

Numerical Simulation of Time-dependent Flow of Williamson Fluid with Heat Transfer

By

Aamir Hamid

A Thesis

*Submitted in the Partial Fulfillment of the
Requirements for the Degree of*

DOCTOR OF PHILOSOPHY

IN

MATHEMATICS

Supervised by

Prof. Dr. Masood Khan

Department of Mathematics
Quaid-i-Azam University, Islamabad
PAKISTAN

2019

Author's Declaration

I, **Aamir Hamid**, hereby state that my PhD thesis titled **Numerical Simulation of Time-dependent Flow of Williamson Fluid with Heat Transfer** is my own work and has not been submitted previously by me for taking any degree from the Quaid-I-Azam University Islamabad, Pakistan or anywhere else in the country/world.

At any time if my statement is found to be incorrect even after my graduate the university has the right to withdraw my PhD degree.



Name of Student: **Aamir Hamid**

Date: **November 22, 2019.**

Plagiarism Undertaking

I solemnly declare that research work presented in the thesis titled "**Numerical Simulation of Time-dependent Flow of Williamson Fluid with Heat Transfer**" is solely my research work with no significant contribution from any other person. Small contribution/help wherever taken has been duly acknowledged and that complete thesis has been written by me.

I understand the zero tolerance policy of the HEC and **Quaid-i-Azam University** towards plagiarism. Therefore, I as an Author of the above titled thesis declare that no portion of my thesis has been plagiarized and any material used as reference is properly referred/cited.

I undertake that if I am found guilty of any formal plagiarism in the above titled thesis even afterward of PhD degree, the University reserves the rights to withdraw/revoke my PhD degree and that HEC and the University has the right to publish my name on the HEC/University Website on which names of students are placed who submitted plagiarized thesis.

Student/Author Signature:



Name: **Aamir Hamid**

Numerical Simulation of Time-dependent Flow of Williamson Fluid with Heat Transfer


By

Aamir Hamid


CERTIFICATE

A THESIS SUBMITTED IN THE PARTIAL FULFILLMENT OF THE
REQUIREMENTS FOR THE DEGREE OF THE
DOCTOR OF PHILOSOPHY IN MATHEMATICS


We accept this thesis as conforming to the required standard



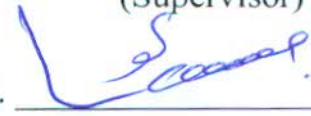
Prof. Dr. Sohail Nadeem
(Chairman)

2. 

Prof. Dr. Masood Khan
(Supervisor)

3.  22/11/2019

Prof. Dr. Saleem Asghar
(External Examiner)

4.  22/11/2019

Dr. Abdullah Shah
(External Examiner)

Department of Mathematics, COMSATS
University, Park Road Chak Shahzad,
Islamabad.

Department of Mathematics, COMSATS
University, Park Road Chak Shahzad,
Islamabad.

Department of Mathematics
Quaid-I-Azam University
Islamabad, Pakistan
2019

Certificate of Approval

This is to certify that the research work presented in this thesis entitled Numerical Simulation of Time-dependent Flow of Williamson Fluid with Heat Transfer was conducted by Mr. Aamir Hamid under the kind supervision of Prof. Dr. Masood Khan. No part of this thesis has been submitted anywhere else for any other degree. This thesis is submitted to the Department of Mathematics, Quaid-i-Azam University, Islamabad in partial fulfillment of the requirements for the degree of Doctor of Philosophy in field of Mathematics from Department of Mathematics, Quaid-i-Azam University Islamabad, Pakistan.

Student Name: Aamir Hamid

Signature: 

External committee:

a) External Examiner 1:

Name: **Prof. Dr. Saleem Asghar**

Designation: Professor

Office Address: Department of Mathematics, COMSATS University, Park Road Chak Shahzad, Islamabad.

Signature:  22/11/2019

b) External Examiner 2:

Name: **Dr. Abdullah Shah**

Designation: Associate Professor

Office Address: Department of Mathematics, COMSATS University, Park Road Chak Shahzad, Islamabad.

Signature:  22/11/2019

c) Internal Examiner

Name: **Prof. Dr. Masood Khan**

Designation: Professor

Office Address: Department of Mathematics, QAU Islamabad.

Signature: 

Supervisor Name:

Prof. Dr. Masood Khan

Name of Dean/ HOD

Prof. Dr. Sohail Nadeem

Signature: 

Signature: 

Dedication

*To my sweet Mother
whose wisdom and patience will never be forgotten.*

*To my dear father
for their tender love and support have put me where I am now.*

§

*To my sisters and my brother
for immense support and encouragements.*

Acknowledgments

*First and foremost, praises and thanks to **Allah**, the Almighty, for His showers of blessings throughout my research work to complete my PhD thesis successfully.*

*I cannot forget the ideal man of the world and most respectable personality for whom Allah created the whole universe, **Prophet Mohammed** (Peace Be Upon Him). I offer my humblest gratitude to Him and seek His assistance and forgiveness.*

*My profound gratitude goes to my supervisor **Prof. Dr. Masood Khan**, who cordially welcomed me into his research group. He has been a real mentor to me that provided his advices unconditionally for everything academic and non-academic throughout these years. He has inspired me to become an independent researcher and helped me realize the power of critical reasoning. He also demonstrated what a brilliant and hard-working scientist can accomplish. His continuous support, motivation and untiring guidance have made this dream come true. I have been extremely lucky to have a supervisor who cared so much about my work, and who responded to my questions and queries so promptly.*

*I would like to express my very great appreciation to my teachers **Prof. Dr. Tasawar Hayat** and **Prof. Dr. Sohail Nadeem** and other members of the department for their valuable and constructive suggestions. I am grateful to everyone at the department of Mathematics, Quaid-i-Azam University.*

*For this dissertation I would like to thank my oral defense committee, **Prof. Dr. Saleem Asghar** and **Dr. Abdullah Shah**, for letting my defense be an enjoyable moment, and for your brilliant comments and suggestions, thanks to you.*

I am extremely grateful to my dearest friends and seniors, Muhammad Irfan, Hashim, Aman Ullah, Masood ur Rahman, Latif Ahmad, Kaleem Iqbal, Jawad Ahmed, Muhammad Waqas, Muhammad Ijaz Khan, Sharafat Hussain, Zahoor Iqbal, Abdul Hafeez, Awais Ahmed, Muhammad Naveed Khan and many others for their friendship, loved, encouraged, entertained, tremendous help and useful discussions in the most positive way.

Finally, but by no means least, I preserve my respects and love to my parents, for their continuous support and encouragement over the years for their love, moral support and encouragement. I would like to thank my loving family with their unconditional, pure and wonderful love that made me climb mountains throughout my academic career and in my personal life. I could never have done it without you, you are the best I could ever have wished for. Lastly, I would especially like to say a heartfelt thank you to my sisters and my brother for keeping me grounded and their selfless love and support for me to pursue the PhD degree.

It has been a wonderful trip these last four years and I would not mind repeating it. I learned a lot, laughed a lot, met a lot of people and harvested from the best times, learned and roughened up from the bad times and will always be thankful to the ones (both named and those unnamed) that help me reach the end.

Aamir Hamid

November 2019

Abstract

The investigation carried out in this thesis focuses on the numerical analysis of time-dependent flow and heat transfer of a non-Newtonian Williamson fluid. In the literature, several constitutive equations were calculated which describe the relation between stress and rate of strain for non-Newtonian fluids. We have chosen the constitutive equation as suggested by Williamson for pseudoplastic materials and proposed the model equations to describe the boundary layer Williamson fluid flow. The core focus of this thesis is to study the behavior of different geometries, like, planar stretching sheet, radially stretching sheet, stretching/shrinking sheet, stretching cylinder, expanding/contracting cylinder and static/moving wedge, for flow patterns of non-Newtonian Williamson fluid.

We know that when fluid flows over a solid body, such as the hull of a ship or an aircraft, frictional forces retard the motion of the fluid in a thin layer close to the solid body. The development of this thin layer is a major contributor to the flow resistance and is of great importance in many engineering and industrial problems. Therefore, the study of such boundary layer flows of non-Newtonian fluids due to different stretching geometries have gained remarkable aspects in numerous industrial applications. Keeping this in view, the present thesis finds out how the stresses on the bodies are affected and to know the behavior of the Weissenberg number of these stresses in relation to the contribution of zero and infinity shear rate viscosity. Additionally, the non-Newtonian Williamson fluid flow due to different stretching surfaces finds its extensive applications in the area of agriculture, engineering, petroleum industries, geothermal reservoir and geothermal energy extractions.

This thesis further presented the characteristics of heat and mass transport of non-Newtonian Williamson fluid. A computational code is developed for the present analysis and it is verified against the available numerical data. Numerical outcomes characterizing the performances of velocity, temperature and concentration distributions are captured through graphical illustrations. The surface drag force, heat and mass transfer rates are also obtained. It is found that the Weissenberg number slow down the fluid motion while

it enhances the temperature distribution. Further, it is worth mentioning that an increment in the unsteadiness parameter diminishes the fluid velocity and temperature, respectively. It is interesting to note that the higher the viscosity ratio parameter has a tendency to decrease the skin friction coefficient substantially.

Contents

1	Introduction	5
1.1	Motivation and Literature Survey	5
1.2	Basics Conservation Laws	15
1.2.1	Mass Conservation	15
1.2.2	Linear Momentum Conservation	16
1.2.3	Energy Conservation	17
1.2.4	Concentration Conservation	17
1.2.5	Energy Conservation for Nanofluids	18
1.2.6	Mass Conservation for Nanofluids	19
1.3	Research Methodology	19
1.3.1	Runge-Kutta Fehlberg Method (RKF-45)	19
1.4	Scope of Research	20
1.5	Thesis Overview	21
2	Impact of Non-linear Thermal Radiation on Unsteady Williamson Fluid Flow	25

2.1	Governing Equations	26
2.2	Geometry of the Problem	28
2.3	Mathematical Formulation	28
2.3.1	Parameters of Physical Interest	31
2.4	Numerical Implementation	32
2.4.1	Validation of Numerical Scheme	34
2.5	Physical Description	34
3	Unsteady Heat Transfer in Williamson Fluid Flow past a Wedge	44
3.1	Physical Problem Description	44
3.1.1	Quantities of Physical Interest	48
3.2	Numerical Procedure	49
3.2.1	Testing of the Code	50
3.3	Results and Discussion	50
4	Transient Flow of Magneto-Williamson Nanofluid due to Wedge	57
4.1	Mathematical Analysis	58
4.1.1	Engineering coefficients	61
4.2	Numerical Simulations	62
4.2.1	Code Validation	63
4.3	Numerical Result and Discussion	64
5	Axisymmetric Flow of Williamson Nanofluid with Slip Mechanism	79
5.1	Flow Equations	80

5.2	Flow Analysis	83
5.2.1	Physical Quantities	87
5.3	Numerical Scheme	88
5.3.1	Validation of Numerical Results	90
5.4	Physical Description	90
6	Unsteady Mixed Convective Flow of Williamson Nanofluid with Variable Thermal Conductivity	102
6.1	Problem Formulation	103
6.1.1	Engineering and Industrial Parameters of Interest	106
6.1.2	Numerical Method for Solution	107
6.1.3	Numerical Validation of the Algorithm	108
6.2	Numerical Results	108
7	Chemically Reacting Flow of Williamson Nanofluid by a Stretching Cylinder	118
7.1	Problem Modelling	119
7.1.1	Parameters of Physical Significance	123
7.1.2	Computational Procedure	123
7.2	Results and Discussion	124
7.2.1	Velocity and Temperature Profiles	124
7.2.2	Nanoparticles Concentration Profiles	126
7.2.3	Skin friction and Nusselt number	127
8	Williamson Fluid Flow driven by Shrinking Surface	135

8.1	Problem Description	136
8.1.1	Engineering Coefficients	139
8.2	Numerical Methodology	139
8.2.1	Validation of Numerical Data	140
8.3	Computational Results	141
9	Thermal Radiation Impact on Williamson Nanofluid Flow induced by an Expanding/Contracting Cylinder	152
9.1	Problem Statement	153
9.1.1	Boundary Conditions	155
9.1.2	Dimensionless forms of Equations	156
9.1.3	Engineering Parameters	157
9.2	Numerical Procedure	158
9.2.1	Validation of Numerical Results	159
9.3	Discussion of Numerical Approach	159
9.3.1	Momentum Boundary Layer	160
9.3.2	Thermal Boundary Layer	161
9.3.3	Concentration Boundary Layer	162
10	Conclusions and Forthcoming Work	175
10.1	Summary of Results	175
10.2	Suggestions for Future Work	177

Chapter 1

Introduction

This chapter consists of preliminary research, literature survey and motivation that encourages us to pursue this research project. Additionally, the outline of the thesis are briefly described at the end.

1.1 Motivation and Literature Survey

Newtonian fluids are defined to have a linear relation between viscous stresses and the local strain rate at each point which arises from their flow. The most common examples of this type includes water and air. Due to their daily life importance, the flows of Newtonian fluids are conventionally regarded as normal. However, there exist several other types of fluids that do not follow the Newton's viscosity law. Broadly, the flow behavior of such type of fluids differ on number of lines. Non-Newtonian fluids appear to be abnormal or even paradoxical initially. However, Walker [1] has described easily reproducible experiments that are able to elaborate the unusual characteristics of non-Newtonian fluids.

The series of explorations dedicated to the study of Newtonian fluids suggest that research of non-Newtonian fluids has not lagged on any scale. An immense amount of study has been performed on non-Newtonian fluids under the cover of different fields. Major topics described in the literature include withdrawal of plates from fluids, pressure dependence of viscosity, agitation and mixing, entrance effects, turbulent flow, instability mould filling, boundary layer theory and fiber spinning, etc. There are many different properties that affect the behavior of the fluid flow which may be utilized to devise categorization of these fluids. The foremost significance in defining the fluid behavior is the viscosity. On this basis, fluids can be subdivided into Newtonian and non-Newtonian. The viscosity is taken to be a constant factor for Newtonian fluids over a certain range of shear rate; however, it can change with temperature and pressure over a range. On the other hand, non-Newtonian fluids have viscosity values that may vary with the shear rate and depends on the shear rate. Several constitutive relations and viscosity models are available varying in their extent of complexity. Bird *et al.* [2] and Barnes *et al.* [3] provide a great overview of many widely encountered viscosity models.

Recently, numerous theoretical and experimental researches have been presented to elaborate the non-Newtonian transport phenomena because of their substantial applications in several industrial and biological activities, mechanical and materials engineering, etc. No doubt, research regarding the non-Newtonian fluid has acquired abundant importance in comparison to Newtonian fluids owing to their extensive engineering applications. For instance, bio-fluids in biological tissue and polymers, emulsions, nuclear fuel slurries, biomedical and lubricants flows, polymeric fluids extrusion, etc. The complex features of these non-Newtonian fluids, like, thixotropy, shear-thinning or shear-thickening and viscoelasticity, show some remarkable application prospects or possibilities, even though bound together perspectives [4] and [5] have

not yet risen for the present. In such manner, various rheological models portraying the non-Newtonian conduct have been proposed. However, majority of non-Newtonian models include some type of modification to their momentum conservation equations. Based on distinct rheological features of the non-Newtonian fluids, several constitutive models have been presented to manifest such fluids. Some existing models of non-Newtonian fluids include power-law model, Oldroyd-B models, differential Reiner-Rivlin models, Carreau model, Sisko model, Ellis model and Williamson model, etc. Out of these Williamson [6] is a simple, yet elegant constitutive model which was originally proposed to simulate the pseudoplastic shear-thinning characteristics of non-Newtonian fluids. The shear-thinning materials are those in which apparent viscosity decreases instantaneously with uplifting shear rate. This three-parameter model is the generalization of Newtonian fluids which has the propensity to elaborate the behavior of polymer melts, blood and paints, etc. The mathematical expression of Williamson constitutive model is expressed as $\mu = \mu_\infty + (\mu_0 - \mu_\infty) (1 - \Gamma\dot{\gamma})^{-1}$, in which μ_0 represents the zero shear rate viscosity and μ_∞ shows infinitely large shear rate viscosity and Γ a material constant. The shear rate is defined as $\dot{\gamma} = \sqrt{\frac{1}{2} \sum_i \sum_j \dot{\gamma}_{ij} \dot{\gamma}_{ji}}$. Due to the prominence applications in biological phenomena, the peristaltic flow and heat transfer analysis of Williamson fluid have fascinated the attention of many researchers, for instance, Nadeem and Akram [7], Vasudev *et al.* [8], Akbar *et al.* [9] and Eldabe *et al.* [10], etc. The convective heat transfer analysis for the flow of Williamson nanofluid by linear stretching/shrinking sheet was reported by Gorla and Gireesha [11]. In this work, they employed the Runge-Kutta integration scheme to find the dual solutions for flow field. Kumar *et al.* [12] numerically investigated the two-phase flow of Williamson fluid with heat transfer by incorporating thermal radiation and temperature jump. Recently, Ramzan *et al.* [13] developed the numerical solution of Williamson fluid flow with

non-Fourier heat transfer considering homogeneous-heterogeneous reactions.

Nanotechnology is a fast emerging field of science that started after Richard P. Feynman's lecture, "There's Plenty of Room at the Bottom". It uses particles with different spatial structure and composition. However, a size of less than 100 nanometers remains constant. Devising methods of formation and characterization of nanosize object having a well-defined geometry and are subject of great research for scientific institutions around the world. Today we note a very intense transfer of nanotechnology from laboratories to daily life. Nanoparticles are increasingly found as components of paints, drugs, cosmetics, food packaging, tires and fabrics. Often, they are components of complex fluids such as polymer solutions, molecular solutions or ordered phases of liquid crystals. Understanding the properties of nanoscale systems is interesting for cognitive reasons. It would encourage the design of materials with definite properties and structure. Hence, it is advisable to inspect systems consisting of nanoparticles and complex fluids such as lyotropic ordered phases of liquid crystals and molecular solutions.

Nanotechnology has appealed to a number of researchers since its advent who investigated the use of nanofluids in the realm of both theoretical and experimental areas. The ability of the nanofluids to transfer the heat more efficiently has made them attractive for a number of industries including nuclear reactors, chemical industry, biological and gas sensing and solar synthesis. These industries have adopted the nanoparticles to intensify the heat-transport capability of the normal fluids. This promise of the nanofluids was proved theoretically for the first time by Choi *et al.* [14] who established that thermal conductivity of the normal fluids becomes doubled upon the addition of nanoparticles. The results reported by Masuda *et al.* [15] and Eastman *et al.* [16] have illustrated that addition of less than 5% of nanoparticles can improve 10–15% of thermal conductivity of the basic fluids making a substantial improvement.

Buongiorno [17] rectified the weaknesses of dispersion and homogeneous models and presented a non-homogeneous, two component model comprising of four equations to illustrate the unusual improvement in the convective heat transfer using nanofluids. Tiwari and Das [18] examined the features of heat transport on nanofluids flow in a two-sided lid-driven heated square cavity. Experimental work [19] has demonstrated that the nanofluid requires 5% volumetric portion for a compelling heat transfer upgrades. Kuznetsov and Nield [20] used the Buongiorno's model to show the impact of thermophoresis diffusion and Brownian motion on the natural convection flow subjected to nanoparticles driven by a vertical surface. Khan and Pop [21] discussed the mechanism of heat and mass transfer in free convection flows of nanofluid past a porous medium. Transient hydro- magnetic rotating flow of a nanofluid with free convection was analyzed by Hamad and Pop [22]. Sheikholeslami and Ganji [23] investigated the rotating 3D flow of an electrically conducting nanofluid. After that, number of researches have been reported on improvement of heat transfer rate in flow of nanofluids over various geometries, like, Dhanai *et al.* [24], Hashim and Khan [25], Hayat *et al.* [26], Nayak *et al.* [27] and Dogonchi and Ganji [28].

The review of magnetohydrodynamic (MHD) features has many important applications in modern engineering and industry, namely solar physics, plasma confinement, cosmology, and many more. Physically, when an external magnetic field is applied to an electrically conducting fluid, it has an ability to create the induced electric and magnetic fields. By assuming of lower magnetic Reynolds number, we can ignore the contribution of the induced magnetic field which interacts with electrically conducting fluid to produce Lorentz force [29]. The applied magnetic field is generally utilized to control momentum and heat transportation in the boundary region. It appears that, Pavlov [30] initially formulated the incompressible magneto-

viscous fluid considering plane sheet deformation. Afterwards, Chakrabarti and Gupta [31] extended this work by including the analysis of the temperature distribution. Hayat *et al.* [32] reported the aspect of heat transport in stretched surface with magnetic effect. Turkyilmazoglu [33] realized that the presence of magnetic field in the boundary layer flow of different fluids is used to control the momentum and heat transfer rate. Dessie and Kishan [34] scrutinized the impact of magnetic field in dissipative stretching flow subjected to variable viscosity and heat sink/source aspects. Waqas *et al.* [35] addressed the MHD flow of micropolar fluid generated by nonlinear convective heated stretching surface considering the effects of mixed convection. Reddy *et al.* [36] elaborated the MHD stretched flow of nanofluid through the porous medium with radiation effect. It is fascinating to take note of those similar studies in different liquids were performed by Hsiao [37, 38], where he described that the electrically conducting magnetic field enhancing the temperature field at a particular domain of the flow. Recently, Haq *et al.* [39] discussed the mixed convective flow along a porous vertical stretching sheet under the effects of magneto-hydrodynamics. They reported the numerical as well as analytical solution of the mentioned problem. Enormous research works [40 – 42] have been done on MHD flows due to stretched surface under different physical situations.

According to researchers, radiative heat transport phenomenon is one of the thrust field of science and engineering. Most engineering processes occurs because of high temperature and hence the study of radiative heat transport plays a remarkable aspects in the structure and design of advanced energy systems. Mukhopadhy *et al.* [43] inspected the effect of nonlinear radiation on steady flow and heat transport behavior across a permeable surface. After that, Cortell [44] presented a numerical investigation to study the radiative heat transfer features by utilizing the Rosseland approximation for electrically conducting viscous fluid flow. He

concluded that the fluid temperature was significantly boosted by the rising thermal radiation. Besides, Hayat *et al.* [45] explored the three-dimensional flow of viscous nanofluid by considering the effects of radiative heat transfer and momentum slip condition. Analytical solutions for momentum and thermal fields have been computed by employing homotopy analysis methods. The oblique stagnation point flow of an electrically conducting viscous nanofluid with convective heat transfer mode and thermal radiation have been probed by Khan *et al.* [46]. Lately, extensive researches have been done in radiative flow and heat transfer subjects [47], [48], [49], [50], [51].

Numerous investigators have given remarkable consideration to incorporate the slip condition at the surface describing the relative movement between the wall and the fluid adjacent to the wall. One can say that this is a basic property that affect the fluid flow features. There is a limited velocity of the liquid-solid interface and such sort of boundary condition for velocity is supposed boundary slip or slip length. Probably, Navier [52] was the first who examined slip condition and observed the tangential slip velocity u_w is linearly related to shear stress τ_w , in the form $u_w = L\tau_w$, where L represents slip factor that changes with the presence of temperature, pressure, normal stress, molecular parameter, and the characteristics of the liquid-solid connection. The boundary layer flow due to a stretched surface with slip condition was initiated by Wang [53]. Later on, Zheng *et al.* [54] reported the radiative flow of nanofluids with combined slip impacts within the sight of permeable medium. Mukhopadhyay [55] scrutinized the flow of an incompressible viscous fluid by considering partial slip mechanism. Later, Khan and Hashim [56] investigated the impact of velocity, thermal and concentration slips driven by a moving wedge for Carreau fluid model. Xie *et al.* [57] explored the numerical solutions for flow and heat transfer analysis of low pressure gas in slip flow regime. They revealed that

the temperature jump decays the heat flux, while the velocity slip improves the rate of heat transfer.

Due to the complexity faced on consideration of all the chemical reactions of a system, it becomes more convenient and simple to limit to binary type only. A chemical reaction needs activation energy which is an amount must be available to start off. The activation energy for a reaction can be determined using Arrhenius equation that describes how the rate constant changes with temperature. Chemical reactions are described by a substance change and at least one product is yielded that have properties not quite the same as the reactants. As a fundamental step in the process of manufacturing, many industrial applications need some form of chemical reaction. These types of reactions are conventionally carried out in chemical reactors and often limited by the degree of mass transfer achieved. It is essential to make the reaction efficient, minimizing the number of reagents, energy inputs and waste while maximizing the yield. Bestman [58] has studied the impact of chemical reaction for binary reaction model with Arrhenius activation energy. Latterly, Kandasamy *et al.* [59] illustrated the effects of chemically reacting flow driven by a wedge-shaped geometry with generation/absorption. They found that chemical reaction parameter reduces the velocity distribution. The impact of chemical reaction and radiative heat transfer induced by a permeable flat plate was studied by Makinde *et al.* [60]. They revealed that the fluid velocity declines with higher values of buoyancy forces and wall suction parameter. Maleque [61] elaborated the binary chemical reaction on boundary layer flow with viscous dissipation. Later on, Wahiduzzaman *et al.* [62] considered nanofluid flow with the impact of heat generation, chemical reaction and thermal radiation past a shrinking sheet. After that, Mabood *et al.* [63] numerically studied nanofluid flow with chemical reaction and viscous dissipation. In their analysis, they exhibited that nanoparticles concentration declined

with an increment in chemical reaction parameter. Makinde and Animasaun [64] analyzed the behavior of thermophoresis diffusion and Brownian motion on bio-convection of nanofluid with chemical reaction effect. In another paper, Eid [65] illustrated the impact of chemical reaction on mixed convective nanofluid flow due to stretched surface. A theoretical review on nanofluid flow induced by rotating disk with chemical reaction was reported by Reddy *et al.* [66]. Chemical reaction and activation energy aspects in nanofluid generated by a vertical plate in the presence buoyancy effects are considered by Mustafa *et al.* [67]. Hsiao [68] applied the controlling method to promote the radiative activation energy of a manufacturing system of Carreau-nanofluid. He utilized the finite difference technique to obtain the convergence and stability of the problem. Khan *et al.* [69] investigated the effect of chemical reaction on stretched flow of Casson fluid.

It is notable that Chaim [70] was the first to contemplate the stagnation-point flow past an elastic sheet by taking the similar value of stretching as well as free stream velocity. Since then, many authors have extended this idea to consider the different aspects of the stagnation point flows. Stagnation point flow is still attracting many researchers attention because of its imperative practical applications. Examples of such technological processes are cooling of electronic devices, the cooling of nuclear reactors during emergency shutdown, hydrodynamic processes in engineering applications and MHD generators. Aman *et al.* [71] acquired the numerical results of two-dimensional stagnation point flow induced by a linearly stretching/shrinking surface. The stagnation point flow of nanofluids generated by a stretching surface is reported by Nandy and Mahapatra [72]. Saleh *et al.* [73] discussed the viscous flow past a vertical shrinking surface with mixed convection in stagnation region. Dash *et al.* [74] investigated the electrically conducting flow towards stretching/shrinking surface by incorporating heat source/sink effect

near a stagnation point. Recently, Nasir *et al.* [75] have studied the stagnation point flow generated by a permeable quadratically stretching/shrinking surface and found the dual nature of solutions for certain parameters. Additionally, Seth *et al.* [76] analyzed the properties of magnetic field in stagnation region considering heat generation/absorption.

The study of heat transfer mechanism through stretching surfaces have received a great deal of research interest due to its engineering and industrial applications, for instance, manufacturing of fiber-glass, enhancement in efficiency of paints and lubrication, plastic-molding, extrusion of polymers, etc. Crane [77] was the pioneer who studied the flow over a linear stretching plate and obtained the analytical solution for the Navier-Stoke's equations. Later on, Grubka and Bobba [78] predicted that the solution calculated by Crane is the exact solution of the Navier-Stoke's equations. The work done by Crane [77] was prolonged by Grubka and Bobba [78] by including the mass transfer effects on the stretched surface. The impact of viscous dissipation on radiative flow over a stretching plate was studied by Cortell [79]. Further, Khan *et al.* [80] studied the heat transport mechanism for Carreau fluid flow with convective heated surface. Their study revealed that fluid velocity decrease significantly by the magnetic field. Moreover, Rahimi *et al.* [81] employed the Collocation method to discuss the behavior of an Eyring-Powell fluid past a linearly stretching surface. Mahabaleshwar *et al.* [82] elaborated the thermal radiation effects on Walter-B liquid flow in stretched surface with Navier-slip conditions.

Over the past few years, the flow and heat transfer analysis past wedge-shaped bodies has been a matter of utmost synchronic interest in the field of engineering and chemical industry. Usually, such sort of flows occur in aerodynamics, ground water pollution, geothermal industries, etc. This concept was initially proposed by Falkner and Skan [83] in 1931. In their model, they

depicted that pressure gradient played a vital role in such types of flow and flow was caused by the pressure gradient. After that, Rajagopal *et al.* [84] extended the work of Falkner and Skan for the flow of second grade fluid and accomplished the solutions by perturbation technique. Several studied describing the impacts of distinct physical phenomena on Falkner-Skan flow are demonstrated in literature, such as, Chamkha *et al.* [85], Hossain *et al.* [86], Ishaq *et al.* [87], Hsiao [88] and Hayat *et al.* [89].

During the past few decades, flow over a circular cylinder have gained notable attention due to rapidly growing applications in many industrial and engineering processes. In 1975, Crane [90] investigated the boundary layer flow generated by a stretched cylinder. Later on, Wang [91] initially reported the flow of Newtonian fluid outside the stretching cylinder. Some recent studies concerning the fluid flow past a circular cylinder was studied by the researchers such as Ishak and Nazar [92], Lok and Pop [93], Fang *et al.* [94], Zaimi *et al.* [95].

1.2 Basics Conservation Laws

The conservation laws of physics like the law of concentration, energy, mass and momentum govern the mechanics of fluids. Mathematical formulation for the conservation hypothesis are stated in differential form as:

1.2.1 Mass Conservation

The mass conservation law describes that the time rate of increase of mass within a control volume $v(t)$ must be equal to to net rate of mass in $v(t)$. This relation can be denoted as:

$$\int_{v(t)} \left(\frac{\partial \rho}{\partial t} + \nabla \cdot (\rho \mathbf{V}) \right) dv = 0. \quad (1.1)$$

As this is true all $v(t)$, so the integrand vanishes at every point. Thus, the mass conservation law is given by

$$\frac{\partial \rho}{\partial t} + \nabla \cdot (\rho \mathbf{V}) = 0. \quad (1.2)$$

Also, the above law is famous as the continuity equation, where ρ denotes the fluid density, \mathbf{V} the velocity field and t be the time.

The continuity equation reduces to the incompressible form as:

$$\nabla \cdot \mathbf{V} = 0. \quad (1.3)$$

1.2.2 Linear Momentum Conservation

According to Newton's second law of motion, which states that the time rate of momentum of a control volume equals the resultant force acting on it. It can be expressed in mathematical form as;

$$\int_{v(t)} \left[\frac{\partial \rho \mathbf{V}_\alpha}{\partial t} + (\rho \mathbf{V}_\alpha \mathbf{V}_\beta)_{,\beta} \right] dv = \int_{v(t)} [\rho \mathbf{B} + \boldsymbol{\tau}_{\alpha\beta,\beta}] dv, \quad (1.4)$$

which implies that

$$\frac{\partial \rho \mathbf{V}_\alpha}{\partial t} + (\rho \mathbf{V}_\alpha \mathbf{V}_\beta)_{,\beta} = \rho \mathbf{B} + \boldsymbol{\tau}_{\alpha\beta,\beta}, \quad (1.5)$$

which is the momentum conservation law. In Eq. (1.5), $\boldsymbol{\tau}_{\alpha\beta}$ is the stress tensor and \mathbf{B} the body force per unit volume.

In a more convenient way the conservation of linear momentum takes the form

$$\rho \left[\frac{\partial \mathbf{V}}{\partial t} + \mathbf{V} \cdot \nabla \mathbf{V} \right] = \text{div } \boldsymbol{\tau} + \rho \mathbf{B}. \quad (1.6)$$

1.2.3 Energy Conservation

The conservation of energy is derived from the first law of thermodynamics. It is mathematically defined as

$$\rho c_p \frac{dT}{dt} = \boldsymbol{\tau} \cdot \mathbf{L} - \text{div } \mathbf{q}_r - \text{div } \mathbf{q}. \quad (1.7)$$

In the above equation, (c_p, T) denote the specific heat and temperature of fluid, respectively.

Further, $(\text{div } \mathbf{q}_r$ and $\text{div } \mathbf{q})$ depict the radiative and thermal heat fluxes, respectively.

The energy flux \mathbf{q} is given as

$$\mathbf{q} = -k \nabla T, \quad (1.8)$$

with k represents the fluid thermal conductivity.

1.2.4 Concentration Conservation

The net concentration of the framework under consideration remains constant. Its expression is obtained by Fick's second law. In the absence of any chemical reaction, it can be written as

$$\frac{\partial \phi}{\partial t} + \mathbf{V} \cdot \nabla \phi = -\nabla \cdot \mathbf{j} + R, \quad (1.9)$$

where, ϕ being the concentration of the fluid, \mathbf{j} the normal mass flux and R "source" or "sink" for ϕ .

The normal mass flux is typically approximated by Fick's first law as

$$\mathbf{j} = -D \nabla \phi, \quad (1.10)$$

where D is the mass diffusivity.

1.2.5 Energy Conservation for Nanofluids

The energy conservation for an incompressible nanofluid is expressed as

$$\rho c_p \frac{dT}{dt} = -h_p \nabla \cdot \mathbf{j}_p - \text{div } \mathbf{q}_p. \quad (1.11)$$

In the above expression, \mathbf{q}_p be the thermal flux of nanofluids, h_p is the enthalpy, \mathbf{j}_p the total nanoparticle mass flux.

Mathematical relations for \mathbf{q}_p and \mathbf{j}_p are as follows:

$$\mathbf{q}_p = -k \nabla T + h_p \mathbf{j}_p, \quad (1.12)$$

$$\mathbf{j}_p = -\rho_p D_B \nabla \phi - \rho_p D_T \frac{\nabla T}{T_\infty}. \quad (1.13)$$

Here, ρ_p denotes the density of nanoparticle, (D_B, D_T) are the Brownian motion and thermophoretic diffusion coefficients.

Now substituting the expressions for \mathbf{q}_p and \mathbf{j}_p into Eq. (1.11), therefore the final equation becomes

$$\rho c_p \frac{dT}{dt} = k \nabla^2 T + \rho_p c_p \left[D_B \nabla \phi \cdot \nabla T + D_T \frac{\nabla T \cdot \nabla T}{T_\infty} \right]. \quad (1.14)$$

1.2.6 Mass Conservation for Nanofluids

Mathematically, nanofluid concentration equation is written as

$$\frac{\partial \phi}{\partial t} + \mathbf{V} \cdot \nabla \phi = -\frac{1}{\rho_p} \nabla \cdot \mathbf{j}_p. \quad (1.15)$$

Making use of Eq. (1.17), we finally have

$$\frac{\partial \phi}{\partial t} + \mathbf{V} \cdot \nabla \phi = D_B \nabla^2 C + D_T \frac{\nabla^2 T}{T_\infty}. \quad (1.16)$$

1.3 Research Methodology

1.3.1 Runge-Kutta Fehlberg Method (RKF-45)

The achievement of numerical solution for ordinary differential equations (ODEs) has been a field of great interest within the fluid dynamic network. For this reason, many authors utilized different numerical schemes to tackle the fluid problems. Generally, numerous techniques are convenient in literature for solving the initial value problems (IVPs) comprising of ODEs. Here, we illustrate Runge-Kutta Fehlberg method which is an ancient and efficient numerical method to compute the solutions of initial value problems. Let an IVP be specified as follows;

$$\frac{dz}{dx} = f(x, z), \quad z(x_m) = z_m. \quad (1.17)$$

The algorithm of RKF-45 is written as

$$z_{m+1} = z_m + h \left(\frac{16}{135} b_0 + \frac{6656}{12825} b_2 + \frac{28561}{56430} b_3 - \frac{9}{50} b_4 + \frac{2}{55} b_5 \right), \quad (1.18)$$

where the coefficients b_0 to b_5 are, respectively, defined as:

$$\left. \begin{aligned} b_0 &= hf(x_m, z_m), \\ b_1 &= hf\left(x_m + \frac{1}{4}h, z_m + \frac{1}{4}b_0\right), \\ b_2 &= hf\left(x_m + \frac{3}{8}h, z_m + \frac{3}{32}b_0 + \frac{9}{32}b_1\right), \\ b_3 &= hf\left(x_m + \frac{12}{13}h, z_m + \frac{1932}{2197}b_0 - \frac{7200}{2197}b_1 + \frac{7296}{2197}b_2\right), \\ b_4 &= hf\left(x_m + h, z_m + \frac{439}{216}b_0 - 8b_1 + \frac{3860}{513}b_2 - \frac{845}{4104}b_3\right), \\ b_5 &= hf\left(x_m + \frac{1}{2}h, z_m - \frac{8}{27}b_0 + 2b_1 - \frac{3544}{2565}b_2 + \frac{1859}{4104}b_3 - \frac{11}{40}b_4\right). \end{aligned} \right\} \quad (1.19)$$

Before using the RK-Fehlberg method, at a very first step, we convert the non-linear differential equations into first order differential structure. The new system of first order ODEs can be obtained by introducing new variables as:

$$f = f_1, \quad f' = f_2, \quad f'' = f_3, \quad \theta = f_4, \quad \theta' = f_5, \quad \phi = f_6, \quad \phi' = f_7. \quad (1.20)$$

1.4 Scope of Research

In human life, the most common and important examples of fluids are air and water that comes across in our daily life. These liquids are basic examples of the Newtonian fluids. However, there exist several other fluids that are less commonly dealt in daily life and found in nature, are classified as non-Newtonian fluids. This relatively small but significant category is an interesting proposition to study the flow mechanism of non-Newtonian fluids. The efforts have been rendered in both physical and mathematical modelling of these fluids. In this thesis, a major part of such research has been dedicated to obtaining an improved view of the bulk flow

of non-linear Williamson fluid over various stretched geometries. The Williamson boundary-layer fluid flow has not been studied on many large scale as compared to other non-Newtonian fluids. This research has used the idea of self-similarity that give some valuable information about the boundary layer behavior. The implementation of the numerical approach for the study of time-dependent Williamson fluid flow in relation to such layer, may also uncover many other aspects of this boundary layer phenomenon.

Our initial interest was the mathematical modelling for the Williamson fluid by incorporating the effects of infinite shear rate viscosity. Consequently, an additional interest in this thesis was the transient flow behavior of Williamson fluid using various mechanisms such as, MHD, mixed convection, thermal radiation, heat source/sink, stagnation-point flow, slip flow, chemical reaction and fluid suction or injected through the surface. There has also been considerable interest and research activity in practical geometries in which fluid flows. We consider time-dependent Williamson fluid flow on a stretching surface, fluid flow past a radially stretching surface, fluid flow past a circular cylinder and fluid flow past a wedge shape geometry. These numerous geometries pose a theoretical challenge to the researchers. In this thesis we develop various flow problems arising from these geometries and employ an efficient numerical technique to solve these problems. Moreover, one other interesting feature of this thesis is the existence of multiple numerical solutions for flow field for certain physical parameters.

1.5 Thesis Overview

The motivation behind this research work is to gain a better understanding about the mechanism of heat transfer for unsteady Williamson fluid flow over certain geometries. In this

dissertation, an extensive numerical approach has been made to explore the heat transfer and fluid flow characteristics for two-dimensional transient flow through different stretched geometries. All the research material produced during this project briefly specified in this section. Thus, the chapter wise arrangement of this thesis is as follows:

Chapter 1: This chapter provides an extensive literature survey behind the present work. A vast number of previous investigations related to linear and non-linear flows over moving surfaces under different aspects are discussed. The basic conservation laws of fluids, numerical methodology, outline of the thesis, motivation and goals of this thesis are also presented.

Chapter 2: This chapter explains the numerical solution of Williamson fluid flow over a planar stretched surface by considering shear rate viscosity at infinity. The prevailing nonlinear PDEs are altered into ODEs and then elucidated numerically by Runge Kutta Fehlberg technique to scrutinize the properties of physical parameters. The contents of this chapter have been published in "*Results Phys.*, 7 (2017) 3968 – 3975".

Chapter 3: This chapter investigated the 2D flow of a non-Newtonian Williamson fluid past a wedge-shaped geometry. The impacts of heat transfer mechanism on time-dependent flow are illustrated graphically. A set of non-dimensional variables are employed to transmute the time-dependent basics flow equations to a first order system of ODEs. The converted conservation equations are numerically incorporated subject to physically appropriate boundary conditions with an efficient numerical method. The outcomes of this chapter are published in "*Results Phys.*, 9 (2018) 479 – 485".

Chapter 4: An investigation regarding the heat transfer characteristics during the time-dependent flow of Williamson fluid due to a static or moving wedge is endowed in this chapter. This chapter also presents the findings from a numerical study of electrically conducting

Williamson nanofluid flow by incorporating convective boundary conditions. The leading PDEs of the flow and heat transfer are altered to a set of ODEs by introducing new non-dimensional quantities. The variations in non-dimensional velocity, temperature and nanoparticle concentration distributions are illustrated to see the influence of physical parameters. The work provided in this chapter is published in "*Int. J. Heat Mass Transf.*, 118 (2018) 480 – 491".

Chapter 5: The foremost concern of this chapter is to deliberate the time-dependent convective axisymmetric Williamson nanofluid flow with a radially stretched wall. The surface nanoparticles concentration is assumed to be uniform and the convective boundary condition is considered. Additionally, radiative heat transfer in the form of Rosseland approximation is considered in here. The control of active parameters on momentum, thermal and concentration fields is deliberated in detail with the help of plotted diagrams and tables. The findings of this chapter are published in "*Eur. Phys. J. Plus*, 134 (2019), doi : 10.1140/epjp/i2019 – 12473 – 9".

Chapter 6: Here, an approximate numerical solution for the mixed convection Williamson fluid flow driven by a radially stretching sheet with nanoparticles and chemically reactive species has been investigated. In addition to this, we consider the nanoparticles condition at the surface. The resultant equations are tackled numerically by a shooting technique. Graphical analysis of several physical parameters on nanofluids velocity, temperature, nanoparticles concentration is demonstrated and discussed with physical reasoning. The work corresponding to this chapter is published in "*J. Mol. Liq.*, 260 (2018) 436 – 446".

Chapter 7: The transient MHD flow Williamson fluid along a stretching cylinder subject to heat generation/absorption and binary chemical reaction is studied theoretically in this chapter. In this investigation, Brownian diffusion and thermophoresis are developed in energy and concentration expressions by employing Buongiorno's model of nanofluid. The ruling math-

emtical system in PDEs is altered over to a system of nonlinear ODEs by non-dimensional analysis. The leading equations of flow model consisting of time dependent momentum, energy and concentration equations are tackled numerically by Runge-Kutta Fehlberg approach. The work presented in this chapter is published in "*J. Mol. Liq.*, 262 (2018) 435 – 442".

Chapter 8: This chapter explores the multiple solutions and combined effects of magnetic field, Ohmic heating and viscous dissipation for time-dependent Williamson fluid flow generated by a permeable shrinking surface. Using suitable transformations, the ODEs equations are integrated by utilizing RKF-45 method. The impact of influential parameters on the dimensionless velocity and temperature distributions is studied and displayed with the help of graphs. The consequences of this chapter are published in "*Int. J. Heat Mass Transf.*, 126 (2018) 933 – 940".

Chapter 9: The cardinal focus of this chapter is to examine the effects of heat generation/absorption, velocity slip and convective heat transfer on the flow of an electrically conducting Williamson nanofluid towards an expanding/contracting cylinder. The study of all governing parameters on the fluid velocity, temperature and nanoparticle volume fraction as well as skin friction coefficient, heat and mass transfer rates are illustrated graphically. The achievements of this chapter have been published in "*Phys. Lett. A*, 126 (2018) 1982 – 1991".

Chapter 10: Finally, the last chapter concludes this thesis and provides a summary of the work presented and suggest some recommendations for future work.

Chapter 2

Impact of Non-linear Thermal Radiation on Unsteady Williamson Fluid Flow

In this chapter, a mathematical model for time-dependent flow of Williamson fluid caused by stretching surface by considering infinite shear rate viscosity has been proposed. The effects of heat source/sink and thermal radiation are considered for the analysis of heat transfer. The similarity transformation technique is utilized to transmute the governing equations of the problem. These nonlinear ODEs are tackled numerically by using Runge-Kutta-Fehlberg 4th–5th order method. The numerical study is performed to investigate the influence of dimensionless parameters subject to their physical characteristics. The results indicate that higher unsteadiness parameter enhances the friction factor at the surface. Additionally, radiative parameter enhances the performance of heat transfer in the flow.

The obtained results are also compared with already published data and a superb agreement is noted.

2.1 Governing Equations

The basic flow equations including the mass conservation, momentum and energy are written as:

$$\nabla \cdot \mathbf{V} = 0, \quad (2.1)$$

$$\rho \frac{d\mathbf{V}}{dt} = \text{div } \boldsymbol{\tau}, \quad (2.2)$$

$$\rho c_p \frac{dT}{dt} = \boldsymbol{\tau} \cdot \mathbf{L} - \text{div } \mathbf{q} - \text{div } \mathbf{q}_r. \quad (2.3)$$

Where, \mathbf{L} denotes the velocity gradient and $\boldsymbol{\tau}$ the Cauchy stress tensor.

The Cauchy stress tensor for Williamson fluid model is expressed as:

$$\boldsymbol{\tau} = -p\mathbf{I} + \mathbf{S}, \quad (2.4)$$

where

$$\mathbf{S} = \left(\mu_\infty + \frac{\mu_0 - \mu_\infty}{1 + \Gamma |\dot{\gamma}|} \right) \mathbf{A}_1, \quad (2.5)$$

where p is the pressure, \mathbf{I} and \mathbf{S} , respectively, denote the identity and extra stress tensors while μ_0 is the zero and μ_∞ the infinity shear rate viscosities, respectively, and Γ the material time constant. While the strain rate $\dot{\gamma}$ is given by

$$\dot{\gamma} = \sqrt{\frac{1}{2} \text{tr}(\mathbf{A}_1^2)}, \quad \text{where } \mathbf{A}_1 = \nabla \mathbf{V} + (\nabla \mathbf{V})^T. \quad (2.6)$$

Here, we consider the case for which $\mu_\infty \neq 0$, $\dot{\gamma} < 0$ and thus Eq. (2.5) takes the form

$$\mathbf{S} = \mu_0 \left(\beta^* + \frac{1 - \beta^*}{1 - \Gamma \dot{\gamma}} \right) \mathbf{A}_1, \quad (2.7)$$

where $\beta^* = \frac{\mu_\infty}{\mu_0}$ represents the ratio of viscosities.

The velocity and temperature fields for two-dimensional unsteady flow have the forms:

$$\mathbf{V} = [u(x, y, t), v(x, y, t), 0], \quad T = (x, y, t), \quad (2.8)$$

where (u, v) signify the components of velocity in (x, y) directions, respectively. From Eq. (2.8), the strain rate $(\dot{\gamma})$ is given by:

$$\dot{\gamma} = \left[4 \left(\frac{\partial u}{\partial x} \right)^2 + \left(\frac{\partial u}{\partial y} + \frac{\partial v}{\partial x} \right)^2 \right]^{1/2}. \quad (2.9)$$

Upon invoking the velocity and temperature fields from Eq. (2.8) along with Eq. (2.9) into Eqs. (2.1) – (2.3), the dimensional form of governing equations under usual boundary-layer assumption take the form:

$$\frac{\partial u}{\partial x} + \frac{\partial v}{\partial y} = 0, \quad (2.10)$$

$$\begin{aligned} \frac{\partial u}{\partial t} + u \frac{\partial u}{\partial x} + v \frac{\partial u}{\partial y} = & -\frac{1}{\rho} \frac{\partial p}{\partial x} + \nu \frac{\partial^2 u}{\partial y^2} \left[\beta^* + (1 - \beta^*) \left(1 - \Gamma \frac{\partial u}{\partial y} \right)^{-1} \right] \\ & + \nu \Gamma \left(\frac{\partial u}{\partial y} \right) \left(\frac{\partial^2 u}{\partial y^2} \right) \left[(1 - \beta^*) \left(1 - \Gamma \frac{\partial u}{\partial y} \right)^{-2} \right], \end{aligned} \quad (2.11)$$

$$0 = -\frac{1}{\rho} \frac{\partial p}{\partial y}, \quad (2.12)$$

$$\frac{\partial T}{\partial t} + u \frac{\partial T}{\partial x} + v \frac{\partial T}{\partial y} = \alpha \frac{\partial^2 T}{\partial y^2} - \frac{1}{\rho c_p} \frac{\partial q_r}{\partial y} + \frac{Q_0}{\rho c_p} (T - T_\infty), \quad (2.13)$$

where $\nu = \mu/\rho$ is the dynamic viscosity.

2.2 Geometry of the Problem

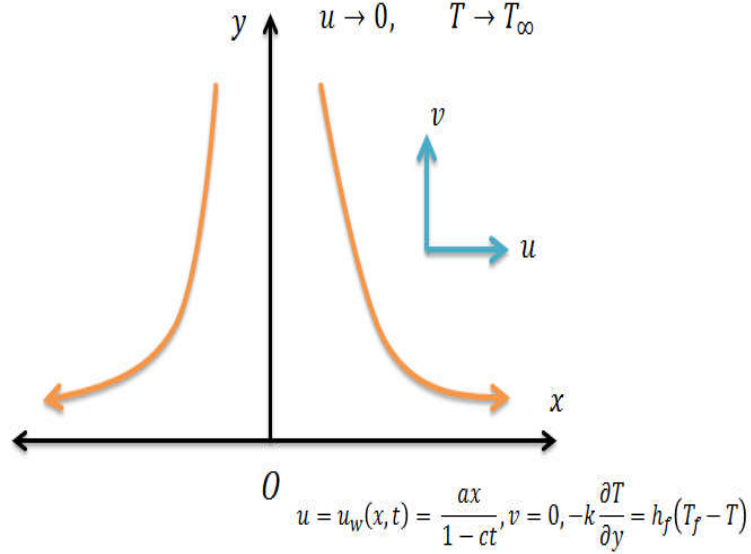


Fig. 2.1: Schematic diagram of physical configuration.

2.3 Mathematical Formulation

We consider a 2D unsteady flow of Williamson fluid driven by a flat stretching surface in the region $y > 0$ (see **Fig. 2.1**). The $U_w(x,t)$ is the stretching velocity with surface temperature $T_w(x,t)$ which is anticipated to be greater than ambient temperature T_∞ ($T_w > T_\infty$). The impact of heat generation/absorption is further incorporated in energy equation.

Under these norms, the equations of radiative Williamson fluid flow are:

$$\frac{\partial u}{\partial x} + \frac{\partial v}{\partial y} = 0, \quad (2.14)$$

$$\begin{aligned} \frac{\partial u}{\partial t} + u \frac{\partial u}{\partial x} + v \frac{\partial u}{\partial y} &= \nu \frac{\partial^2 u}{\partial y^2} \left[\beta^* + (1 - \beta^*) \left(1 - \Gamma \frac{\partial u}{\partial y} \right)^{-1} \right] \\ &+ \nu \Gamma \left(\frac{\partial u}{\partial y} \right) \left(\frac{\partial^2 u}{\partial y^2} \right) \left[(1 - \beta^*) \left(1 - \Gamma \frac{\partial u}{\partial y} \right)^{-2} \right], \end{aligned} \quad (2.15)$$

$$\frac{\partial T}{\partial t} + u \frac{\partial T}{\partial x} + v \frac{\partial T}{\partial y} = \alpha \frac{\partial^2 T}{\partial y^2} - \frac{1}{\rho c_p} \frac{\partial q_r}{\partial y} + \frac{Q_0}{\rho c_p} (T - T_\infty), \quad (2.16)$$

along with the boundary conditions

$$u = U_w(x, t), \quad v = 0, \quad -k \frac{\partial T}{\partial y} = h_f (T_f - T) \quad \text{at } y = 0, \quad (2.17)$$

$$u \rightarrow 0, \quad T \rightarrow T_\infty \quad \text{as } y \rightarrow \infty. \quad (2.18)$$

The q_r via Rosseland approximation is simplified as:

$$q_r = -\frac{4\sigma^{**}}{3k^*} \frac{\partial T^4}{\partial y} = -\frac{16\sigma^* T^3}{3k^*} \frac{\partial T}{\partial y}, \quad (2.19)$$

in which k^* indicates the mean absorption coefficient and σ^{**} denotes the Stefan-Boltzmann constant. Utilizing Eq. (2.19) into Eq. (2.16), we have the following form of energy equation:

$$u \frac{\partial T}{\partial x} + v \frac{\partial T}{\partial y} + w \frac{\partial T}{\partial z} = \alpha \frac{\partial^2 T}{\partial y^2} + \frac{16\sigma^{**}}{3k^* \rho c_p} \frac{\partial}{\partial y} \left(T^3 \frac{\partial T}{\partial y} \right) + \frac{Q_0}{\rho c_p} (T - T_\infty), \quad (2.20)$$

where $\alpha \left(= \frac{k}{(\rho c)_p} \right)$ signify the thermal diffusivity.

In addition, $U_w(x, t)$ and $T_w(x, t)$ are of the form:

$$U_w(x, t) = \frac{ax}{1 - ct}, \quad T_w(x, t) = T_\infty + \frac{T_0 U_w x}{\nu(1 - ct)^{\frac{1}{2}}}. \quad (2.21)$$

In the above expression, $ct < 1$ while a and c are dimensional constants having dimension T^{-1} . The effective rate of stretching $\frac{1}{(1-ct)}$ increments or decays with time as $c > 0$ or $c < 0$, respectively.

Let us define the non-dimensional transformations [98] :

$$\eta = y \sqrt{\frac{U_w}{\nu x}}, \quad \psi(x, y, t) = \sqrt{\nu U_w x} f(\eta), \quad \theta(\eta) = \frac{T - T_\infty}{T_w - T_\infty}, \quad (2.22)$$

where ψ is the stream-function with $u = \frac{\partial \psi}{\partial y}$ and $v = -\frac{\partial \psi}{\partial x}$.

Substituting Eqs.(2.21 – 2.22) into (2.15 – 2.20), we obtain

$$\left[\beta^* + (1 - \beta^*) (1 - We f'')^{-2} \right] f''' + f f'' - (f')^2 - A \left[f' + \frac{\eta}{2} f'' \right] = 0, \quad (2.23)$$

$$[\{1 + R_d(1 + (\theta_w - 1)\theta)^3\}\theta']' + Pr(f\theta' - 2f'\theta) - Pr \frac{A}{2}(\eta\theta' + 3\theta) + Pr \delta\theta = 0, \quad (2.24)$$

subject to the boundary conditions

$$f(0) = 0, \quad f'(0) = 1, \quad \theta'(0) = -\gamma(1 - \theta(0)), \quad (2.25)$$

$$f'(\infty) \rightarrow 0, \quad \theta(\infty) \rightarrow 0. \quad (2.26)$$

The dimensionless parameters are given by:

$$\begin{aligned} We & \left(= \sqrt{\frac{a^3 \Gamma^2 x^2}{\nu(1-ct)^3}} \right), \quad Pr \left(= \frac{\mu c_p}{k} \right), \quad \delta \left(= \frac{Q_0(1-ct)}{\alpha(\rho c)_f} \right), \quad A \left(= \frac{c}{a} \right), \\ Rd & \left(= \frac{16\sigma^{**}T_\infty^3}{3k^*k} \right), \quad \theta_w \left(= \frac{T_f}{T_\infty} > 1 \right), \quad \gamma \left(= \frac{h_f}{k} \sqrt{\frac{\nu}{\alpha}} \right). \end{aligned} \quad (2.27)$$

Here, We , Pr , A , δ , Rd , θ_w and γ denote the local Weissenberg number, Prandtl number, unsteadiness parameter, heat source parameter ($\delta > 0$) and heat sink parameter ($\delta < 0$), radiation parameter, temperature ratio parameter and the Biot number, respectively.

2.3.1 Parameters of Physical Interest

The skin friction coefficient (C_{fx}) and the Nusselt number (Nu_x) are reported as follows:

$$C_{fx} = \frac{\tau_w}{\rho U_w^2}, \quad Nu_x = \frac{xq_w}{k(T_f - T_\infty)} + \frac{xq_r}{k(T_f - T_\infty)}. \quad (2.28)$$

In which τ_w and q_w are expressed as:

$$\tau_w = \mu_0 \frac{\partial u}{\partial y} \left[\beta^* + (1 - \beta^*) \left(1 - \Gamma \frac{\partial u}{\partial y} \right)^{-1} \right], \quad q_w = -k \left(\frac{\partial T}{\partial y} \right)_{y=0}. \quad (2.29)$$

Applying the transformations (2.22), we have

$$\begin{aligned} Re^{1/2} C_{fx} & = f''(0) [\beta^* + (1 - \beta^*) \{1 - We f''(0)\}^{-1}], \\ Re_x^{-1/2} Nu_x & = -[1 + Rd \{1 + (\theta_w - 1)\theta(0)\}^3] \theta'(0), \end{aligned} \quad (2.30)$$

where $Re_x \left(= \frac{xU_w}{\nu} \right)$ being the local Reynolds number.

2.4 Numerical Implementation

The system of ordinary differential Eqs. (2.23) and (2.24) are highly nonlinear and partially coupled. Therefore, it is quite difficult to obtain their analytical or exact solutions. Thus a numerical treatment would be more appropriate. Hence, the governing equations (2.23) and (2.24) having the boundary conditions (2.25) and (2.26) are numerically integrated by adopting shooting algorithm coupled with the Runge-Kutta Fehlberg integration scheme.

The Runge-Kutta Fehlberg method is a numerical technique which can be applied to solve the first order ODEs of the form:

$$\frac{dy}{dx} = f(x, y), \quad y(x_i) = y_i.$$

Before applying the Runge-Kutta Fehlberg scheme, at a very first step, we reduce the non-linear differential structure into simultaneous differential structure of first order. The governing equations (2.23) and (2.24) are transformed to a set of five first order ODEs containing five unknowns. In this regard, we introduce the new variables:

$$f = u_1, \quad f' = u_2, \quad f'' = u_3, \quad \theta = u_4, \quad \theta' = u_5. \quad (2.31)$$

By practising the above variables, we get:

$$u_1' = u_2, \quad (2.32)$$

$$u_2' = u_3, \quad (2.33)$$

$$u'_3 = \frac{-u_1 u_3 - u_2^2 - A(u_2 + \frac{\eta}{2} u_3)}{[\beta^* + (1 - \beta^*)(1 - We u_3^2)]^{-2}}, \quad (2.34)$$

$$u'_4 = u_5, \quad (2.35)$$

$$u'_5 = \frac{\left[-3 [1 + R_d(\theta_w - 1)u_4]^2 R_d(\theta_w - 1)u_5^2 - \text{Pr}(u_1 u_5 - 2u_1 u_4) + \text{Pr} \frac{A}{2} \{ \eta u_5 + 3u_4 \} - \text{Pr} \delta u_3 \right]}{[1 + R_d(\theta_w - 1)u_4]^3}. \quad (2.36)$$

Subsequently, the homologous modulated boundary conditions (BCs) take the form:

$$u_1 = 0, \quad u_2 = 1, \quad u_2 = \xi_1, \quad u_5 = -\gamma(1 - u_4), \quad u_5 = \xi_2. \quad (2.37)$$

To acquire the numerical solution of above non-linear system (2.32) and (2.36) along with initial conditions (2.37), we need the values of unknown initial conditions ξ_1 and ξ_2 . Since the values of ξ_1 and ξ_2 are not prescribed, we use the multiple shooting method to find these unknown initial values i.e., $f''(0)$ and $\theta'(0)$. To do this, we have to shoot these initial conditions with a systematic guessing such that the solution satisfies the given far field boundary conditions (2.36). A hit and trail method is exercised in order to find these values. An important aspect of shooting technique is to chose the appropriate value of η_∞ . Let the range of numerical integration to be finite dimensions i.e., $\eta_\infty = 10$. We then compare the calculated values of $f'(\eta)$ and $\theta(\eta)$ at $\eta_\infty = 10$ with the given boundary conditions $f'(\eta_\infty) = 1$ and $\theta(\eta_\infty) = 0$, and adjust the values of $f''(0)$ and $\theta'(0)$ using the Newton's method to give a better approximation to the solution. The step-size is chosen to be $\Delta\eta = 0.01$. We obtained the numerical solution with the convergence criterion of 10^{-6} in all cases.

2.4.1 Validation of Numerical Scheme

In order to examine the validity of our utilized code, a comparison of computed results is made with the previously published studies. **Table 2.1** elucidates a comparison regarding the numerical results for $f''(0)$ for varying A when $We = 0$ and $\beta^* = 0$ with those of Sharidan *et al.* [96], Chamkha *et al.* [97] and Khan and Azam [98]. It can be found from this table that these outcomes are observed in better agreement. **Table 2.2** provides a comparison regarding numerical outcomes of local Nusselt number ($Re_x^{-\frac{1}{2}} Nu_x$) for distinct Prandtl number (Pr), when $We = 0, \beta^* = 0, \theta_w = 0, R_d = 0, \delta = 0$ and $A = 0$, with published works of Grubka and Bobba [99] and Chen [100] with a superb agreement.

2.5 Physical Description

This section emphasizes on the numerical outcomes for distinct physical parameters namely, unsteadiness parameter A , Prandtl number Pr , local Weissenberg number We , viscosity ratio parameter β^* , radiation parameter R_d , heat sink/source parameter δ , temperature ratio parameter θ_w and Biot number γ . The characteristics of these parameters versus velocity and temperature distributions are exposed graphically. We have selected fixed values to these parameters in the whole analysis as: $We = 1.0, \beta^* = 0.2, \theta_w = 1.2, R_d = 1.3, \delta = 0.2, \gamma = 0.3, Pr = 0.72$ and $A = 0.4$.

The variation in $f'(\eta)$ and $\theta(\eta)$ for distinct values of A are sketched in **Figs. 2.2(a, b)**. From these plots, it is observed that the fluid velocity and temperature decrease for higher A . Further, when A increases, the fluid velocity and temperature diminishes. From physical perspective, as A increases the fluid temperature decreases due to less amount of heat transfer

from plate to the fluid. In **Figs. 2.3(a, b)**, the physical behavior of boundary layer near to the wall can be seen by observing the velocity and temperature graphs, respectively. These sketches demonstrate that how the velocity and temperature fields are effected by β^* . It also explain that $f'(\eta)$ increases by rising β^* while reverse pattern is seen for associated thermal boundary layer thickness.

Figs. 2.4(a, b) are outlined to describe the impact of We on $f'(\eta)$ and $\theta(\eta)$. From the output of these figures, it can be seen that fluid velocity decreases by higher We . It also results a decline in the momentum boundary layer thickness. However, a reverse trend is witnessed for the fluid temperature. Physically, the relaxation time is increased for greater We which diminishes the liquid velocity and enhances the fluid temperature. **Fig. 2.5(a)** reveals the deviation in the temperature field in response to change in heat generation parameter ($\delta > 0$). It is noticed that the fluid temperature and allied thickness of layer enhances with larger heat generation parameter. In fact, the heat generation parameter ($\delta > 0$) yields an additional heat that causes an increment in the thickness of thermal boundary layer. **Fig. 2.5(b)** depicts the effect on temperature profiles for heat absorption parameter ($\delta < 0$). It can be viewed that the fluid temperature reduces subject to higher heat absorption parameter ($\delta < 0$). The impact of R_d and θ_w on $\theta(\eta)$ are plotted through **Figs. 2.6(a, b)**. These graphs reveal that larger values of R_d and θ_w have the affinity to improve the temperature distribution and the thickness of thermal boundary layer. Physically, an increment in radiation parameter yields lower mean absorption coefficient. Therefore, radiative heat transport rate to the fluid enhances. Moreover, the larger values of temperature ratio parameter show that $T_w > T_\infty$ which rise the fluid thermal state and produces an increment in temperature field. **Figs. 2.7(a, b)** elaborate the impact of Pr and γ on $\theta(\eta)$. The temperature field decreases with higher Pr . The main reason behind

this fact is that the fluid with high Prandtl number has slow rate of thermal diffusion and therefore lower the conduction and the thickness of thermal boundary layer while an opposite behavior is seen for Biot number. Therefore, the larger Biot number leads to uplift the wall temperature and the thickness of thermal boundary layer. To ensure the authenticity of current numerical computations, a comparison by bvp4c and shooting methods are portrayed in **Fig. 2.8**. A remarkable agreement between the two computational techniques is found. It indicates that the obtained results in this chapter are reliable and correct. The numerical outcomes of $Re^{1/2}C_{fx}$ and $Re^{-1/2}Nu_x$ are also formulated in **Tables 2.3** and **2.4** for some physical parameters. The variations subject to numerous values of A , β^* and We on $Re^{1/2}C_{fx}$ are depicted in **Table 2.3**. It is fascinating to notice that by uplifting the Weissenberg number the shear stress at the wall decreases. Further, from **Table 2.4**, it is momentous to mention that the rate of heat transfer is enhanced with greater Prandtl number. Additionally, it is observed that larger values of γ , R_d and θ_w enhance the heat transport rate.

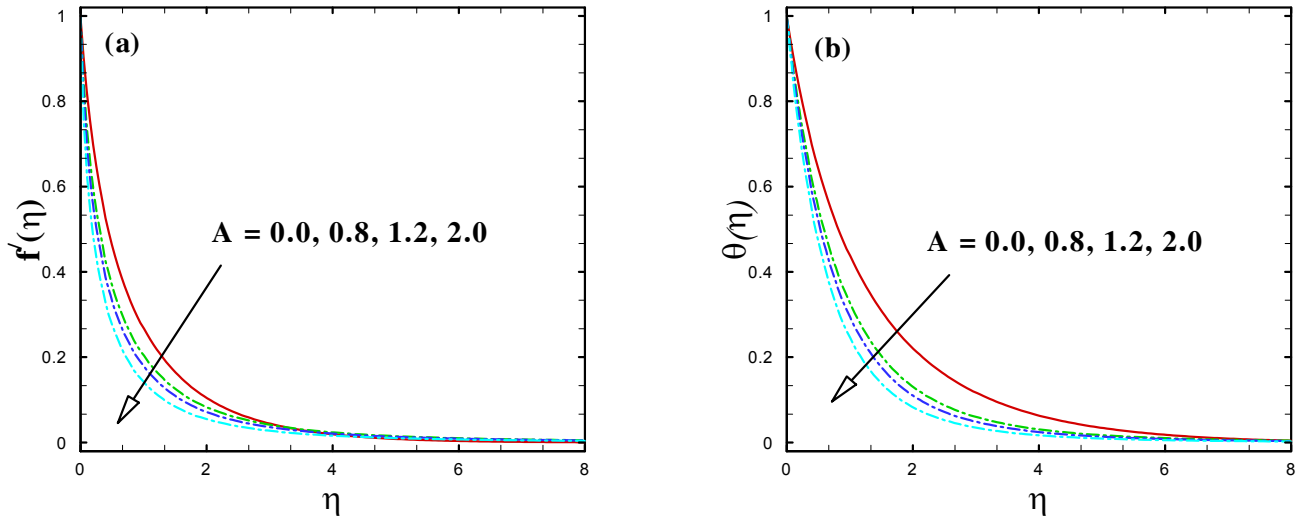


Fig. 2.2 : Impact of $f'(\eta)$ and $\theta(\eta)$ for various A .

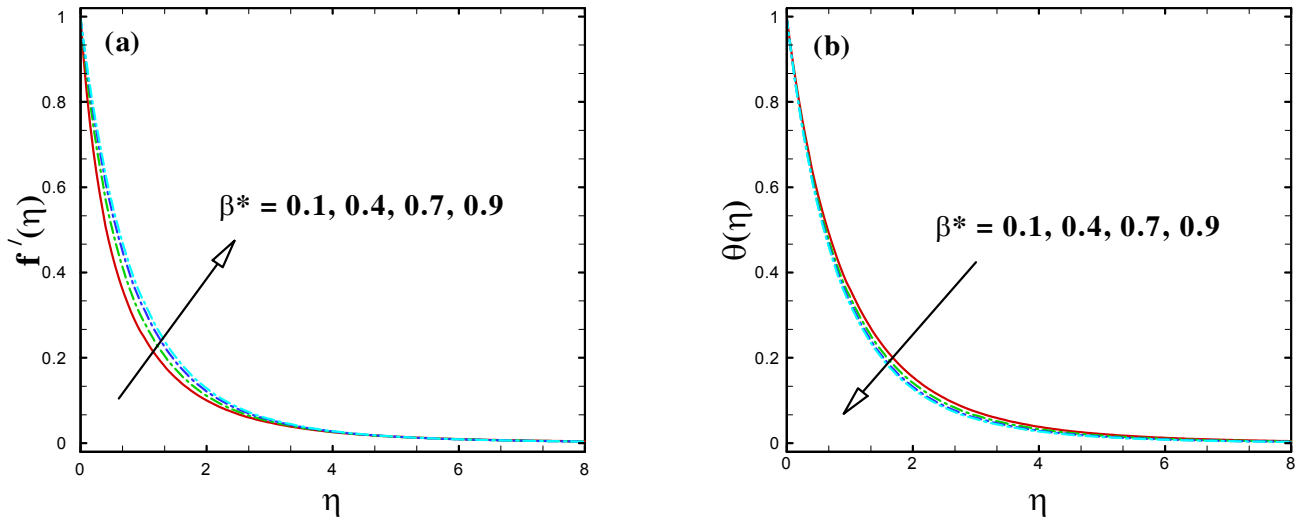


Fig. 2.3 : Impact of $f'(\eta)$ and $\theta(\eta)$ for various β^* .

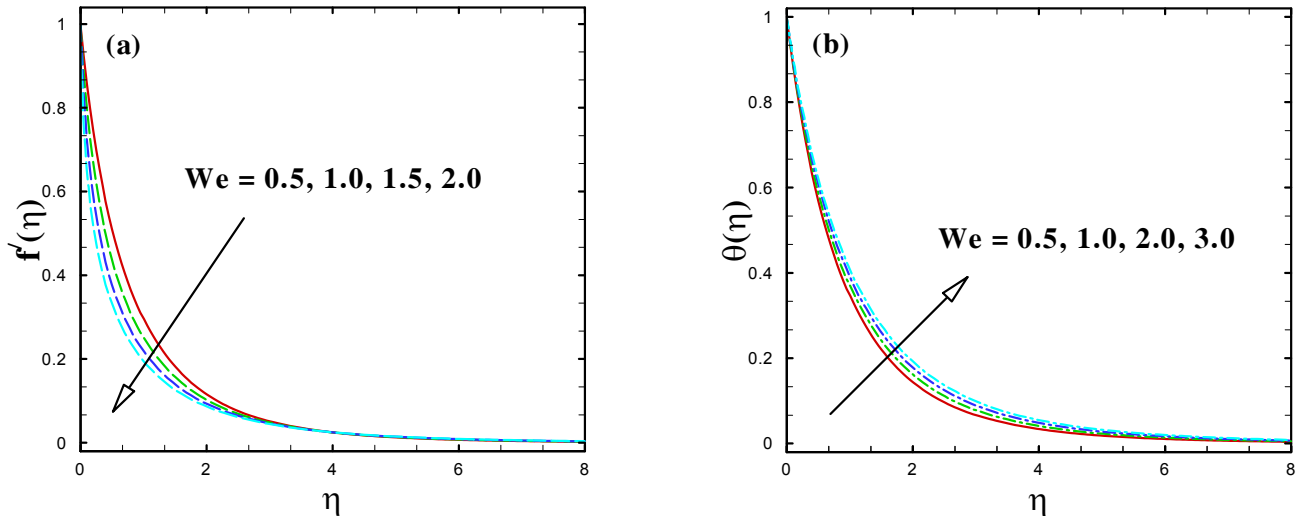


Fig. 2.4 : Impact of $f'(\eta)$ and $\theta(\eta)$ for various We .

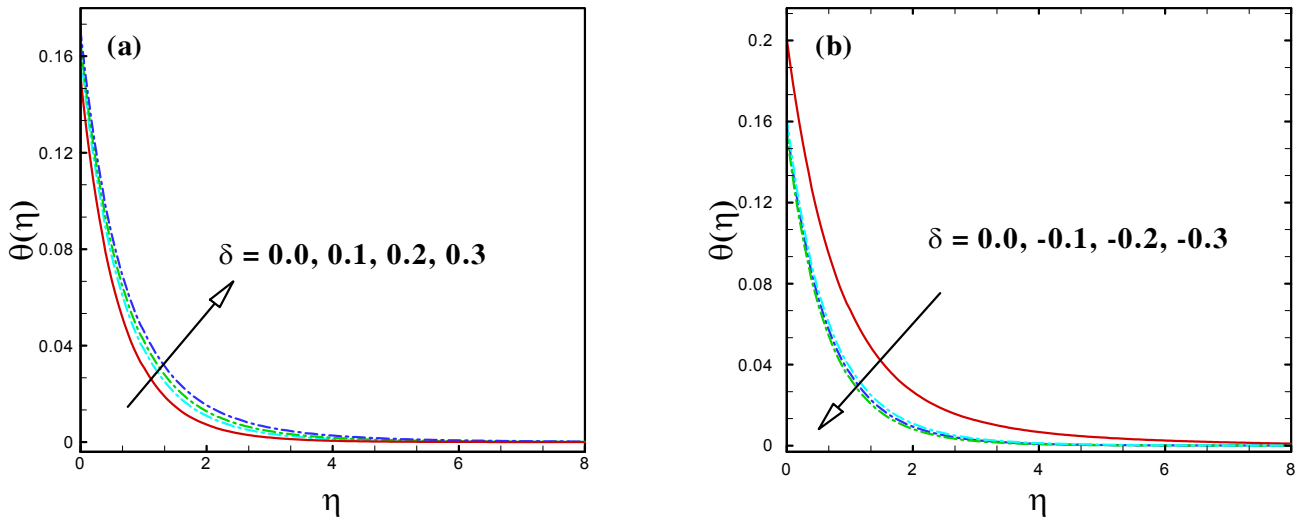


Fig. 2.5 : Impact of $\theta(\eta)$ for various $\delta > 0$ and $\delta < 0$.

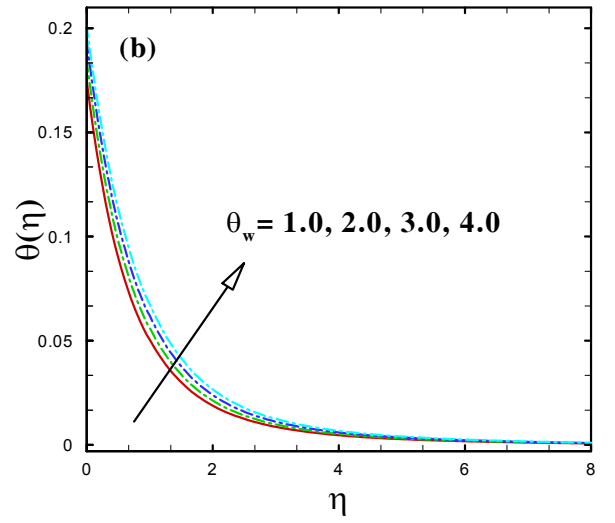
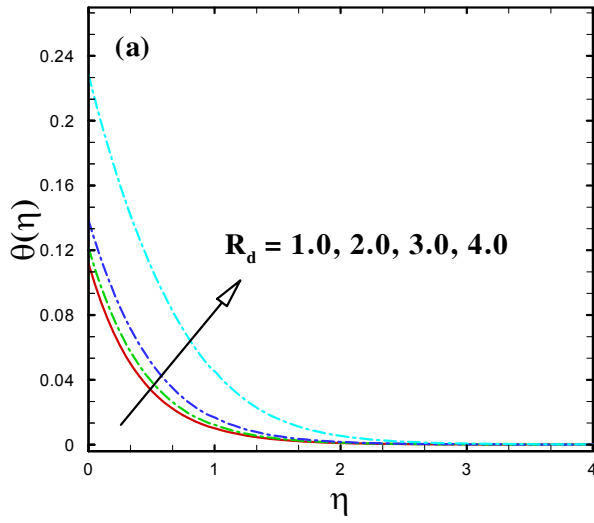


Fig. 2.6 : Impact of $\theta(\eta)$ for various R_d and θ_w .

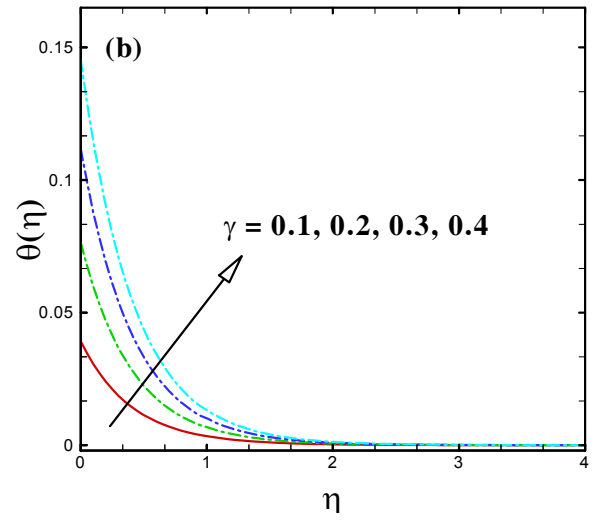
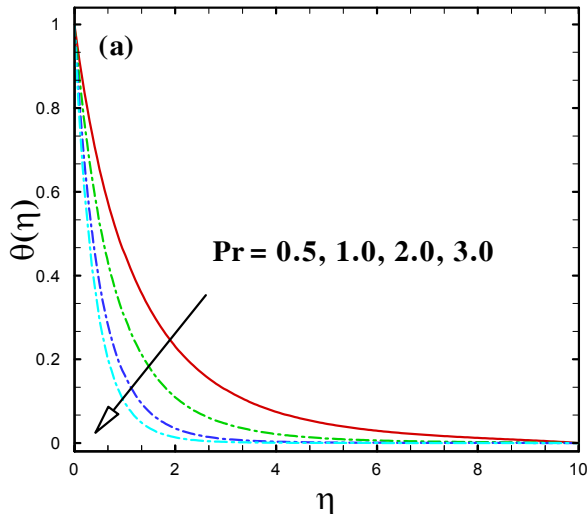


Fig. 2.7 : Impact of $\theta(\eta)$ for various Pr and γ .

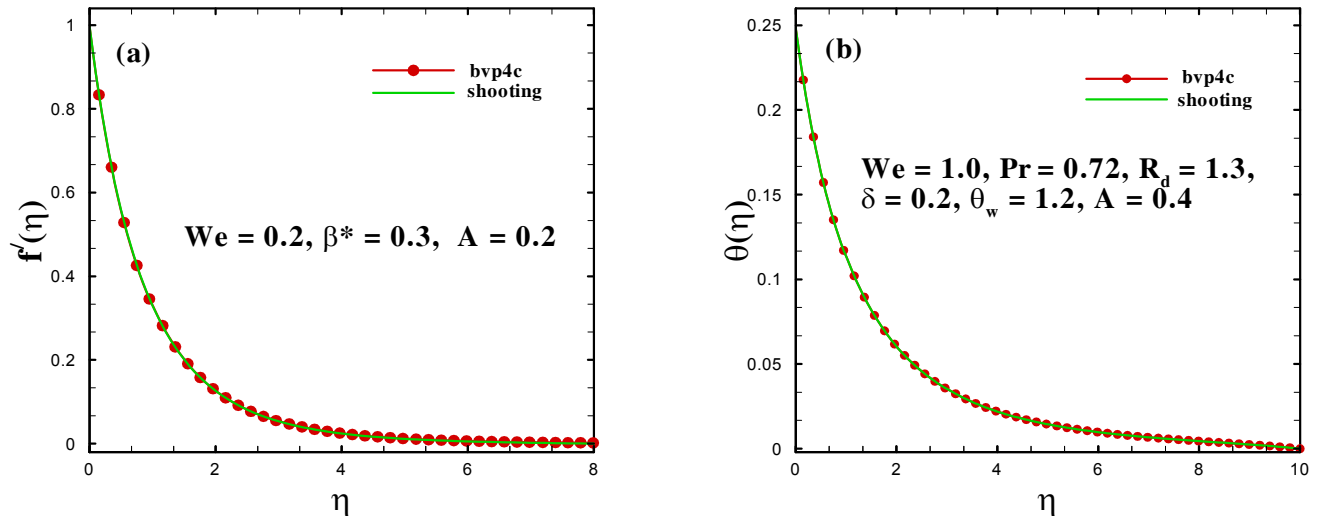


Fig. 2.8 : A comparison between bvp4c and shooting methods for $f'(\eta)$ and $\theta(\eta)$.

Table 2.1: Comparison for numerical outcomes of $f''(0)$ for various A , for Newtonian fluid.

A	Sharidan <i>et al.</i> [96]	Chamkha <i>et al.</i> [97]	Khan and Azam [98]	Present work
0.8	-1.2610420	-1.2615120	-1.2610430	-1.2610427
1.2	-1.3777220	-1.3780520	-1.3777240	-1.3777238

Table 2.2 : A comparison between the results of $-\theta'(0)$ for various Prandtl number (Pr) when $We = 0$, $\beta^* = 0$, $\theta_w = 0$, $R_d = 0$, $\delta = 0$ and $A = 0$.

Pr	Grubka and Bobba [99]	Chen [100]	Present work
0.72	1.08850	1.088530	1.0886210
1.00	1.33330	1.333340	1.3333335
3.00	2.50970	2.509720	2.5096981
10.0	4.79690	4.796860	4.7968527

Table 2.3: Computed values of $Re_x^{1/2}C_{fx}$ for various A , We and β^* when $Pr = 0.72$.

A	We	β^*	$-Re^{1/2}C_{fx}$
0	3.0	0.2	0.33979494
0.5			0.35138616
1.0			0.35966403
2.0			0.37186619
1.0	0.5		1.0448919
	1.0		0.81338758
	2.0		0.50549252
	3.0		0.35966403
		0.2	1.0255021
		0.4	1.2987835
		0.6	1.5027336
		0.8	1.6710805

Table 2.4: Computed values of $Re_x^{-1/2}Nu_x$ for varying R_d, θ_w, γ and Pr when $We = 1.0$, $A = 0.2$, $\delta = 0.3$ and $\beta^* = 0.2$.

R_d	θ_w	γ	Pr	$Nu_x Re_x^{-\frac{1}{2}}$
0.5	1.2	0.3	1.0	0.632107
1.0				0.882219
1.5				1.12095
2.0				1.34567
0.5	1.5			0.632107
	1.7			0.669341
	2.0			0.736606
	1.2	0.5		0.586143
		0.7		0.752486
		1.0		0.954415
		0.3	1.3	0.386056
			1.7	0.394549
			2.0	0.399100

Chapter 3

Unsteady Heat Transfer in

Williamson Fluid Flow past a Wedge

In this chapter, a mathematical formulation for the transient Falkner-Skan Williamson fluid flow and heat transfer is presented. Firstly, the governing flow equations are formulated for current model in terms of PDEs. The transformed non-linear ODEs are solved numerically by employing Runge-Kutta-Fehlberg method. The features of pertinent parameters are explored by observing the non-dimensional velocity and temperature fields. The coefficients of skin-friction and Nusselt number are illustrated by means of tables. The outcomes declare that rate of heat transport is accelerated with a rise in unsteadiness and wedge angle parameters. It is also noticed that the viscosity ratio parameter enhances the fluid velocity.

3.1 Physical Problem Description

A schematic view and geometrical configuration of the physical model is illustrated in **Fig. 3.1**.

In this analysis, we have considered the time-dependent flow of a Williamson fluid model due

to stretching wedge. The stretching velocity of the wedge is denoted by $U_w(x, t) = \frac{bx^m}{1-ct}$, in which b signifies the stretching rate and c the dimensional constant with dimension $(\text{time})^{-1}$. Additionally, the flow moves along the axis of wedge in the upward direction with a free stream velocity $U_e(x, t) = \frac{ax^m}{1-ct}$, where a , c and m are positive constants with $0 \leq m \leq 1$. The total wedge angle is supposed to be $\Omega = \beta\pi$, where $\beta = \frac{2m}{m+1}$ is associated with the pressure gradient. To investigate the heat transfer, we have taken the temperature at the surface of wedge as $T_w(x, t) = T_\infty + \frac{T_0 U_w x}{\nu \sqrt{1-ct}}$, where T_0 represent the initial reference and T_∞ the free stream temperature, respectively, when y approaches infinity.

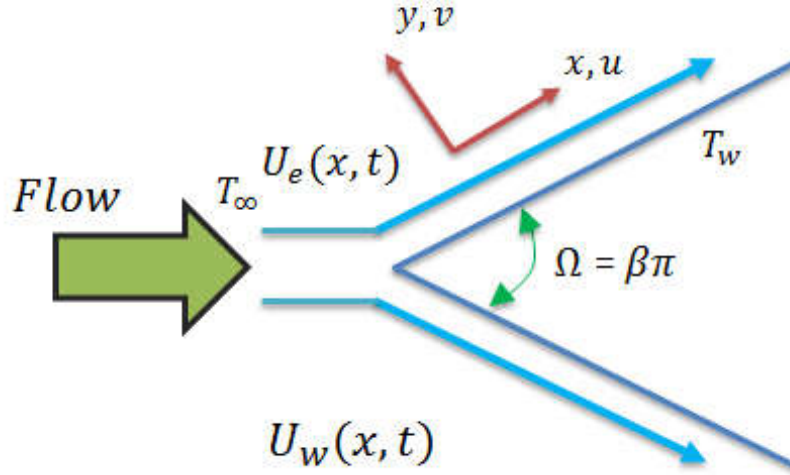


Fig. 3.1: Physical sketch of considered problem.

The continuity equation can be written as:

$$\frac{\partial u}{\partial x} + \frac{\partial v}{\partial y} = 0. \quad (3.1)$$

The momentum equation after employing the usual boundary layer approximations for Williamson fluid without viscous dissipation and external force can be expressed as:

$$\begin{aligned} \frac{\partial u}{\partial t} + u \frac{\partial u}{\partial x} + v \frac{\partial u}{\partial y} &= \frac{\partial U_e}{\partial t} + U_e \frac{\partial U_e}{\partial x} + \nu \frac{\partial^2 u}{\partial y^2} \left[\beta^* + (1 - \beta^*) \left(1 - \Gamma \frac{\partial u}{\partial y} \right)^{-1} \right] \\ &+ \nu \Gamma \left(\frac{\partial u}{\partial y} \right) \left(\frac{\partial^2 u}{\partial y^2} \right) \left[(1 - \beta^*) \left(1 - \Gamma \frac{\partial u}{\partial y} \right)^{-2} \right]. \end{aligned} \quad (3.2)$$

The energy equation for time dependent flow receipts the form:

$$\frac{\partial T}{\partial t} + u \frac{\partial T}{\partial x} + v \frac{\partial T}{\partial y} = \alpha \frac{\partial^2 T}{\partial y^2}. \quad (3.3)$$

It is worth mentioning that the Eq. (3.2) of Williamson fluid reduces to Newtonian fluid case when $\beta^* = 0$ and $\Gamma = 0$.

We have applied the no-slip conditions at the surface of the wedge along with the flow conditions which are given as follow:

(a) On the wedge surface *i.e.*, at $y = 0$:

$$u = U_w(x, t), \quad v = 0, \quad T = T_w(x, t). \quad (3.4)$$

(b) At free stream *i.e.*, as $y \rightarrow \infty$:

$$u \rightarrow U_e, \quad T \rightarrow T_\infty. \quad (3.5)$$

Using dimensionless variables

$$\eta = y \sqrt{\frac{(m+1)U_e}{2\nu x}}, \quad \psi(x, y, t) = \sqrt{\frac{2\nu x U_e}{m+1}} f(\eta), \quad \theta(\eta) = \frac{T - T_\infty}{T_w - T_\infty}. \quad (3.6)$$

On substituting the above defined non-dimensional parameters into Eqs. (3.2) and (3.3), we get the accompanying nonlinear ordinary differential equations:

$$\left[\beta^* + (1 - \beta^*) (1 - W_e f'')^{-2} \right] f''' + f f'' + \beta (1 - (f')^2) - A(2 - \beta) \left(f' + \frac{\eta}{2} f'' - 1 \right) = 0, \quad (3.7)$$

$$\theta'' + \text{Pr} (f\theta' - 2f'\theta) - \text{Pr} \frac{A}{2} (2 - \beta) (\eta\theta' + 3\theta) = 0, \quad (3.8)$$

with reduced boundary conditions:

$$f(0) = 0, \quad f'(0) = \lambda, \quad \theta(0) = 1, \quad (3.9)$$

$$f'(\infty) \rightarrow 1, \quad \theta(\infty) \rightarrow 0. \quad (3.10)$$

Here, $\lambda = \frac{b}{a}$ denotes the wedge moving parameter and $\lambda > 0$ the stretching and $\lambda < 0$ the shrinking wedge, respectively, while $\lambda = 0$ for a static wedge. The other involved physical dimensionless variables are given by:

We ($= \sqrt{\frac{\Gamma^2(m+1)U_\infty^3}{2\nu x}}$) is the local Weissenberg number, A ($= \frac{c}{ax^{m-1}}$) the unsteadiness parameter, Pr ($= \frac{\mu C_p}{k}$) the Prandtl number and β ($= \frac{2m}{m+1}$) the wedge angle parameter.

3.1.1 Quantities of Physical Interest

The imperative physical parameters are skin friction and Nusselt number that are elaborated as:

$$C_{fx} = \frac{\tau_w}{\rho u_w^2}, \quad Nu_x = \frac{xq_w}{k(T_w - T_\infty)}, \quad (3.11)$$

where τ_w and q_w are expressed as

$$\tau_w = \mu_0 \frac{\partial u}{\partial y} \left[\beta^* + (1 - \beta^*) \left(1 - \Gamma \frac{\partial u}{\partial y} \right)^{-1} \right], \quad q_w = -k \left(\frac{\partial T}{\partial y} \right) \Big|_{y=0}. \quad (3.12)$$

Invoking (3.6) and (3.12), we get

$$\begin{aligned} \text{Re}^{1/2} C_{fx} &= \frac{1}{\sqrt{2-\beta}} f''(0) [\beta^* + (1-\beta^*) \{1 - We f''(0)\}^{-1}], \\ \text{Re}^{-1/2} Nu_x &= -\frac{1}{\sqrt{2-\beta}} \theta'(0). \end{aligned} \quad (3.13)$$

3.2 Numerical Procedure

The numerical computations of the governing ordinary differential Eqs. (3.7) – (3.10) are obtained with the aid of Runge-Kutta Fehlberg integration scheme. This governing problem [(3.7) – (3.10)] constitutes a one-parameter two-point boundary value problem and is solved numerically. We need to change the modelled ODEs into a set of first-order in terms of new dependent variables as:

$$f' = p, \quad p' = q, \quad q' = \frac{-fq - \beta(1-q^2) + A(2-\beta)(p + \frac{\eta}{2}q - 1)}{[\beta^* + (1-\beta^*)(1 - We q)^{-2}]}, \quad (3.14)$$

$$\theta' = s, \quad s' = -\text{Pr}(fs - 2p\theta) + \text{Pr} \frac{A}{2}(2-\beta)(\eta p + 3\theta), \quad (3.15)$$

and associated boundary condition becomes

$$f(0) = 0, \quad p(0) = \lambda, \quad \theta(0) = 1, \quad p(\infty) = \xi_1 \quad \text{and} \quad \theta(\infty) = \xi_2. \quad (3.16)$$

To get the numerical solutions for the system of Eqs. (3.14) and (3.15) with conditions (3.16) by employing Runge-Kutta Fehlberg technique coupled with shooting iterative method, we have to find the values of unknown ξ_1 and ξ_2 . The unknown values are approximated by Newton

iterative method. In this study, the suitable finite value of $\eta \rightarrow \infty$, say η_∞ is taken to be 10. The computer software MATLAB is utilized for computational work. A step size of $\Delta\eta = 0.01$ has been acceptable for a convergence criterion of 10^{-6} in all cases.

3.2.1 Testing of the Code

To demonstrate the validity of accomplished numerical outcomes, a correlation with earlier published work is elaborated in limiting cases. The acquired results of $\text{Re}^{1/2} C_{fx}$ for specific β are compared with those published by Rajagopal *et al.*[84], Kuo [101] and Ishaq *et al.*[102], (see **Table3.1**). A perfect compatibility with the results of the aforementioned authors is noted.

3.3 Results and Discussion

Here, the time dependent flow and heat transport features of Williamson fluid towards moving wedge are numerically investigated. The current section focuses on the obtained numerical results which are manifested through **Figs. 3.2–3.6** for dimensionless velocity and temperature fields for various numerical values of leading parameters that are the local Weissenberg number We , viscosity ratio parameter β^* , wedge angle parameter β , moving wedge parameter λ and Prandtl number Pr .

The outcomes of unsteadiness parameter A versus velocity $f'(\eta)$ and temperature $\theta(\eta)$ fields are plotted in **Fig. 3.2(a)** and **Fig. 3.2(b)**. From these plots, it is examined that a rise in unsteadiness parameter augments the velocity field, whereas a depreciation in temperature profile is noted. We have plotted these graphs for static and moving wedge parameter. Here, $\lambda = 0$ relates to the static wedge and $\lambda = 0.3 > 0$ represents a moving wedge. Therefore, it is revealed that fluid velocity is lower for stretching wedge in comparison to a static wedge while

a reverse trend is seen for temperature profiles. Also, the thickness of both layers (momentum and thermal) reduces for higher unsteadiness parameter A . Physically, when A increases then the wedge releases heat and the fluid temperature declines.

Figs. 3.3(a) and **3.3(b)** demonstrate the variation of $f'(\eta)$ and $\theta(\eta)$ for varying moving wedge parameter λ for $\beta = 0$ and $\beta = 1$. It can be concluded from **Fig. 3.3(a)** that velocity distribution elaborates a growing behavior for uplifting values of moving wedge parameter λ for both the cases. In addition, the thickness of momentum boundary layer reduces for higher λ . An increment in the moving wedge parameter leads to depreciate the temperature distribution, as seen in **Fig. 3.3(b)**. The thickness of thermal boundary layer also reduces for greater moving wedge parameter.

The behavior of wedge angle parameter β against fluid velocity and temperature inside the boundary layer are demonstrated in **Figs. 3.4(a)** and **3.4(b)**. Here, $\lambda = 0$ means a static wedge and $\lambda = 0.3 > 0$ shows a moving wedge, respectively. From these figures, it is noticed that the behavior of wedge parameter is comparable to unsteadiness parameter A i.e., fluid velocity enhances while temperature diminishes for higher β . The reason behind this fact is that wedge angle parameter β demonstrates pressure gradient. Thus, positive values of β relate to adequate pressure gradient which rises the flow.

The variation of $f'(\eta)$ and $\theta(\eta)$ for varying β^* are presented in **Figs. 3.5(a)** and **3.5(b)**. We examined a dependency of velocity and temperature fields on β^* . Further, $\beta = 0$ relates to zero degree wedge angle (flow by flat plate) and $\beta = 1$ corresponds to 90 degree wedge angle (stagnation-point flow). When β^* intensify the velocity profile increases and diminishes for temperature profile. Moreover, the fluid velocity is higher in case of flow near stagnation point in comparison with flow over a flat plate. For higher β^* , thickness of both boundary layers

(momentum and thermal) reduces remarkably.

The impact of We on dimensionless velocity and temperature profiles by keeping the other parameters fixed is portrayed in **Figs. 3.6(a)** and **3.6(b)**. From these figures, we found that velocity field rises whereas temperature field decreases by rising the Weissenberg number. Clearly, thickness of momentum and thermal layers are reducing function of Weissenberg number.

Table 3.2 demonstrates the characteristics of unsteadiness parameter A , wedge angle parameter β , viscosity ratio parameter β^* and moving wedge parameter λ on $Re^{1/2}C_{fx}$ and $Re^{-1/2}Nu_x$. Here, $Re^{1/2}C_{fx}$ and $Re^{-1/2}Nu_x$ enhance by rising A . It is further seen that shear stress at the wall is a decaying function of β and λ . We further found that the rate of heat transfer is a reducing function of β .

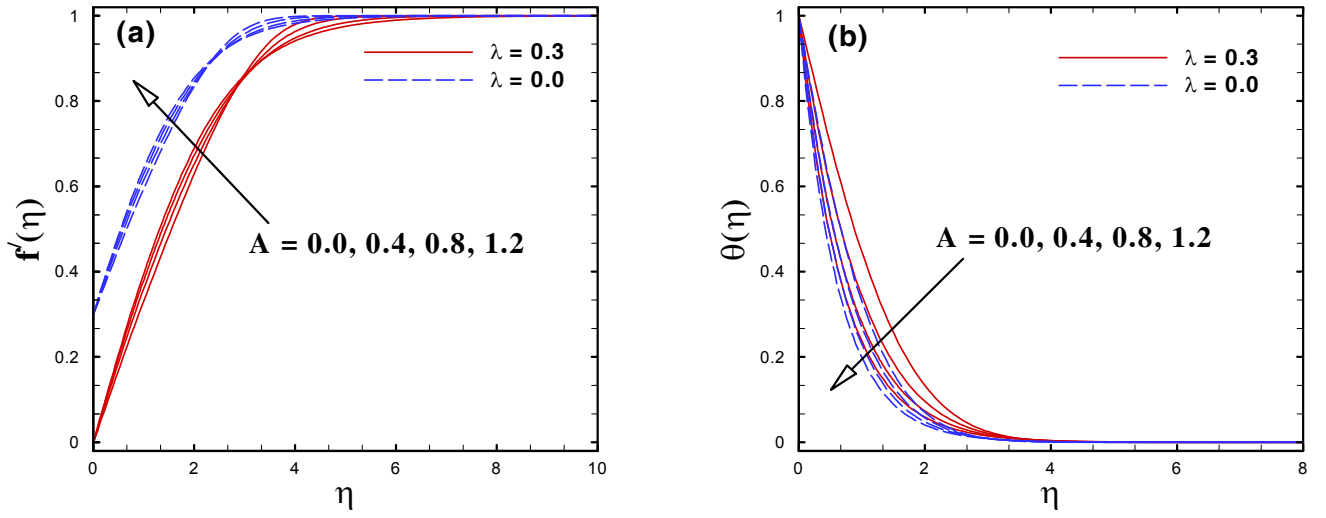


Fig. 3.2: Impact of A on $f'(\eta)$ and $\theta(\eta)$.

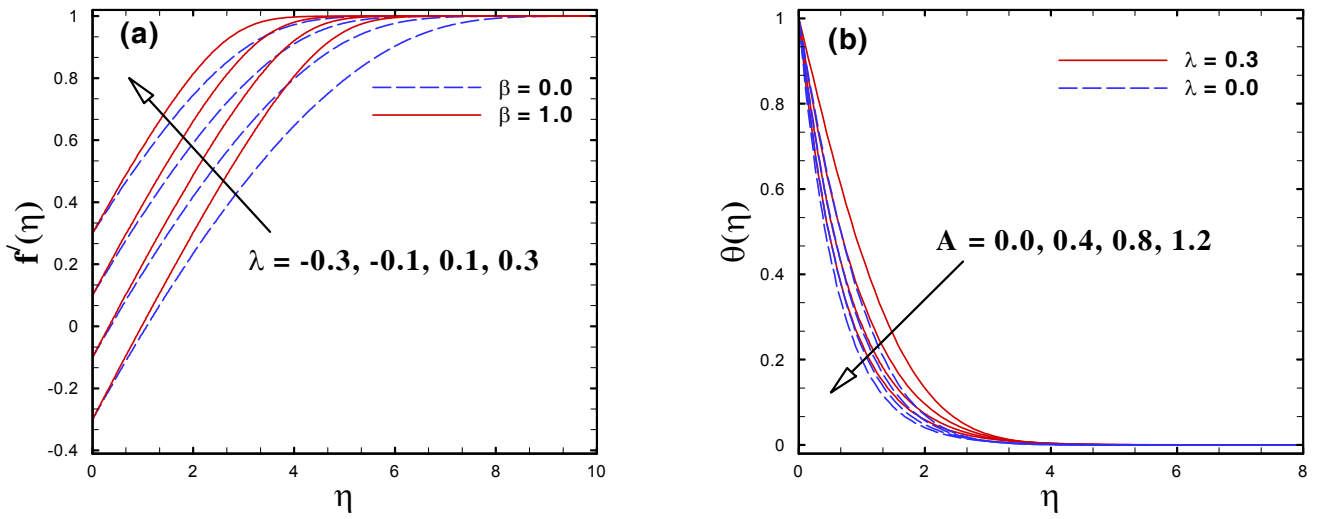


Fig. 3.3: Impact of λ on $f'(\eta)$ and $\theta(\eta)$.

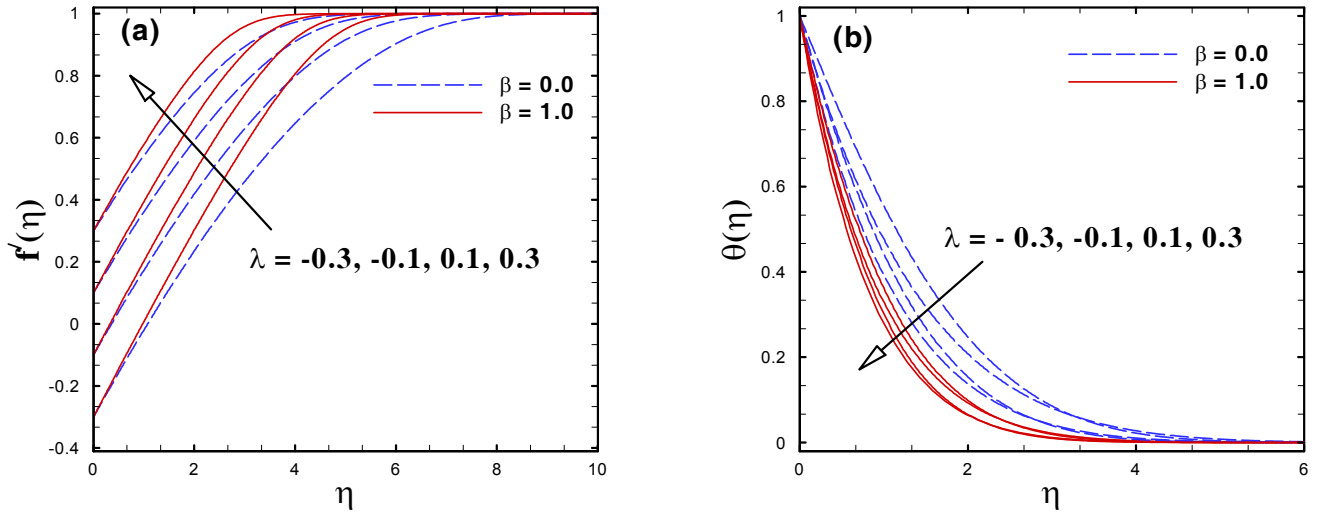


Fig. 3.4: Impact of β on $f'(\eta)$ and $\theta(\eta)$.

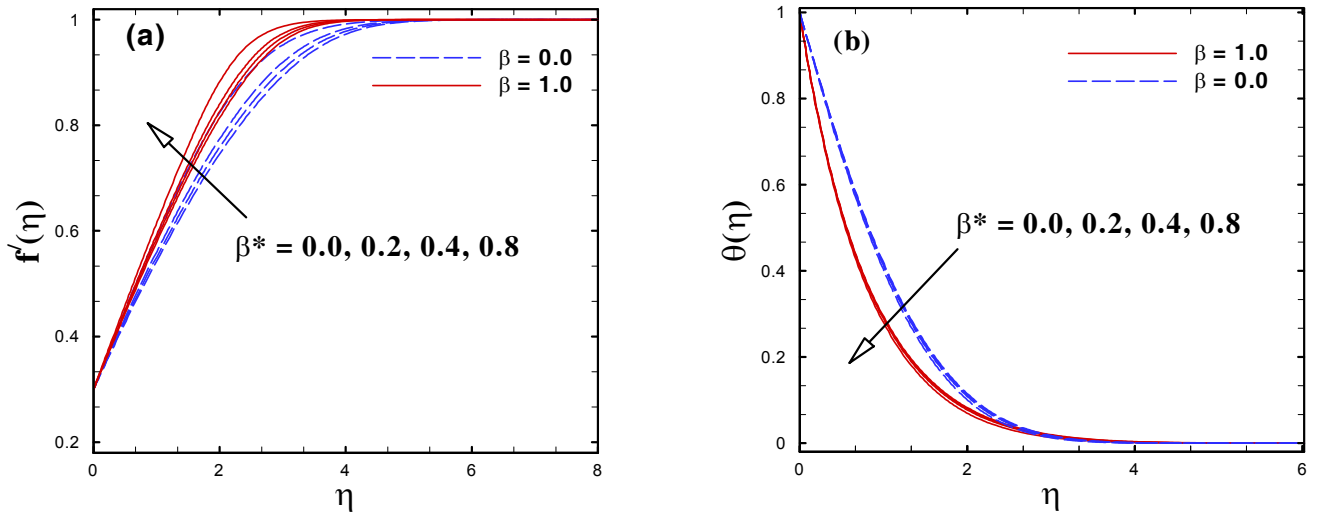


Fig. 3.5: Impact of β^* on $f'(\eta)$ and $\theta(\eta)$.

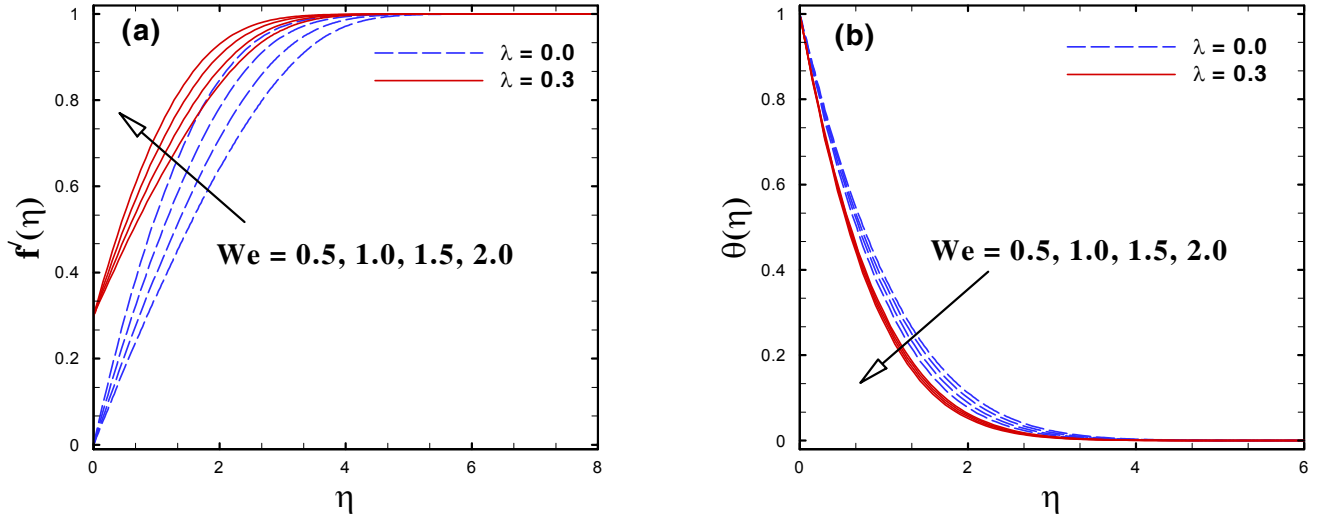


Fig. 3.6: Impact of We on $f'(\eta)$ and $\theta(\eta)$.

Table 3.1: A comparison of $-f''(0)$ for varying β when $We = \beta^* = 0$.

β	Rajagopal <i>et al.</i> [84]	Kuo [101]	Ishak <i>et al.</i> [102]	Present study
0.0	—	0.469600	0.46960	0.469601
0.1	0.587035	0.587880	0.58700	0.587036
0.3	0.774755	0.775524	0.77480	0.774754
0.5	0.927680	0.927905	0.92770	0.92768
1.0	1.232585	1.231289	1.23260	1.232588

Table 3.2: Numerical outcomes of $Re^{1/2}C_{fx}$ and $Re^{-1/2}Nu_x$ for varying β^* , β , λ and A when $We = 2.0$ and $Pr = 1.0$.

β^*	β	λ	A	$(2 - \beta)^{1/2} Re^{1/2} C_{fx}$	$(2 - \beta)^{1/2} (Re_x)^{-1/2} Nu_x$
0.0	0.3	0.2	0.1	1.15746	1.03699
	0.2			1.11757	1.04193
	0.4			1.07167	1.04803
	0.8			0.943644	1.06788
0.2	0.3	0.2	0.1	0.15728	0.03701
	0.5			1.40549	1.03412
	0.8			1.75955	1.02657
	1.0			1.9872	1.02021
0.2	0.3	-0.3	0.1	1.62985	0.37401
		-0.2		1.58455	0.539636
		0.0		1.41105	0.813351
		0.2		1.15728	1.03701
0.2	0.3	0.2	0.0	1.06074	0.94192
			0.2	1.25376	1.12634
			0.3	1.35024	1.21069
			0.4	1.44669	1.29069

Chapter 4

Transient Flow of Magneto-Williamson Nanofluid due to Wedge

The intention of this chapter is to elaborate the Falkner-Skan Williamson nanofluid flow caused by a moving/static wedge by considering magnetic effect. Further, the convective heat transfer mechanism for flow is also investigated. Compatible transformations convert the PDEs into ODEs. The ensuing ODEs are computed via Runge-Kutta Fehlberg integration procedure featuring a shooting technique. Computations are presented for the dimensionless velocity, temperature and nanoparticles concentration fields, the skin friction, reduced heat and mass transport coefficients for pertinent physical parameters. The rise in the amount of convective parameter has caused a rise in the fluid temperature. The rate of heat transfer is examined to be increased as a result of Brownian motion and thermophoresis parameters enhancement. Besides, the validity of present code is validated through comparison with earlier published

works and found to be in superb agreement.

4.1 Mathematical Analysis

We formulated a transient incompressible flow of Williamson fluid past a wedge shaped geometry. The heat and mass transfer characteristics of stagnation-point flow of MHD Williamson nanofluid are investigated. The stretching and free stream velocities are $U_w(x, t) = \frac{bx^m}{1-ct}$, $U_e(x, t) = \frac{ax^m}{1-ct}$, respectively, where (a, b, c and $m > 0$), with $0 \leq m \leq 1$. Here, magnetic field $B(t) = \frac{B_0}{(1-ct)^{1/2}}$ is applied normal to the flow field. The physical layout of the current model is illustrated in **Fig. 4.1**. In addition, the wedge surface is heated through convection process via hot liquid with temperature T_f which yields a coefficient of heat transfer h_f .

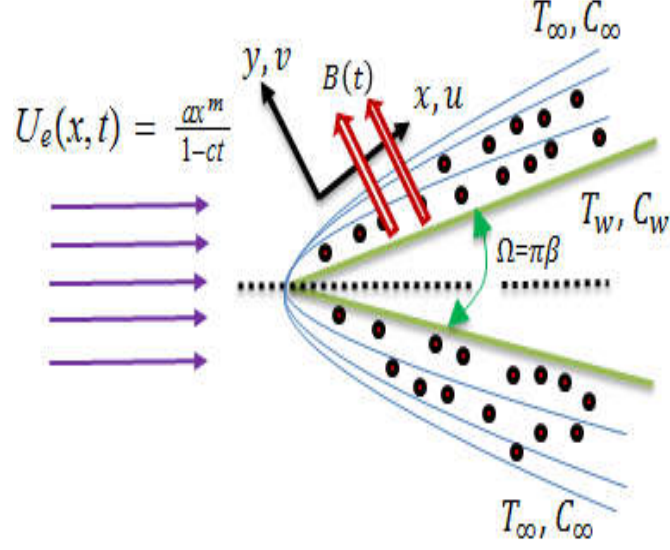


Fig. 4.1: Physical sketch of the flow configuration.

The governing equations for Williamson nanofluids are finalized by implementing the Oberbeck–Boussinesq approximations as:

Continuity equation:

$$\frac{\partial u}{\partial x} + \frac{\partial v}{\partial y} = 0, \quad (4.1)$$

Momentum equation:

$$\begin{aligned} \frac{\partial u}{\partial t} + u \frac{\partial u}{\partial x} + v \frac{\partial u}{\partial y} &= \frac{\partial U_e}{\partial t} + U_e \frac{\partial U_e}{\partial x} + \nu \frac{\partial^2 u}{\partial y^2} \left[\beta^* + (1 - \beta^*) \left(1 - \Gamma \frac{\partial u}{\partial y} \right)^{-1} \right] \\ &- \frac{\sigma B^2(t)}{\rho} (u - U_e) + \nu \Gamma \left(\frac{\partial u}{\partial y} \right) \left(\frac{\partial^2 u}{\partial y^2} \right) \left[(1 - \beta^*) \left(1 - \Gamma \frac{\partial u}{\partial y} \right)^{-2} \right], \end{aligned} \quad (4.2)$$

Energy equation:

$$\frac{\partial T}{\partial t} + u \frac{\partial T}{\partial x} + v \frac{\partial T}{\partial y} = \alpha \frac{\partial^2 T}{\partial y^2} + \tau \left[D_B \frac{\partial C}{\partial y} \frac{\partial T}{\partial y} + \frac{D_T}{T_\infty} \left(\frac{\partial T}{\partial y} \right)^2 \right], \quad (4.3)$$

Nanoparticles concentration equation:

$$\frac{\partial C}{\partial t} + u \frac{\partial C}{\partial x} + v \frac{\partial C}{\partial y} = D_B \frac{\partial^2 C}{\partial y^2} + \frac{D_T}{T_\infty} \frac{\partial^2 T}{\partial y^2}, \quad (4.4)$$

with physical boundary conditions

$$\left. \begin{aligned} u = U_w = \lambda U_e, \quad v = 0, \\ -k \frac{\partial T}{\partial y} = h_f (T_f - T), \quad C = C_w(x, t) \end{aligned} \right\} \text{ at } y = 0, \quad (4.5)$$

$$u \rightarrow U_e, \quad T \rightarrow T_\infty, \quad C \rightarrow C_\infty \} \text{ as } y \rightarrow \infty,$$

where D_B , D_T denote the Brownian and thermophoresis diffusion coefficients, respectively.

Further, the surface concentration $C_w(x, t)$ is defined as:

$$C_w(x, t) = C_\infty + \frac{C_0 U_w x}{\nu(1 - ct)^{\frac{1}{2}}}, \quad (4.6)$$

where C_0 depicts the initial reference concentration.

To proceed with the analysis, the following pertinent non-dimensional quantities are employed to recast the ordinary differential equations:

$$\eta = y \sqrt{\frac{(m+1)U_e}{2\nu x}}, \quad \psi(x, y, t) = \sqrt{\frac{2\nu x U_e}{m+1}} f(\eta), \quad \theta(\eta) = \frac{T - T_\infty}{T_f - T_\infty}, \quad \phi(\eta) = \frac{C - C_\infty}{C_w - C_\infty}, \quad (4.7)$$

where $\phi(\eta)$ is the dimensionless fluid concentration.

Using Eq. (4.7) into Eqs. (4.2) – (4.4), we get

$$\begin{aligned} & \left[\beta^* + (1 - \beta^*)(1 - We f'')^{-2} \right] f''' + f f'' + \beta \{1 - (f')^2\} \\ & - A(2 - \beta) \left\{ f' + \frac{\eta}{2} f'' - 1 \right\} - M^2(2 - \beta) \{f' - 1\} = 0, \end{aligned} \quad (4.8)$$

$$\theta'' + \text{Pr} (f\theta' - 2f'\theta) - \text{Pr} \frac{A}{2}(2 - \beta) (\eta\theta' + 3\theta) + \text{Pr} Nb\theta'\phi' + \text{Pr} Nt (\theta')^2 = 0, \quad (4.9)$$

$$\phi'' + \text{Pr} Le (f\phi' - 2f'\phi) - \text{Pr} \frac{A}{2}(2 - \beta) (\eta\phi' + 3\phi) \frac{Nt}{Nb} \theta'' = 0. \quad (4.10)$$

The associated converted boundary conditions for the flow take the form:

$$\left. \begin{aligned} f = 0, \quad f' = \lambda, \quad \phi = 1, \\ \theta' = -\gamma(2 - \beta)^{1/2} (1 - \theta), \end{aligned} \right\} \text{ at } \eta = 0, \quad (4.11)$$

$$f' \rightarrow 1, \quad \theta \rightarrow 0, \quad \phi \rightarrow 0 \quad \text{as } \eta \rightarrow \infty, \quad (4.12)$$

where $\lambda = \frac{U_w}{U_e}$ is the velocity ratio parameter, $M^2 = \frac{\rho B_0^2}{\rho a x^{m-1}}$ depicts the magnetic parameter, $Nt = \frac{\tau D_T (T_f - T_\infty)}{\nu T_\infty}$ indicates the thermophoresis number, $Nb = \frac{\tau D_B (C_w - C_\infty)}{\nu}$ associates the Brownian motion number, $Le = \frac{\alpha}{D_B}$ the Lewis number and $\gamma = \frac{h_f}{k} x \text{Re}^{-1/2}$ is the generalized Biot number.

4.1.1 Engineering coefficients

The practical coefficients of engineering concern in material processing operations are the C_{fx} , Nu_x and Sh_x which have the following respective definitions:

$$C_{fx} = \frac{\tau_w}{\rho U_e^2}, \quad Nu_x = \frac{x q_w}{k(T_f - T_\infty)}, \quad Sh_x = \frac{x q_m}{D_B(C_w - C_\infty)}, \quad (4.13)$$

with

$$\begin{aligned}\tau_w &= \mu_0 \frac{\partial u}{\partial y} \left[\beta^* + (1 - \beta^*) \left(1 - \Gamma \frac{\partial u}{\partial y} \right)^{-1} \right], & q_w &= -k \left(\frac{\partial T}{\partial y} \right) \Big|_{y=0}, \\ q_m &= -D_B \left(\frac{\partial C}{\partial y} \right) \Big|_{y=0}.\end{aligned}\quad (4.14)$$

Utilizing Eqs. (4.7) and (4.14), we obtain

$$\begin{aligned}(2 - \beta)^{1/2} \text{Re}^{1/2} C_{fx} &= f''(0) [\beta^* + (1 - \beta^*) \{1 - We f''(0)\}^{-1}], \\ (2 - \beta)^{1/2} \text{Re}^{-1/2} Nu_x &= -\theta'(0), & (2 - \beta)^{1/2} \text{Re}^{-1/2} Sh_x &= -\phi'(0).\end{aligned}\quad (4.15)$$

4.2 Numerical Simulations

In this study, RK-Fehlberg algorithm is employed to discretize the flow, energy and concentration equations for the considered problem with the assistance of shooting technique. In this regard, the Eqs. (4.8) – (4.12) are integrated for influential parameters. To do this, we first define the new variables:

$$f = X_1, \quad f' = X_2, \quad f'' = X_3, \quad \theta = X_4, \quad \theta' = X_5, \quad \phi = X_6, \quad \phi' = X_7. \quad (4.16)$$

By practising the above variables, system of first order differential equations become

$$\left. \begin{aligned}X_1' &= X_2, \\ X_2' &= X_3, \\ X_3' &= \frac{-X_1 X_3 - \beta \{1 - X_2^2\} - A(2 - \beta) \{X_2 + \frac{\eta}{2} X_3 - 1\} - M^2(2 - \beta) \{X_2 - 1\}}{[\beta^* + (1 - \beta^*) (1 - We X_3^2)^{-2}]},\end{aligned} \right\} \quad (4.17)$$

$$\left. \begin{aligned} X_4' &= X_5, \\ X_5' &= -\text{Pr} \left[X_1 X_5 - 2X_1 X_4 - \frac{A}{2}(2 - \beta)(\eta X_5 + 3X_4) + NbX_5 X_7 + NtX_5^2 \right], \end{aligned} \right\} \quad (4.18)$$

$$\left. \begin{aligned} X_6' &= X_7, \\ X_7' &= -\text{Pr} Le \left[X_1 X_7 - 2X_2 X_6 - \frac{A}{2}(2 - \beta)(\eta X_7 + 3X_6) \right] - \frac{Nt}{Nb} X_5'. \end{aligned} \right\} \quad (4.19)$$

Subsequently, the corresponding initial condition becomes:

$$\left. \begin{aligned} X_1(0) = 0, \quad X_2(0) = \lambda, \quad X_5(0) = -\gamma(2 - \beta)^{1/2} \{1 - X_4(0)\}, \quad X_6(0) = 1, \\ X_2(\infty) = 1, \quad X_4(\infty) = 0, \quad X_6(\infty) = 0. \end{aligned} \right\} \quad (4.20)$$

To set the solution of Eqs. (4.17) to (4.19) along with conditions (4.20) as an initial value problem, one requires the values of $f''(0)$, $\theta'(0)$ and $\phi'(0)$. Since, these are unknown in the current problem, so we start with the initial guesses for $f''(0)$, $\theta'(0)$ and $\phi'(0)$ such that the conditions $f' = 1$, $\theta = 0$ and $\phi = 0$ are satisfied for suitable finite domain length η_∞ . The above process is repeated until the desired accuracy is achieved. The far field BCs in Eq. (4.20) are estimated by utilizing a finite value 10 for η_∞ as follows:

$$f'(\eta_\infty) \rightarrow 1, \quad \theta(\eta_\infty) \rightarrow 0, \quad \phi(\eta_\infty) \rightarrow 0. \quad (4.21)$$

4.2.1 Code Validation

In order to ascertain either the obtained numerical results are accurate or not, it is necessary to check the behavior of velocity, nanofluid temperature and concentration fields. These profiles must fulfill the resultant boundary conditions at η_∞ asymptotically. We repeat the process by guessing values of $f''(0)$, $\theta'(0)$ and $\phi'(0)$ for the fixed pertinent parameters so that the

corresponding far field conditions (4.20) must be fulfilled. In addition, numerical results of $-f''(0)$ obtained in this analysis are validated by comparing them with those calculated by Rajgopal *et al.* [84], Kuo [101] and Ishaq *et al.* [102] in some special case when $\beta^* = 0 = We = \lambda$. This comparison is depicted quantitatively through **Table 4.1** which verifies the accuracy of our result.

4.3 Numerical Result and Discussion

Numerical results of this investigation are declared in terms of the velocity, temperature and concentration distributions of various pertinent parameters; these physical parameters include We , Pr , A , β , λ , M , Le , Nt , Nb and γ . The impact of these emerging parameters on flow field, skin friction, rate of heat and mass transfer coefficients in terms of Nusselt number and Sherwood number are plotted through **Figs. 4.2 – 4.10**. In order to perform the numerical simulation we have assigned fixed values to non-dimensional pertinent parameter as $We = M = 1$, $\lambda = \beta = 0.2$, $\beta^* = 0.2$, $Pr = 0.72$, $Nt = \gamma = 0.1$, and $Nb = 0.2$. In the whole analysis, these values are kept as constant except the varied parameters as shown in the respective figure legends. Following the work of Turkyilmazoglu [33], numerical simulation is completed by reporting a certain range of required parameters $A(0.0 \leq A \leq 1.2)$, $M(0 \leq M \leq 3.0)$, $We(1.0 \leq We \leq 4.0)$, $\beta^*(0 \leq \beta^* \leq 1.0)$, $Nt(0.1 \leq Nt \leq 2.5)$, $Nb(0.1 \leq Nb \leq 0.4)$, $\gamma(0.1 \leq \gamma \leq 0.4)$ and $Le(1 \leq Le \leq 4)$.

The variations of $f'(\eta)$, $\theta(\eta)$ and $\phi(\eta)$ for different A are exhibited through **Figs. 4.2(a) – 4.2(c)**. It is anticipated by **Fig.4.2(a)** that the velocity of nanofluid demonstrates an accelerating behavior near the solid boundary for higher values of A while an reverse behavior is

seen as we move along η within the boundary layer regime. It can be noticed that all the graphs are captured for static wedge ($\lambda = 0$) and moving wedge ($\lambda = 0.3$). We further noticed that both the velocity and momentum boundary layer thickness are higher in case of moving wedge. Further, we see that the nanofluid temperature is found to reduce with increasing A , whereas the thermal boundary layer becomes thinner, as illustrated in **Fig. 4.2(b)**. It is due to the fact that that when unsteadiness parameter increases then the sheet loses its heat and the nanofluids temperature decreases. Moreover, the concentration profile $\phi(\eta)$ is demonstrated in **Fig. 4.2(c)**. It is evident from this figure that both the nanoparticles concentration and solutal boundary layer thickness reduce with growing values of A .

Impact of M on momentum, thermal and concentration boundary layers is demonstrated in **Figs. 4.3(a) – 4.3(c)** for the case of flow over a static and moving wedge. Physically, $M = 0$ depicts hydrodynamic flow and $M > 0$ stands for hydromagnetic flow. We clearly see from **Fig. 4.3(a)** that the fluid velocity at any point in the flow field enhances due to increasing M . It is additionally observed that the M creates drag force which tends to deliver resistance in the flow of fluid particles and the momentum boundary layer tends toward the surface, as seen in **Fig. 4.3(a)**. It is analyzed from these profiles that the velocity boundary layer thickness diminishes for higher M in both cases. In view of physics, the Lorentz force generated by the dual actions of electric and magnetic fields lessens the momentum boundary layer thickness by resisting the transport phenomenon. **Fig.4.3(b)** and **4.3(c)** display the impact of M on $\theta(\eta)$ and $\phi(\eta)$ distributions, respectively. Note that for both temperature and concentration profiles either $\lambda = 0$ or $\lambda = 0.3$, we observed a decreasing trend. Furthermore, the thermal boundary layer seems to decrease for increasing magnetic parameter.

Figs. 4.4(a) – 4.4(c) are drawn to look into the behavior of We on $f'(\eta)$, $\theta(\eta)$ and $\phi(\eta)$.

It is seen through **Fig. 4.4(a)** that the profile of velocity is boosted by enlarging We in case of both static and moving wedge. It is worthwhile to noticed that momentum boundary layer thickness depreciates for higher estimation of We . Also, this figure indicates that for $\lambda = 0.3$, a thicker velocity boundary layer is produced than that of $\lambda = 0$. Furthermore, it is noted from **Fig. 4.4(b)** and **4.4(c)** that the nanofluid temperature and concentration distributions are decreasing function of We . Increasing the Weissenberg number has a shrinking effect on the thickness for thermal and concentration boundary layers.

To visualize the behavior of β^* on $f'(\eta)$ and $\theta(\eta)$, we have plotted **Figs. 4.5(a)** and **4.5(b)**, respectively. These profiles are illustrated for two distinct values of wedge angle parameter, i.e., $\beta = 0$ (flow over a horizontal flat plate) and $\beta = 1$ (flow over a vertical flat plate). We noticed a considerable difference between these two cases for distinct viscosity ratio parameter. From **Fig. 4.5(a)**, it can be concluded that at each point inside the boundary layer regime the velocity of nanofluids accelerates by uplifting values of β^* . However, an opposite pattern is seen for momentum boundary layer thickness in both cases. Furthermore, all the velocity curves satisfy the far field boundary conditions asymptotically. **Fig. 4.5(b)** is sketched to see the profiles of nanoparticles temperature for varied values of β^* by keeping all other involve parameters fixed. An increment in the viscosity ratio parameter causes a significant reduction in the nanofluids temperature in both cases. Additionally, it is important to note that the nanofluids temperature is higher in case of $\beta = 0$ when compare to the case of $\beta = 1$.

The thermophoresis parameter Nt has a vital role on $\theta(\eta)$ and $\phi(\eta)$ in the boundary layer region. The influence of Nt on $\theta(\eta)$ and $\phi(\eta)$ is captured in **Figs. 4.6(a)** and **4.6(b)**. As demonstrated in these figures, the temperature and concentration at each point within the boundary layer reveal the same increasing behavior with an increment of thermophoresis parameter Nt .

From a physical perspective, thermophoresis is a force in which these small particles employ a physical force on another particles to move it away from the hotter surface and pushed toward a colder one. Therefore, the rising values of Nt corresponds to higher thermophoretic force which tends to push the nanoparticles in the boundary layer from higher temperature to a lower temperature region. As a consequence, a rise in the nanofluid temperature and nanoparticles concentration is noted. Moreover, the thermal and concentration boundary layer thicknesses are larger for slightly augmented values of Nt .

A qualitative analysis of the thermal and concentration boundary layers with Brownian motion parameter Nb is delineated in **Figs. 4.7(a)** and **4.7(b)**, respectively. One can clearly view from **Fig. 4.7(a)** that the nanofluid temperature escalates when Nb enhances. Indeed, the Brownian motion is the result of crisscross motion of nanoparticles. Physically, an enhancement in Brownian motion leads to the effective gesture of nanoparticles inside the flow regime. Therefore, the strength of this chaotic movement increase the kinematic energy of the nanoparticles which accelerates the nanofluid's temperature. Moreover, an enlargement in Nb boosts the unsystematic motion of the particles and accordingly the thermal boundary layer thickness grows. However, it is depicted that concentration profile shows a declining trend with growing Nb . Further, it is noticed that $\phi(\eta)$ decreases significantly with increase in Nb .

Fig. 4.8 revealed the behavior of $\theta(\eta)$ and $\phi(\eta)$ for various γ . As expected, the Biot number enhances the temperature distribution. Moreover, the thermal boundary layer thickness depicts a growing behavior as the value of γ is raised. The wedge surface is isolated at $\gamma = 0$.

To illustrate the influence of Le on $\phi(\eta)$, **Fig. 4.9** is displayed. It is found that the Le considerably effects the nanoparticles concentration field. From this figure, it is established that the nanoparticles concentration reduces by growing Le . The reason behind this is because of

the reduction in mass diffusivity or due to the Brownian motion of nanoparticles.

Figs. 4.10(a) – 4.10(c), respectively, show the influence of $\text{Re}^{1/2} C_{fx}$, $\text{Re}^{-1/2} Nu_x$ and $\text{Re}^{-1/2} Sh_x$ for two cases flow over flat plate and near the stagnation point, respectively. From **Fig. 4.10(a)**, we can see that the local skin friction enhances with an increment in the unsteadiness parameter for both the cases. It can also be seen that the local skin friction is higher for stagnation point flow in comparison with the flow over a flat plate. In **Fig. 4.10(b)**, the non-dimensional Nusselt number is plotted against Prandtl number by varying the generalized Biot number. This plot shows that the rate of heat transfer increases in response to a rise in Biot number for both the cases. The variation of local Sherwood number with respect to Lewis number is sketched in **Fig. 4.10(c)**. The behavior of mass transfer coefficient in **Fig. 4.10(c)** illustrates that concentration gradient augments for Le . In case of stagnation point flow, the mass transfer is higher for particular values of Lewis number.

Table 4.2 incorporates the data showing the behavior of numerical results of local skin frictions under the influence of β , λ , We and β^* . Based on this table, it is seen that the $\text{Re}^{1/2} C_{fx}$ upgrades by improving the estimations of A and M . Enhancement in β and λ reduce the surface drag force. Further, the viscosity ratio parameter has decreasing effect on $\text{Re}^{1/2} C_{fx}$. **Table 4.3** illustrates the impact of A , β and Pr on rate of heat and mass transfer when $M = We = 2.0$, $\gamma = 0.1$, $\lambda = 0.2$, $Le = 1.0$, $\beta^* = 0.2$ and $Nt = Nb = 0.2$ are fixed. As evident through **Table 4.3** that increase in A and β causes a decrease in the local Nusselt number while an opposite is true for higher Prandtl number. Furthermore, a foremost factor is that Sherwood number is the decreasing function of β and an increasing function of A and Pr .

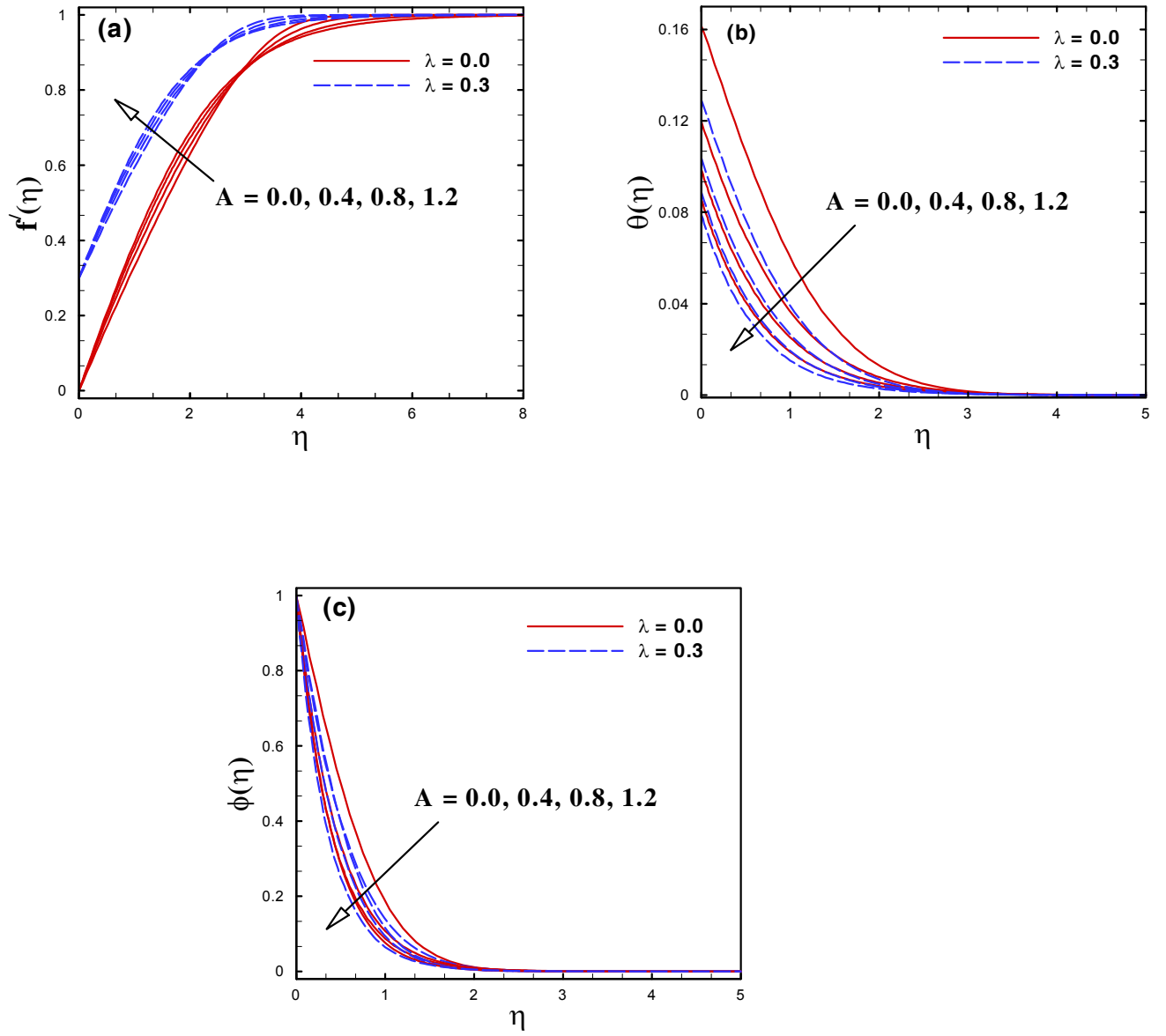


Fig. 4.2: Impact of A on $f'(\eta)$, $\theta(\eta)$ and $\phi(\eta)$.

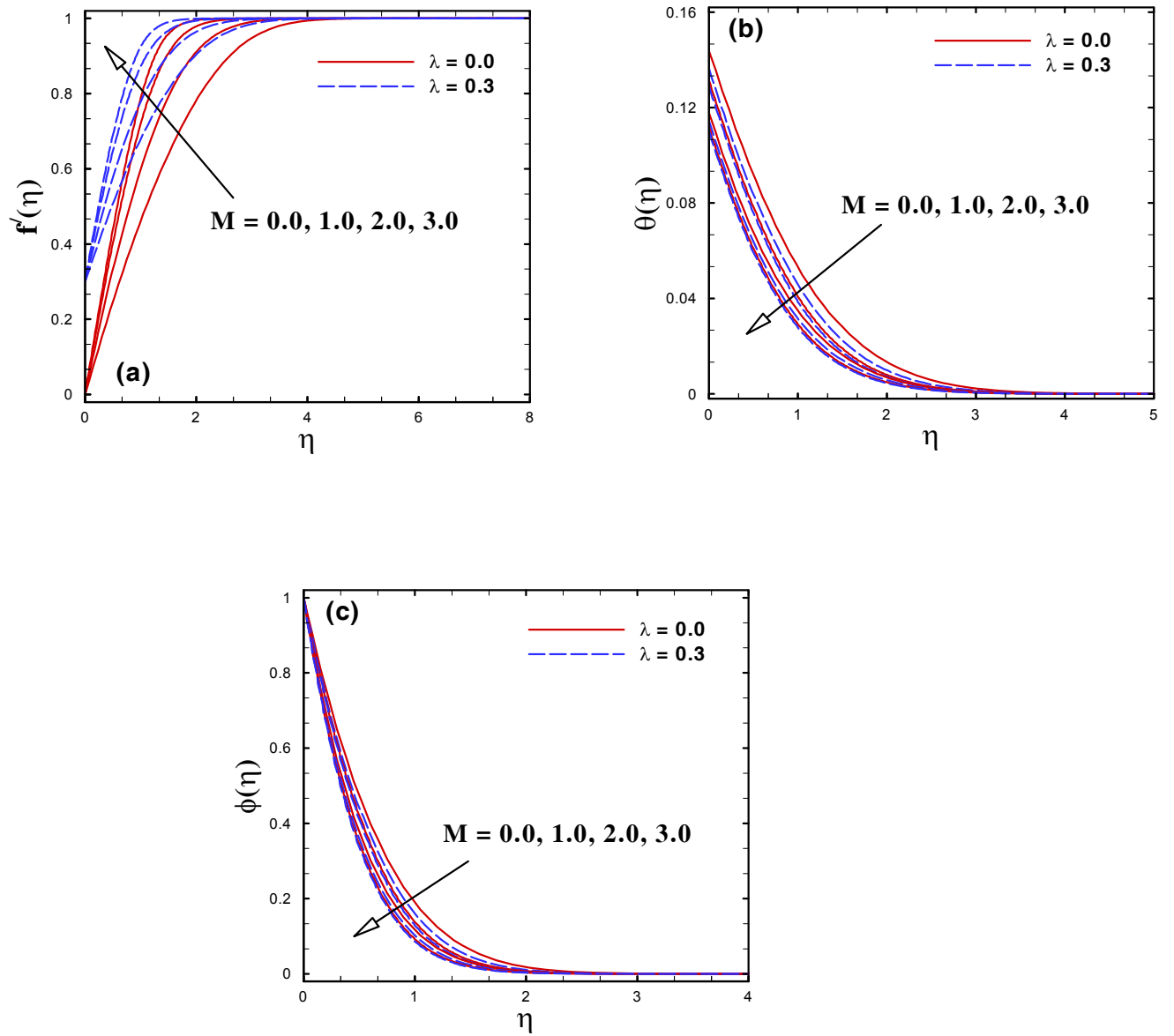


Fig. 4.3: Impact of M on $f'(\eta)$, $\theta(\eta)$ and $\phi(\eta)$.

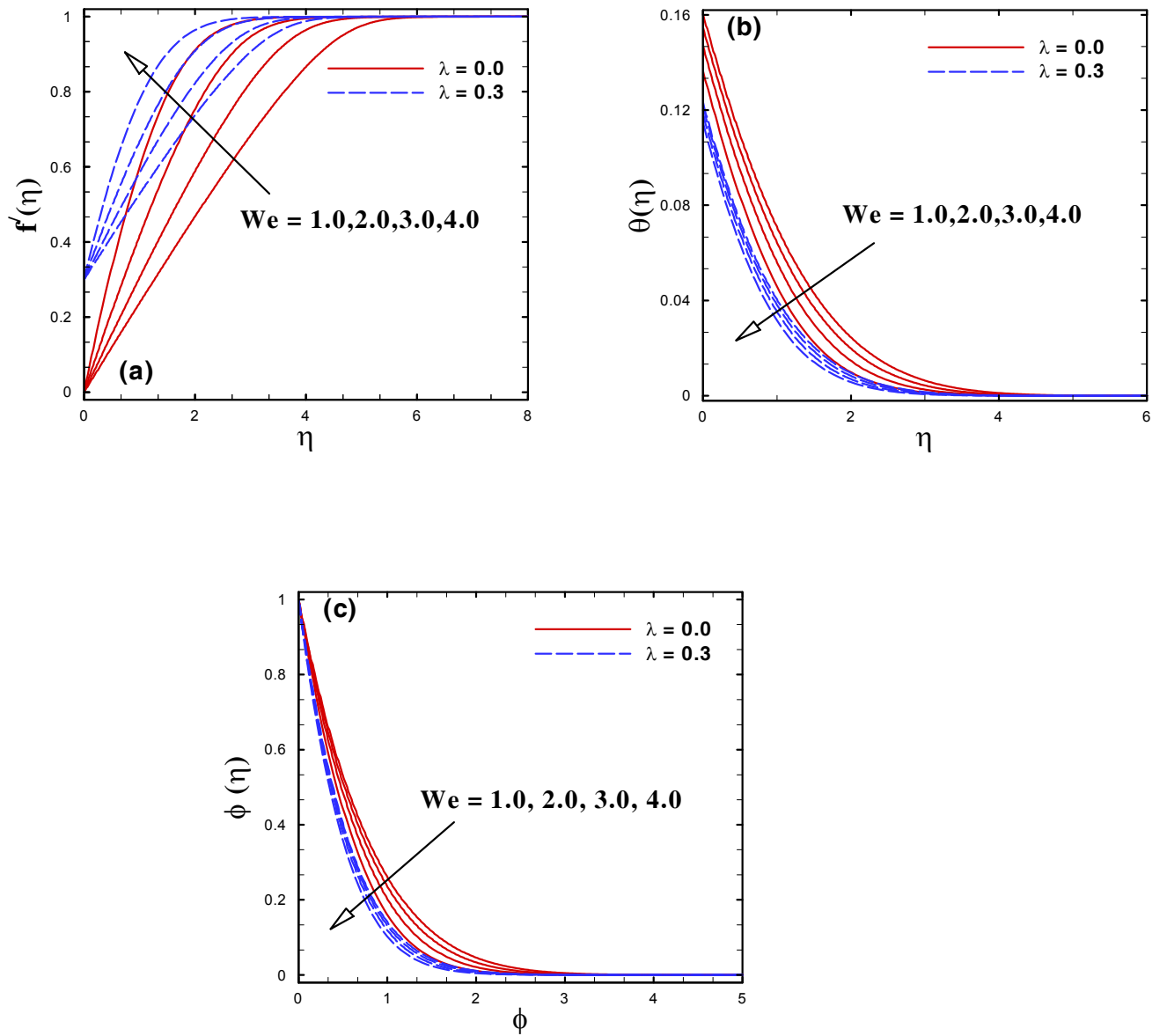


Fig. 4.4: Impact of We on $f'(\eta)$, $\theta(\eta)$ and $\phi(\eta)$.

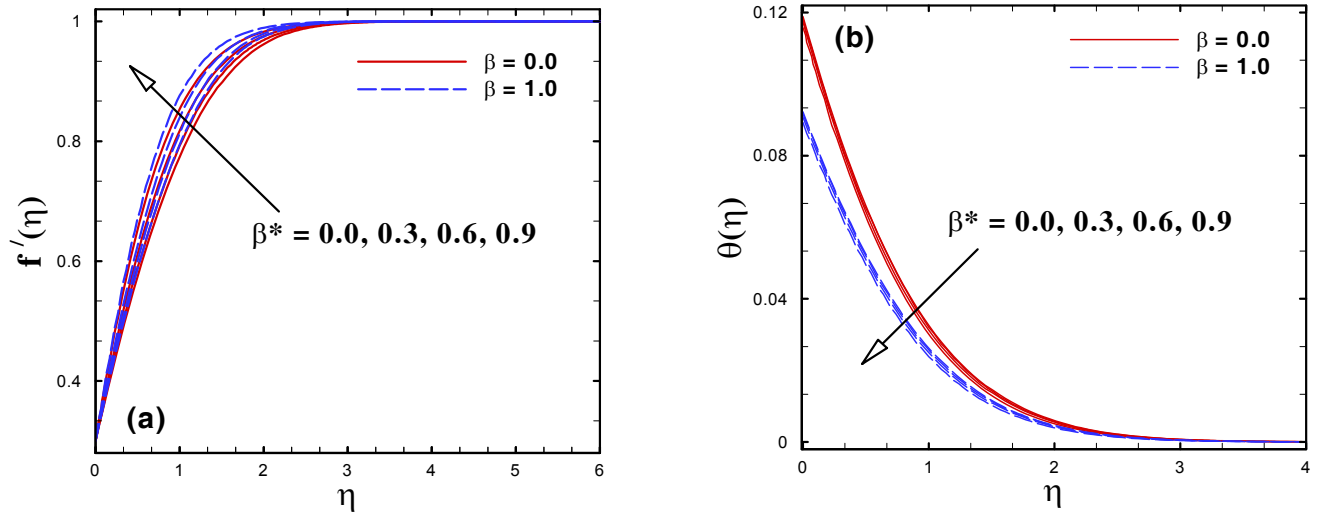


Fig. 4.5: Impact of β^* on $f'(\eta)$ and $\theta(\eta)$.

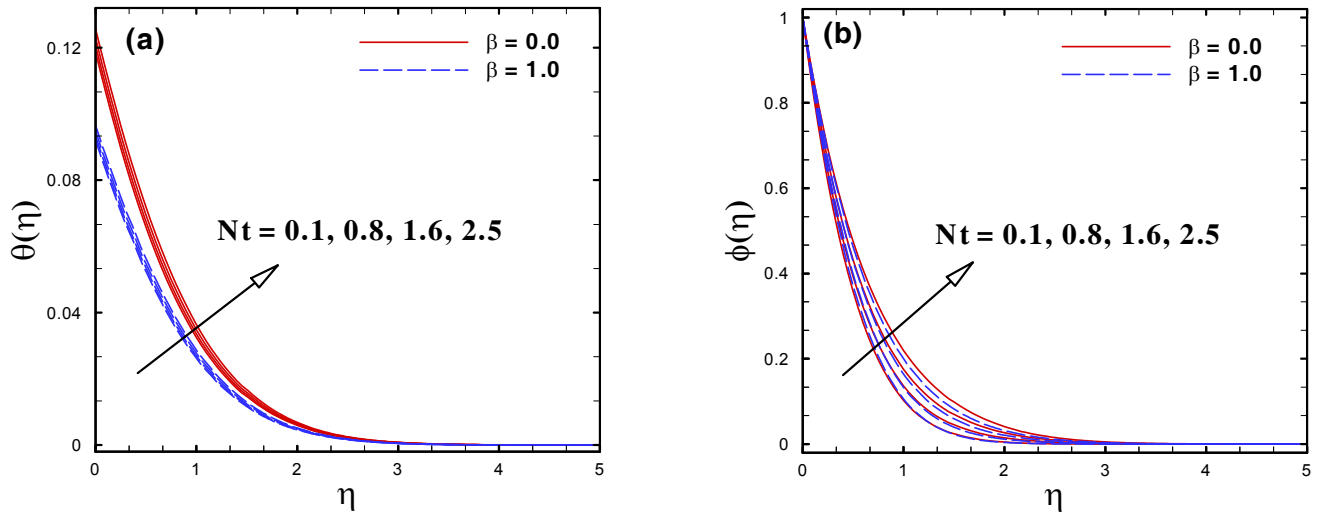


Fig. 4.6: Impact of Nt on $\theta(\eta)$ and $\phi(\eta)$.

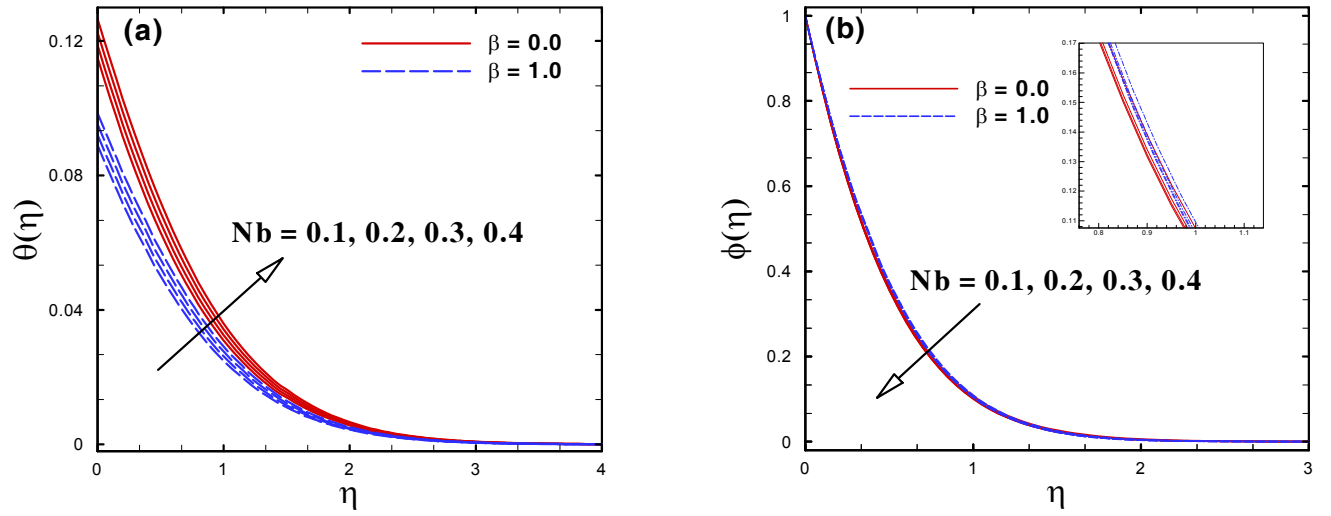


Fig. 4.7: Impact of Nb on $\theta(\eta)$ and $\phi(\eta)$.

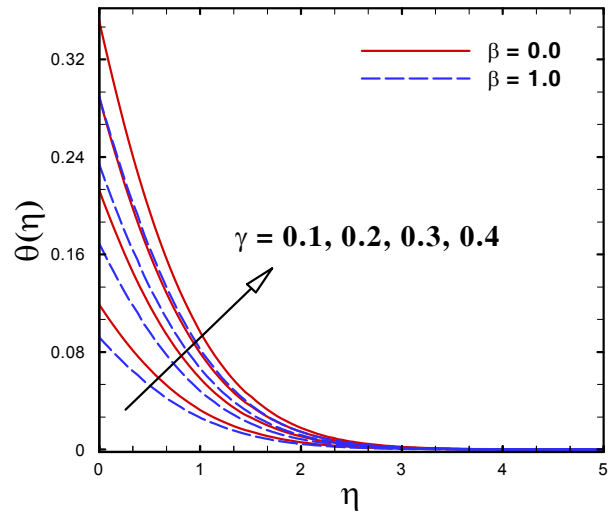


Fig. 4.8: Impacts of γ on $\theta(\eta)$.

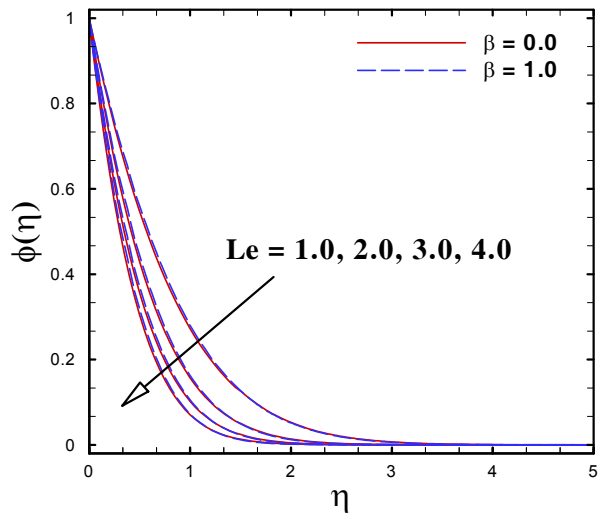


Fig. 4.9: Impact of Le on $\phi(\eta)$.

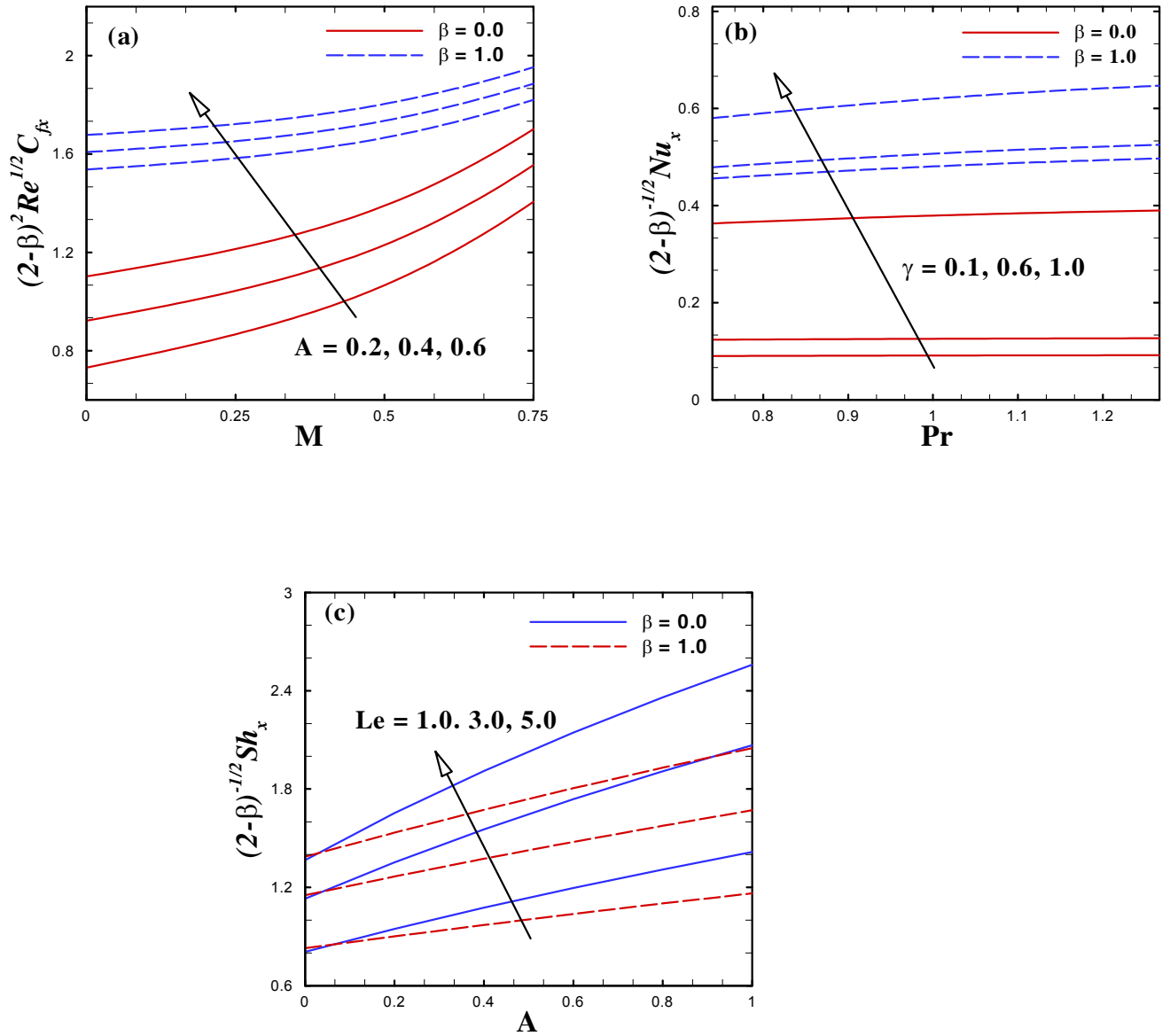


Fig. 4.10: Variation of $\text{Re}^{1/2} C_{fx}$, $\text{Re}^{-1/2} \text{Nu}_x$ and $\text{Re}^{-1/2} \text{Sh}_x$ for varying A , γ and Le .

Table 4.1 : A comparison of $-f''(0)$ for varying β when $\beta^* = We = \lambda = A = 0$.

β	Rajagopal <i>et al.</i> [84]	Kuo [101]	Ishaq <i>et al.</i> [102]	Present study
0.0	—	0.469600	0.4696	0.469600
0.1	0.587035	0.587080	0.5870	0.587035
0.3	0.774755	0.774724	0.7748	0.774755
0.5	0.927680	0.927905	0.9277	0.927680
1.0	1.232585	1.232589	1.2326	1.232588

Table 4.2 : The numerical data of $Re^{1/2}C_{fx}$ for various values of β , λ , We and β^* when $A = 0.2$ and $M = 2.0$.

β	λ	We	β^*	$(2 - \beta)^{1/2} Re^{1/2}C_{fx}$
0.0	0.2	2.0	0.3	6.83663
0.3	—	—	—	6.28601
0.6	—	—	—	5.73011
1.0	—	—	—	4.98722
0.3	-0.2	—	—	12.4367
—	-0.1	—	—	10.7264
—	0.1	—	—	7.64492
—	0.2	—	—	6.28601
—	—	2.0	—	6.28601
—	—	2.5	—	7.42285
—	—	3.0	—	8.58178
—	—	3.5	—	9.76077
—	—	2.0	0.2	6.14577
—	—	—	0.4	5.98778
—	—	—	0.6	5.80668
—	—	—	0.8	5.58524

Table 4.3 : The numerical data of $Re^{-1/2}Nu_x$ and $Re^{-1/2}Sh_x$ for A , β and Pr when $M = We = 2.0$, $\gamma = 0.1$, $\lambda = 0.2$, $Le = 1.0$, $\beta^* = 0.2$ and $Nt = Nb = 0.2$.

A	β	Pr	$(2 - \beta)^{1/2} Re^{-1/2}Nu_x$	$(2 - \beta)^{1/2} Re^{-1/2}Sh_x$
0.0	0.3	3.0	0.117747	1.53830
0.2	–	–	0.120004	1.85559
0.3	–	–	0.120774	2.00184
–	0.0	–	0.130585	2.07381
–	0.4	–	0.117310	1.97738
–	1.0	–	0.093656	1.82524
–	–	1.0	0.0913386	1.10523
–	–	2.0	0.092991	1.51457
–	–	3.0	0.093656	1.82524

Chapter 5

Axisymmetric Flow of Williamson Nanofluid with Slip Mechanism

In this chapter, we present a novel study to develop a mathematical model for a non-Newtonian Williamson fluid flow subject to nanoparticles. The movement of nanoparticle is caused by a radially stretching surface. This study aims at describing the thermal characteristics of nanoparticles via Rosseland approximation to illustrate the non-linear radiation effects. Convective heat transfer model alongside Brownian motion are studied for the electrically conducting nanofluids flow. A set of PDEs for Williamson nanofluids flow are derived by basic conservation laws, i.e., momentum, energy and concentration. These equations are initially converted to ODEs by employing non-dimensional quantities. The numerical simulation of these equations is performed using the Runge-Kutta Fehlberg scheme. An examination is done to investigate the impact of pertinent parameters on momentum, thermal and concentration boundary layers. It is concluded from our computations that the nanofluids velocity and temperature accelerate when Brownian motion parameter rises. Finally, a comparison of obtained nu-

merical solution against previous literature is presented which shows satisfactory agreement.

5.1 Flow Equations

Mathematical model elaborating the characteristics of unsteady Williamson fluid can be expressed in terms of basic governing expressions. Considering the fluid to be incompressible, the flow equations are

$$\nabla \cdot \mathbf{V} = 0, \quad (5.1)$$

$$\rho \frac{d\mathbf{V}}{dt} = -\nabla p + \nabla \cdot \boldsymbol{\tau} + \mathbf{J} \times \mathbf{B}. \quad (5.2)$$

Here, \mathbf{J} and \mathbf{B} represent the electrical current density and magnetic field, respectively. The shear stress can be expressed in terms of non-Newtonian viscosity $\mu(\dot{\gamma})$ as

$$\boldsymbol{\tau} = \mu(\dot{\gamma})\mathbf{D}. \quad (5.3)$$

The constitutive equation for Williamson fluid are given by Eqs. (2.4) to (2.7) (cf. Chapter 2).

The velocity field for described model is taken as:

$$\mathbf{V} = [u(r, z, t), 0, w(r, z, t)], \quad (5.4)$$

where (u, w) are the components of velocity along the radial and axial directions, respectively.

The shear rate according to the Williamson model is defined in terms of the velocity gradients

as:

$$\dot{\gamma} = \left[2 \left(\frac{\partial u}{\partial r} \right)^2 + 2 \left(\frac{\partial w}{\partial z} \right)^2 + \left(\frac{\partial u}{\partial z} + \frac{\partial w}{\partial r} \right)^2 + \frac{2u^2}{r^2} \right]^{1/2}. \quad (5.5)$$

Under the overhead norms, the equations which governs the flow become

$$\frac{\partial u}{\partial r} + \frac{u}{r} + \frac{\partial w}{\partial z} = 0, \quad (5.6)$$

$$\rho \left(\frac{\partial u}{\partial t} + u \frac{\partial u}{\partial r} + w \frac{\partial u}{\partial z} \right) = -\frac{\partial p}{\partial r} + \frac{\partial \tau_{rr}}{\partial r} + \frac{\partial \tau_{rz}}{\partial z} + \frac{\tau_{rr} - \tau_{\theta\theta}}{r}, \quad (5.7)$$

$$\rho \left(\frac{\partial w}{\partial t} + u \frac{\partial w}{\partial r} + w \frac{\partial w}{\partial z} \right) = -\frac{\partial p}{\partial z} + \frac{1}{r} \frac{\partial}{\partial r} (r \tau_{rz}) + \frac{\partial \tau_{zz}}{\partial z}, \quad (5.8)$$

where

$$\tau_{rr} = 2\mu_0 \frac{\partial u}{\partial r} \left[\beta^* + (1 - \beta^*) \left(1 - \Gamma \left\{ \begin{array}{l} 2 \left(\frac{\partial u}{\partial r} \right)^2 + 2 \left(\frac{\partial w}{\partial z} \right)^2 \\ + \left(\frac{\partial u}{\partial z} + \frac{\partial w}{\partial r} \right)^2 + \frac{2u^2}{r^2} \end{array} \right\}^{1/2} \right)^{-1} \right], \quad (5.9)$$

$$\tau_{\theta\theta} = 2\mu_0 \frac{u}{r} \left[\beta^* + (1 - \beta^*) \left(1 - \Gamma \left\{ \begin{array}{l} 2 \left(\frac{\partial u}{\partial r} \right)^2 + 2 \left(\frac{\partial w}{\partial z} \right)^2 \\ + \left(\frac{\partial u}{\partial z} + \frac{\partial w}{\partial r} \right)^2 + \frac{2u^2}{r^2} \end{array} \right\}^{1/2} \right)^{-1} \right], \quad (5.10)$$

$$\tau_{zz} = 2\mu_0 \frac{\partial w}{\partial z} \left[\beta^* + (1 - \beta^*) \left(1 - \Gamma \left\{ \begin{array}{l} 2 \left(\frac{\partial u}{\partial r} \right)^2 + 2 \left(\frac{\partial w}{\partial z} \right)^2 \\ + \left(\frac{\partial u}{\partial z} + \frac{\partial w}{\partial r} \right)^2 + \frac{2u^2}{r^2} \end{array} \right\}^{1/2} \right)^{-1} \right], \quad (5.11)$$

$$\tau_{rz} = \mu_0 \left(\frac{\partial u}{\partial z} + \frac{\partial w}{\partial r} \right) \left[\beta^* + (1 - \beta^*) \left(1 - \Gamma \left\{ \begin{array}{l} 2 \left(\frac{\partial u}{\partial r} \right)^2 + 2 \left(\frac{\partial w}{\partial z} \right)^2 \\ + \left(\frac{\partial u}{\partial z} + \frac{\partial w}{\partial r} \right)^2 + \frac{2u^2}{r^2} \end{array} \right\}^{1/2} \right)^{-1} \right]. \quad (5.12)$$

Invoking τ_{rr} , $\tau_{\theta\theta}$, τ_{zz} and τ_{rz} from above the equations, the governing momentum Eqs. (5.7)

and (5.8) take the form:

$$\begin{aligned}
\rho \left(\frac{\partial u}{\partial t} + u \frac{\partial u}{\partial r} + w \frac{\partial u}{\partial z} \right) &= -\frac{\partial p}{\partial r} - \frac{\sigma B_0^2}{\rho} u + \mu_0 \left[\frac{\partial^2 u}{\partial r^2} + \frac{\partial^2 u}{\partial z^2} + \frac{\partial}{\partial r} \left(\frac{u}{r} \right) \right] \\
&\times \left[\beta^* + (1 - \beta^*) \left(1 - \Gamma \left\{ \begin{array}{l} 2 \left(\frac{\partial u}{\partial r} \right)^2 + 2 \left(\frac{\partial w}{\partial z} \right)^2 \\ + \left(\frac{\partial u}{\partial z} + \frac{\partial w}{\partial r} \right)^2 + \frac{2u^2}{r^2} \end{array} \right\}^{1/2} \right)^{-1} \right] \\
+ 2\mu_0 \frac{\partial u}{\partial r} \frac{\partial}{\partial r} &\left[\beta^* + (1 - \beta^*) \left(1 - \Gamma \left\{ \begin{array}{l} 2 \left(\frac{\partial u}{\partial r} \right)^2 + 2 \left(\frac{\partial w}{\partial z} \right)^2 \\ + \left(\frac{\partial u}{\partial z} + \frac{\partial w}{\partial r} \right)^2 + \frac{2u^2}{r^2} \end{array} \right\}^{1/2} \right)^{-1} \right] \\
&+ \mu_0 \left(\frac{\partial u}{\partial z} + \frac{\partial w}{\partial r} \right) \\
&\times \frac{\partial}{\partial z} \left[\beta^* + (1 - \beta^*) \left(1 - \Gamma \left\{ \begin{array}{l} 2 \left(\frac{\partial u}{\partial r} \right)^2 + 2 \left(\frac{\partial w}{\partial z} \right)^2 \\ + \left(\frac{\partial u}{\partial z} + \frac{\partial w}{\partial r} \right)^2 + \frac{2u^2}{r^2} \end{array} \right\}^{1/2} \right)^{-1} \right], \tag{5.13}
\end{aligned}$$

$$\begin{aligned}
& \rho \left(\frac{\partial w}{\partial t} + u \frac{\partial w}{\partial r} + w \frac{\partial w}{\partial z} \right) = -\frac{\partial p}{\partial z} + \mu_0 \left(\frac{\partial^2 w}{\partial r^2} + \frac{\partial^2 w}{\partial z^2} \right) \\
& \times \left[\beta^* + (1 - \beta^*) \left(1 - \Gamma \left\{ \begin{array}{l} 2 \left(\frac{\partial u}{\partial r} \right)^2 + 2 \left(\frac{\partial w}{\partial z} \right)^2 \\ + \left(\frac{\partial u}{\partial z} + \frac{\partial w}{\partial r} \right)^2 + \frac{2u^2}{r^2} \end{array} \right\}^{1/2} \right)^{-1} \right] \\
& + 2\mu_0 \frac{\partial w}{\partial z} \frac{\partial}{\partial z} \left[\beta^* + (1 - \beta^*) \left(1 - \Gamma \left\{ \begin{array}{l} 2 \left(\frac{\partial u}{\partial r} \right)^2 + 2 \left(\frac{\partial w}{\partial z} \right)^2 \\ + \left(\frac{\partial u}{\partial z} + \frac{\partial w}{\partial r} \right)^2 + \frac{2u^2}{r^2} \end{array} \right\}^{1/2} \right)^{-1} \right] \\
& + \mu_0 \left(\frac{\partial u}{\partial z} + \frac{\partial w}{\partial r} \right) \frac{\partial}{\partial r} \left[\beta^* + (1 - \beta^*) \left(1 - \Gamma \left\{ \begin{array}{l} 2 \left(\frac{\partial u}{\partial r} \right)^2 + 2 \left(\frac{\partial w}{\partial z} \right)^2 \\ + \left(\frac{\partial u}{\partial z} + \frac{\partial w}{\partial r} \right)^2 + \frac{2u^2}{r^2} \end{array} \right\}^{1/2} \right)^{-1} \right] \\
& + \frac{\mu_0}{r} \frac{\partial w}{\partial r} \left[\beta^* + (1 - \beta^*) \left(1 - \Gamma \left\{ \begin{array}{l} 2 \left(\frac{\partial u}{\partial r} \right)^2 + 2 \left(\frac{\partial w}{\partial z} \right)^2 \\ + \left(\frac{\partial u}{\partial z} + \frac{\partial w}{\partial r} \right)^2 + \frac{2u^2}{r^2} \end{array} \right\}^{1/2} \right)^{-1} \right], \quad (5.14)
\end{aligned}$$

Utilizing the well-known boundary-layer estimations [$O(u, r) = 1$, $O(v, z) = \delta$, $O(\nu) = \delta = O(\Gamma)$], the governing equations reduce to:

$$\begin{aligned}
\frac{\partial u}{\partial t} + u \frac{\partial u}{\partial r} + w \frac{\partial u}{\partial z} &= -\frac{\sigma B(t)^2}{\rho} u + \nu \frac{\partial^2 u}{\partial z^2} \left[\beta^* + (1 - \beta^*) \left(1 - \Gamma \frac{\partial u}{\partial z} \right)^{-1} \right] \\
&+ \nu \Gamma \left(\frac{\partial u}{\partial z} \right) \frac{\partial^2 u}{\partial z^2} \left[(1 - \beta^*) \left(1 - \Gamma \frac{\partial u}{\partial z} \right)^{-2} \right], \quad (5.15)
\end{aligned}$$

$$0 = -\frac{1}{\rho} \frac{\partial p}{\partial z}. \quad (5.16)$$

5.2 Flow Analysis

Let us formulate the unsteady axisymmetric Williamson nanofluid flow generated by a convectively heated radially stretching surface with non-linear thermal radiation effects. The flow

mechanism has been considered in two-dimensional (r, z) reference frames as exhibited in **Fig. 5.1**. The radially stretched surface coincide with the plane $(z = 0)$ and liquid flows in upper half region $(z > 0)$. Besides, the flow field is subject to an external magnetic field having strength $B(t) = \frac{B_0}{(1-\beta t)^{1/2}}$ applied along the z -axis. The induced magnetic field is absent for smaller magnetic Reynolds number. Also, heat transfer analysis of nanoparticles is studied by incorporating the impact of thermophoresis and Brownian motion. We suppose the velocity slip at the surface of the stretching sheet. The stretching velocity of the sheet in radial direction is given by $u_w(r, t) = \frac{ar}{1-ct}$.

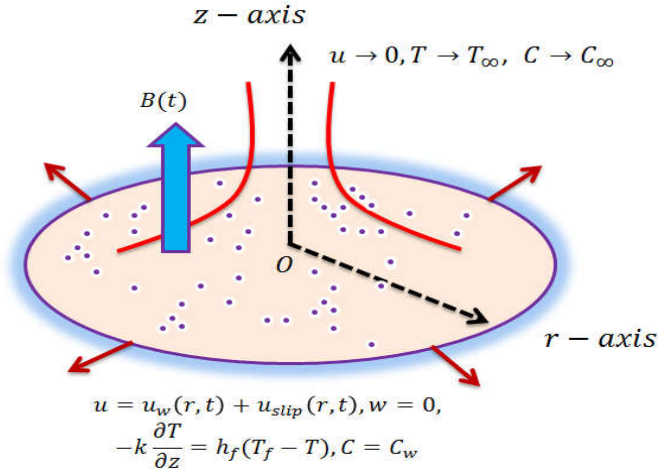


Fig. 5.1: A physical layout of the flow configuration.

The governing equations by assuming time-dependent magnetic field take the form:

$$\frac{\partial u}{\partial r} + \frac{u}{r} + \frac{\partial w}{\partial z} = 0, \quad (5.17)$$

$$\begin{aligned} \frac{\partial u}{\partial t} + u \frac{\partial u}{\partial r} + w \frac{\partial u}{\partial z} &= \nu \frac{\partial^2 u}{\partial z^2} \left[\beta^* + (1 - \beta^*) \left(1 - \Gamma \frac{\partial u}{\partial z} \right)^{-1} \right] - \frac{\sigma B^2(t)}{\rho} u \\ &+ \nu \Gamma \left(\frac{\partial u}{\partial z} \right) \frac{\partial^2 u}{\partial z^2} \left[(1 - \beta^*) \left(1 - \Gamma \frac{\partial u}{\partial z} \right)^{-2} \right], \end{aligned} \quad (5.18)$$

$$\frac{\partial T}{\partial t} + u \frac{\partial T}{\partial r} + w \frac{\partial T}{\partial z} = \frac{\partial}{\partial z} \left[\left(\alpha_m + \frac{16\sigma^* T^3}{3k^* \rho c_p} \right) \frac{\partial T}{\partial z} \right] + \tau \left[D_B \frac{\partial C}{\partial z} \frac{\partial T}{\partial z} + \frac{D_T}{T_\infty} \left(\frac{\partial T}{\partial z} \right)^2 \right], \quad (5.19)$$

$$\frac{\partial C}{\partial t} + u \frac{\partial C}{\partial r} + v \frac{\partial C}{\partial z} = D_B \frac{\partial^2 C}{\partial z^2} + \frac{D_T}{T_\infty} \frac{\partial^2 T}{\partial z^2}. \quad (5.20)$$

In the above equations, ρ represents the fluid density, $\tau = (\rho c_p)/(\rho c)_f$ the heat capacitance ratio of nanoparticle to base liquid and $\alpha_m = k/(\rho c)_p$ the thermal diffusivity.

The boundary conditions are reported below:

$$u = u_w(r, t) + u_{slip}, \quad w = 0, \quad k \frac{\partial T}{\partial z} = -h_f(T_f - T), \quad C = C_w \quad \text{at} \quad z = 0, \quad (5.21)$$

$$u \rightarrow 0, \quad T \rightarrow T_\infty, \quad C \rightarrow C_\infty \quad \text{as} \quad z \rightarrow \infty. \quad (5.22)$$

The mathematical form of velocity slip condition is:

$$u_{slip} = L_1 \tau_{rz} = L_1 \frac{\partial u}{\partial z} \left[\beta^* + (1 - \beta^*) \left(1 - \Gamma \frac{\partial u}{\partial z} \right)^{-1} \right], \quad (5.23)$$

where L_1 is known as slip length.

We consider the following non-dimensional variables [80]:

$$\eta = \frac{z}{r} \text{Re}^{1/2}, \quad \psi(r, z, t) = -r^2 u_w \text{Re}^{-1/2} f(\eta), \quad u = \frac{-1}{r} \frac{\partial \psi}{\partial z}, \quad w = \frac{1}{r} \frac{\partial \psi}{\partial r}, \quad (5.24)$$

$$\theta(\eta) = \frac{T - T_\infty}{T_f - T_\infty} \quad \text{and} \quad \phi(\eta) = \frac{C - C_\infty}{C_w - C_\infty}. \quad (5.25)$$

Also $T = T_\infty + [1 + (\theta_w - 1)\theta]$, with $\theta_w (> 1)$ as the temperature ratio parameter and defined as $\theta_w = \frac{T_f}{T_\infty}$.

The velocity components in terms of new non-dimensional variables become

$$u = u_w f'(\eta), \quad w = -2u_w \text{Re}^{-1/2} f(\eta). \quad (5.26)$$

Utilizing Eqs. (5.24) and (5.25) into Eqs. (5.18) – (5.20), we finally get

$$\left[\beta^* + (1 - \beta^*) (1 - We f'')^{-2} \right] f''' - A \left(f' + \frac{\eta}{2} f'' \right) + 2f f'' - (f')^2 - M^2 f' = 0, \quad (5.27)$$

$$\theta'' + \text{Pr} \left(2f\theta' - \frac{A}{2} \eta \theta' + Nb\theta' \phi' + Nt(\theta')^2 \right) + \frac{4}{3N_R} \frac{d}{d\eta} \left[\{1 + (\theta_w - 1)\theta\}^3 \theta' \right] = 0, \quad (5.28)$$

$$\phi'' + 2Scf\phi' - \frac{A}{2} Sc\eta\phi' + \frac{Nt}{Nb}\theta'' = 0. \quad (5.29)$$

Consequently, the boundary conditions have the forms:

$$\begin{aligned} f(0) &= 0, \quad f'(0) = 1 + \alpha f''(0) [\beta^* + (1 - \beta^*) \{1 - We f''(0)\}^{-1}], \\ \theta'(0) &= -\gamma(1 - \theta(0)), \quad \phi(0) = 1, \quad f'(\infty) \rightarrow 0, \quad \theta(\infty) \rightarrow 0, \quad \phi(\infty) \rightarrow 0. \end{aligned} \quad (5.30)$$

The significant thermophysical parameters are elaborated as follows:

The local Weissenberg number $We^2 \left(= \frac{a^3 \Gamma^2 r^2}{\nu(1-cl)^3} \right)$, the non-linear radiation parameter $N_R \left(= \frac{kk^*}{4\sigma^{**}T_\infty^3} \right)$, the Schmidt number $Sc \left(= \frac{\nu}{D_B} \right)$, the generalized Biot number $\gamma \left(= \frac{rh_f}{k} Re^{-1/2} \right)$ and the velocity slip parameter $\alpha \left(= \frac{L_1}{r} Re^{1/2} \right)$.

5.2.1 Physical Quantities

The physical parameters of engineering concern are given by

$$C_{fr} = \frac{\tau_w|_{z=0}}{\rho u_w^2}, \quad Nu_r = \frac{rq_w|_{z=0}}{k(T_f - T_\infty)}, \quad Sh_r = \frac{rq_m|_{z=0}}{D_B(C_w - C_\infty)}, \quad (5.31)$$

where τ_w , q_w and q_m represent wall (shear stress, heat flux, mass flux) respectively, and given as:

$$\begin{aligned} \tau_w &= \mu_0 \frac{\partial u}{\partial z} \left[\beta^* + (1 - \beta^*) \left(1 - \Gamma \frac{\partial u}{\partial z} \right)^{-1} \right] \Big|_{z=0}, \\ q_w &= -k \left(\frac{\partial T}{\partial z} \right)_w + (q_r)_w, \text{ or } q_w = -k \left(1 + \frac{16\sigma^*}{3k^*} T^3 \right) \frac{\partial T}{\partial z} \Big|_w, \\ q_m &= -D_B \left(\frac{\partial C}{\partial z} \right)_{z=0}. \end{aligned} \quad (5.32)$$

Using (5.24), (5.25), (5.31) and (5.32), one gets

$$\begin{aligned} Re^{1/2} C_{fr} &= f''(0) \left[\beta^* + (1 - \beta^*) \{1 - We f''(0)\}^{-1} \right], \\ Re^{-1/2} Nu_r &= -\theta'(0) \left[1 + (4/3N_R) \{1 + (\theta_w - 1)\theta(0)\}^3 \right], \\ Re^{-1/2} Sh_r &= -\phi'(0). \end{aligned} \quad (5.33)$$

5.3 Numerical Scheme

The ordinary non-linear differential Eqs. (5.27), (5.28) and (5.29) with boundary conditions (5.30) are tackled numerically via Runge-Kutta-Fehlberg integration algorithm. Before we apply this method to the present problem, the coupled nonlinear Eqs. (5.27) – (5.29) which are third order in f and second order in θ and ϕ are reduce to the system of seven first-order ODEs of initial order seven unknowns are as follows:

$$\begin{aligned}
 f &= \tilde{A}, & f' &= \tilde{B}, & f'' &= \tilde{C}, & f''' &= \tilde{C}'; \\
 \theta &= \tilde{D}, & \theta' &= \tilde{E}, & \theta'' &= \tilde{E}'; \\
 \phi &= \tilde{F}, & \phi' &= \tilde{G}, & \phi'' &= \tilde{G}';
 \end{aligned} \tag{5.34}$$

Invoking Eq. (5.37) in Eqs. (5.29), (5.30) and (5.31), we obtain

$$\left[\beta^* + (1 - \beta^*) \left(1 - We\tilde{C} \right)^{-2} \right] \tilde{C}' - \tilde{B}^2 - A \left(\tilde{B} + \frac{\eta}{2} \tilde{C} \right) - M^2 \tilde{B} + 2\tilde{A}\tilde{C} = 0, \tag{5.35}$$

$$\begin{aligned}
 & \left\{ 3N_R + 4 \left[1 + (\theta_w - 1) \tilde{D} \right]^3 \right\} \tilde{E}' + 3N_R \text{Pr} \left[2\tilde{A}\tilde{E} - \frac{A}{2}\eta\tilde{E} + Nb\tilde{E}\tilde{G} + Nt\tilde{E}^2 \right] \\
 & + 12(\theta_w - 1) \left[1 + (\theta_w - 1) \tilde{D} \right]^2 \tilde{E}^2 = 0,
 \end{aligned} \tag{5.36}$$

$$\tilde{G}' + 2Sc\tilde{A}\tilde{G} + \frac{A}{2}Sc\eta\tilde{G} - \frac{Nt}{Nb}\tilde{E}' = 0. \tag{5.37}$$

The nonlinear BVP has been transformed to a system of seven simultaneous equations of first-order for seven unknowns as follows:

$$\begin{aligned}
\tilde{A}' &= \tilde{B}, \\
\tilde{B}' &= \tilde{C}, \\
\tilde{C}' &= \frac{\tilde{B}^2 + A(\tilde{B} + \frac{\eta}{2}\tilde{C}) + M^2\tilde{B} - 2\tilde{A}\tilde{C}}{[\beta^* + (1 - \beta^*)(1 - We\tilde{C})^{-2}]}, \tag{5.38}
\end{aligned}$$

$$\begin{aligned}
\tilde{D}' &= \tilde{E}, \\
\tilde{E}' &= \frac{\left\{ \begin{array}{l} -3N_R \text{Pr} \left[2\tilde{A}\tilde{E} - \frac{A}{2}\eta\tilde{E} + Nb\tilde{E}\tilde{G} + Nt\tilde{E}^2 \right] \\ -12(\theta_w - 1) \left[1 + (\theta_w - 1)\tilde{D} \right]^2 \tilde{E}^2 \end{array} \right\}}{3N_R + 4[1 + (\theta_w - 1)\tilde{D}]^3}, \tag{5.39}
\end{aligned}$$

$$\begin{aligned}
\tilde{F}' &= \tilde{G}, \\
\tilde{G}' &= -2Sc\tilde{A}\tilde{G} - \frac{A}{2}Sc\eta\tilde{G} + \frac{Nt}{Nb}\tilde{E}'. \tag{5.40}
\end{aligned}$$

The boundary conditions are:

$$\begin{aligned}
\tilde{A} &= 0, \quad \tilde{B} = 1 + \alpha\tilde{C} \left[\beta^* + (1 - \beta^*) \left\{ 1 - We\tilde{C} \right\}^{-1} \right], \\
\tilde{E} &= -\gamma(1 - \tilde{D}), \quad \tilde{F} = 1 \quad \text{at} \quad \eta = 0, \\
\tilde{B} &\rightarrow 0, \quad \tilde{D} \rightarrow 0, \quad \tilde{F} \rightarrow 0 \quad \text{as} \quad \eta \rightarrow \infty. \tag{5.41}
\end{aligned}$$

To solve Eqs. (5.38) – (5.40) with (5.41) as an initial value problem (IVP) the values for $\tilde{C}(0)$ *i.e.*, $f''(0)$, $\tilde{E}(0)$ *i.e.*, $\theta'(0)$ and $\tilde{G}(0)$ *i.e.*, $\phi'(0)$ are necessary; however, these values are not

indicated. Once all the seven initial conditions are determined then we solve this system of coincidental equations employing RKF-45 order technique.

5.3.1 Validation of Numerical Results

To validate the present numerical procedure, the above simulation results are tested with the results reported by Arial [103]. The numerical data $-f''(0)$ is compared with Arial [103] for varying values of slip parameter α by taking $We = A = M = \beta^* = 0$. **Table 5.1** shows the excellent correspondence between the two sets of results.

In addition, the computed numerical results are compared with those of Makinde *et al.* [104], who investigated the flow of electrically conducting nanofluids driven by a radially stretching convective surface with thermal radiation. **Table 5.2** highlights the values of friction coefficient for the case when $We = A = \alpha = \beta^* = 0$ are listed for different magnetic parameter M . As exhibited in this table, the results of current investigation are consistent with the data of Makinde *et al.*'s [104] work. Therefore, the numerical scheme of the current analysis is authorized.

5.4 Physical Description

This study is devoted to discuss the physical aspects of radiative Williamson nanofluid flow over a radially stretched surface. In this section, the impact of several leading non-dimensional parameters, namely, unsteadiness parameter A , viscosity ratio parameter β^* , magnetic parameter M , Weissenberg number We , Prandtl number Pr , velocity slip parameter α , temperature ratio parameter θ_w , thermal radiation parameter N_R on velocity, temperature and nanoparticles concentration are depicted graphically. The profiles for velocity $f'(\eta)$, temperature $\theta(\eta)$ and

concentration $\phi(\eta)$ are presented in **Figs. 5.2-5.9** for fixed values of the physical parameters $We = 1.0$, $A = 0.1$, $\beta^* = 0.2$, $\alpha = 0.1$, $M = 0.2$, $\gamma = 0.1$, $Pr = 2.5$, $Nt = 0.2$, $Nb = 0.1$, $N_R = 2.0$, $\theta_w = 1.2$ and $Sc = 2.0$.

Figs. 5.2(a-c) portray the $f'(\eta)$, $\theta(\eta)$ and $\phi(\eta)$ distributions by varying the numerical values of M . It is depicted through **Fig. 5.2(a)** that the velocity of nanofluids is depressed with increasing values of magnetic parameter by keeping the other parameters fixed. Likewise, the associated momentum boundary layer thickness reduces with higher M . Physically, it is justified that the higher magnetic parameter has the capacity to slow down the motion of fluid particles. This occurs due to Lorentz force which acts like a retarding force. From **Figs. 5.2(b)** and **5.2(c)** we observed that both temperature $\theta(\eta)$ and concentration $\phi(\eta)$ are boosted with the raising values of magnetic parameter within the boundary layer region. In addition, a similar trend is noted for both thermal and solutal boundary layer thickness with higher M .

Figs. 5.3(a-c) depict the variation of $f'(\eta)$, $\theta(\eta)$ and $\phi(\eta)$ with velocity slip parameter α . From this plot, it is understandable that the fluid velocity enhances by growing α . Additionally, it can also be reported that temperature and nanoparticles concentration and their corresponding thermal and concentration boundary layer thicknesses are reducing functions of α .

Figs. 5.4(a) and **5.4(b)** render the variation of $\theta(\eta)$ and $\phi(\eta)$ with varying A . It is perceived from these figures that the fluid temperature and nanoparticles concentration show a rising behavior with higher unsteadiness parameter. However, the corresponding boundary layer thickness is elevated by enhancing the unsteadiness parameter. In fact, an increment in unsteadiness parameter can boost the thermal and concentration fields.

Figs. 5.5(a) and **5.5(b)** are captured to depict the influence of θ_w and N_R on $\theta(\eta)$. From

these plots, it is observed that higher values of θ_w relate to larger wall temperature as compared to ambient fluid. As a result, temperature of the fluid as well as thermal boundary layer thickness increases. **Fig. 5.5(b)** demonstrates the impact of N_R on $\theta(\eta)$ profiles. This figure reveals that the nanofluid temperature depreciate by rising N_R .

Figs. 5.6(a) and **5.6(b)** are portrayed against the similarity variable η to see the effect of γ on $\theta(\eta)$ and $\phi(\eta)$. As an output of these plots, it is noted that temperature and nanoparticles concentration of the fluid as well as thermal and solutal boundary layer thicknesses enhance for growing γ . At $\gamma = 0$, the sheet is totally isolated. The interior thermal resistance of the sheet is extremely strong and convective heat transfer does not occur from the outside of sheet to the cool liquid far away from the sheet. However, the recorded effect in nanoparticle volume fraction is minimal.

The behavior of Nb on the nanofluid temperature and concentration within the hydrodynamic boundary layers are elucidated through **Figs. 5.7(a)** and **5.7(b)**. From these plots, it is observed that temperature and its related boundary layer thickness elevates for increasing values of Nb , but reverse pattern is observed for concentration profile. Brownian motion happens due to random movement of nanoparticles and caused a reduction in nanoparticle volume fraction within the boundary layer region.

Figs. 5.8(a) and **5.8(b)** are displayed to examine the impact of Nt and Sc on $\phi(\eta)$. It is visualized that concentration field and corresponding boundary solutal boundary layer thickness suppress with uplifting Nt . Physically, higher values of Nt increases the temperature difference between the ambient and surface and it results in a growth in nanofluid temperature and concentration. **Fig. 5.8(b)** displays the impact of Sc on $\phi(\eta)$. The Schmidt number embodies the ratio of kinematic viscosity to molecular mass diffusivity for an increment in Sc yields a

reduction in mass diffusivity in the system which yields a decline in nanoparticles concentration.

The variation in non-dimensional skin friction against magnetic parameter for different values of α is depicted in **Fig. 5.9(a)**. As seen earlier, the fluid velocity reduces for magnetic parameter because of the Lorentz force generated by magnetic field, consequently, the skin friction depicts the similar behavior for higher magnetic parameter as shown in this figure. It is further noted that the dimensionless skin friction enhances as the velocity slip parameter increases. The local Nusselt number is sketched through **Fig. 5.9(b)**, against the Prandtl number Pr for several values of thermophoresis parameter Nt . These plots highlight that the rate of heat transfer reduces with a growth in thermophoresis parameter. This is because of the fact that higher thermophoretic force drags the nanoparticles with large thermal conductivity from the hotter region to the ambient fluid. Further, the impact of Pr on the heat transfer rate is to increase its magnitude. Finally, the effect of Sc on the dimensionless Sherwood number against α is depicted in **Fig. 5.9(c)**. This figure reveals that the reduced Sherwood number is higher for larger velocity slip parameter i.e., the Sherwood number is a decreasing function of α . It is clear from this figure that higher curves corresponds to the higher values of Sc .

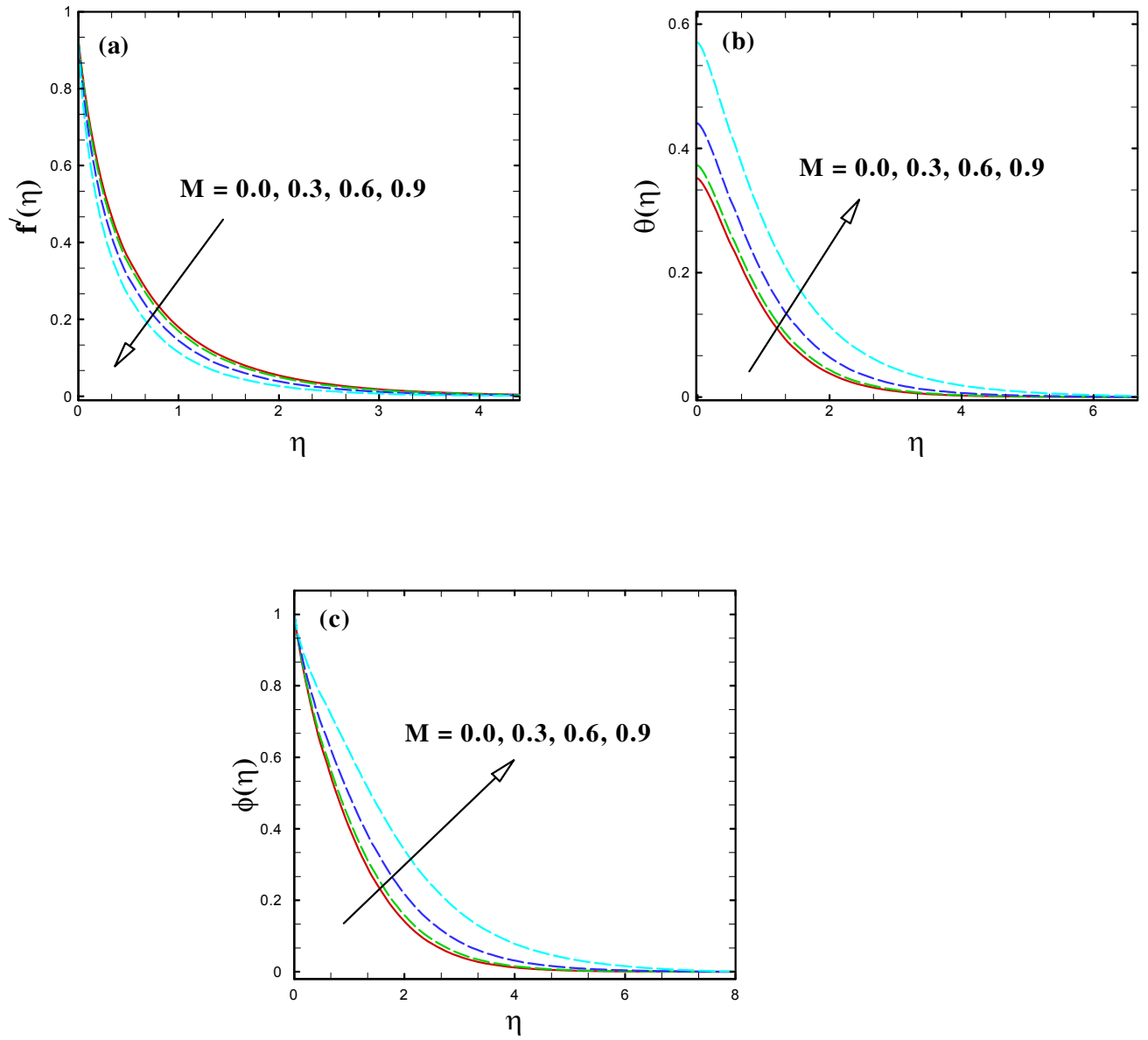


Fig. 5.2: The variation of M on $f'(\eta)$, $\theta(\eta)$ and $\phi(\eta)$.

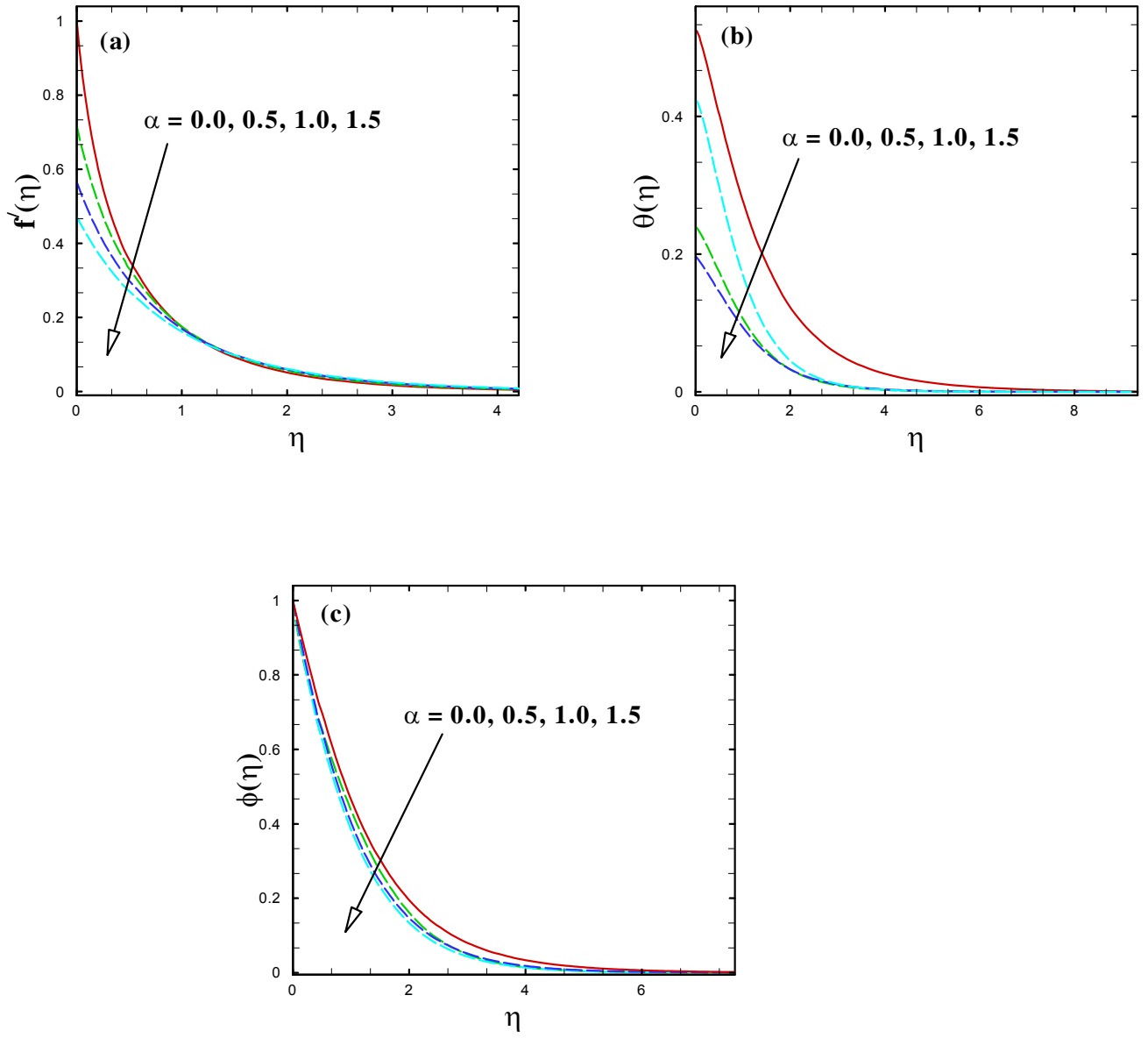


Fig. 5.3: The variation of α on $f'(\eta)$, $\theta(\eta)$ and $\phi(\eta)$.

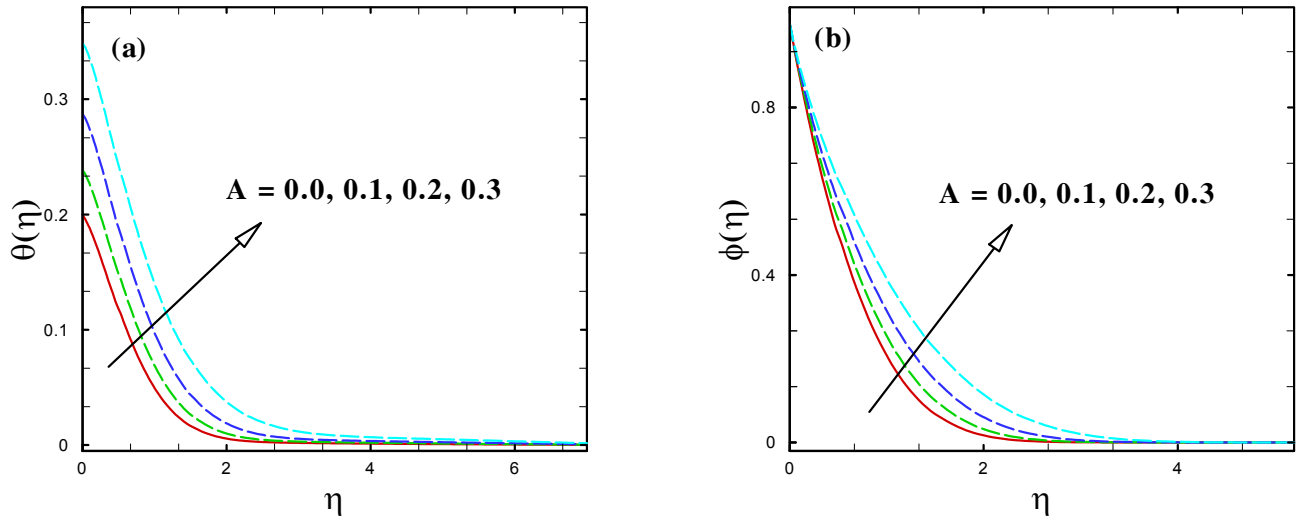


Fig. 5.4: The variation of A on $\theta(\eta)$ and $\phi(\eta)$.

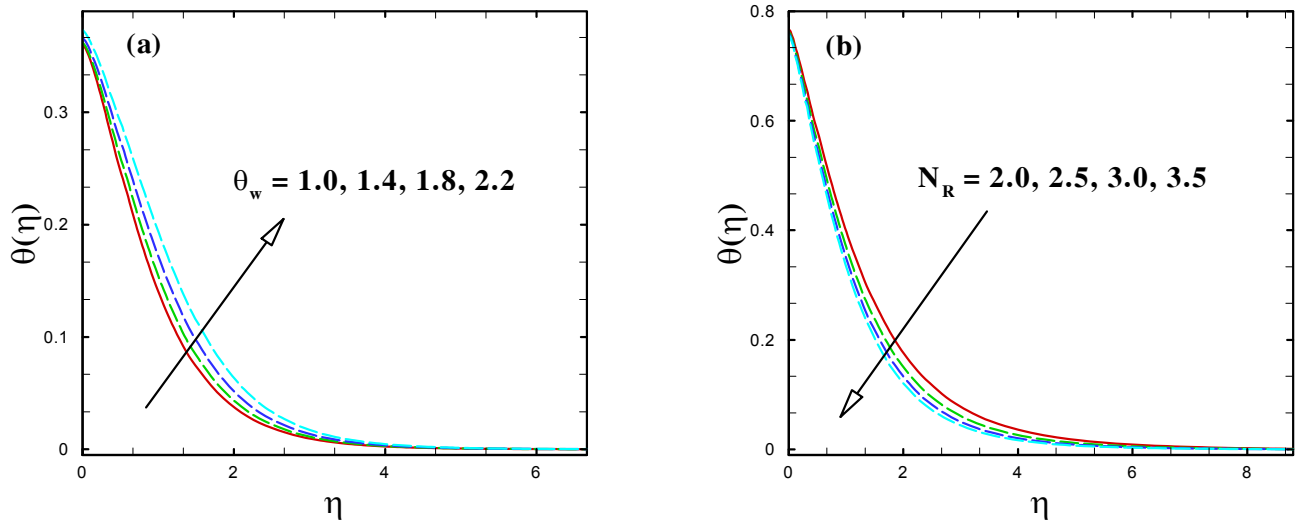


Fig. 5.5: The variation of θ_w and N_R on $\theta(\eta)$.

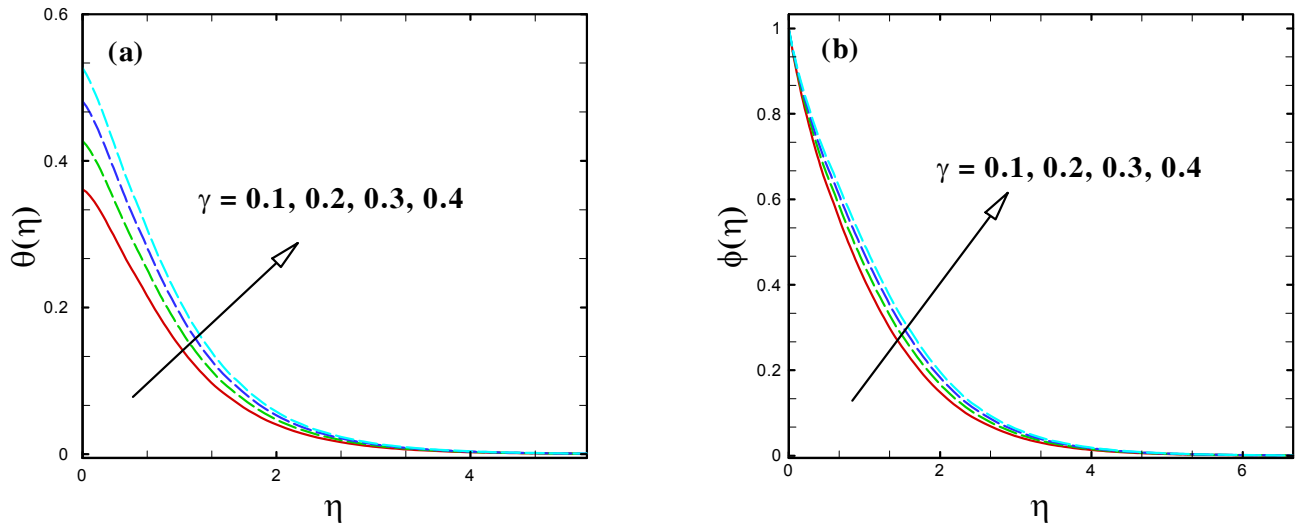


Fig. 5.6: The variation of γ on $\theta(\eta)$ and $\phi(\eta)$.

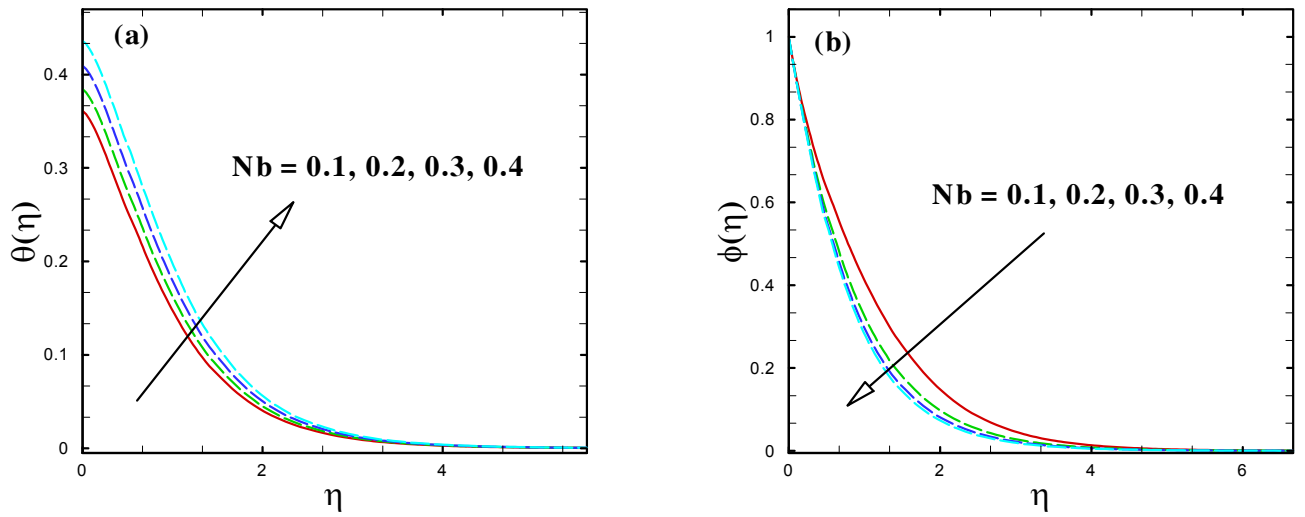


Fig. 5.7: The variation of Nb on $\theta(\eta)$ and $\phi(\eta)$.

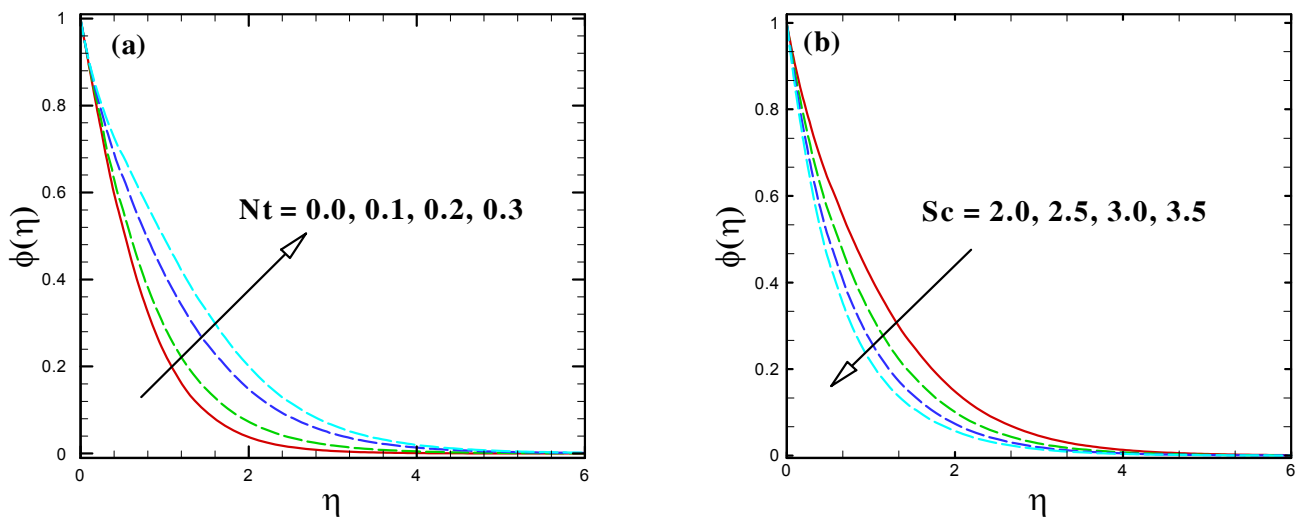


Fig. 5.8: The variation of Nt and Sc on $\phi(\eta)$.

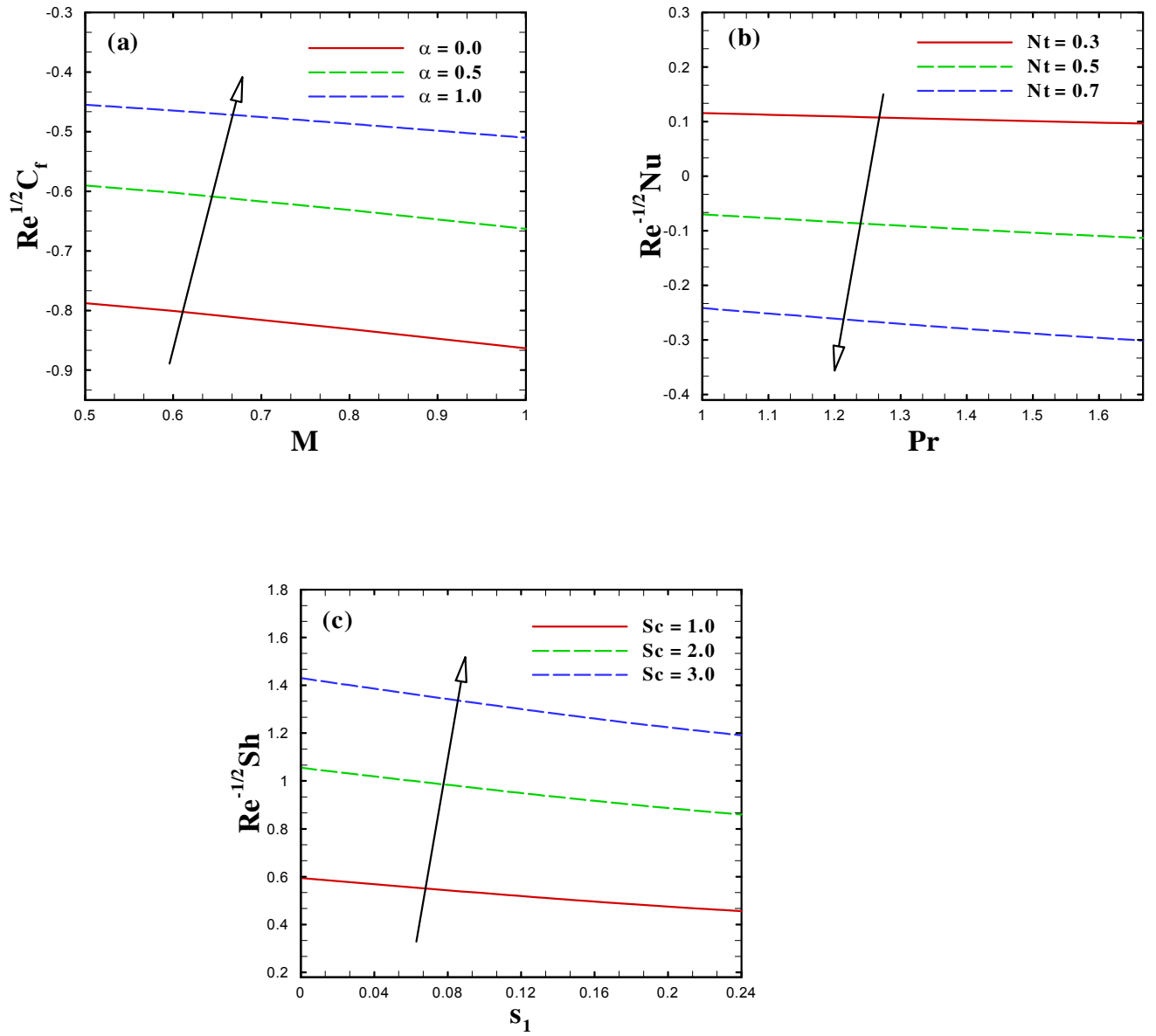


Fig. 5.9: The variation of α , Nt and Sc on $Re^{1/2} C_{fr}$, $Re^{-1/2} Nu_r$ and $Re^{-1/2} Sh_r$.

Table 5.1: Comparison of the $\text{Re}^{1/2} C_{fr}$ for different values of α when $We = M = A = \beta^* = 0$.

α	[$-f''(0)$]				
	Exact [103]	HPM [103]	Perturbation [103]	Asymptotic [103]	Present survey
0.0	1.1737210	1.1785110	1.1737210	—	1.17373
0.01	1.1534720	1.1573110	1.1534810	—	1.15348
0.02	1.1340170	1.1369980	1.1340900	—	1.13403
0.05	1.0799490	1.0808200	1.0810100	—	1.07996
0.1	1.0018340	1.0003080	1.0095220	—	1.00185
0.2	0.8784250	0.8744530	0.9302130	—	0.87844
0.5	0.6505280	0.6453040	1.2016230	1.5299180	0.65056
1.0	0.4625100	0.4583330	—	0.5741630	0.46254
2.0	0.2990500	0.2965340	—	0.3107530	0.29090
5.0	0.1493930	0.1484540	—	0.1495900	0.14945
10.0	0.0829120	0.0825320	—	0.0828330	0.08297
20.0	0.0443680	0.0442280	—	0.0443370	0.04442
50.0	0.018732	0.0186980	—	0.0187270	0.01877
100.0	0.009594	0.0095830	—	0.0095930	0.009618

Table 5.2: Comparison of the $\text{Re}^{1/2} C_{f_r}$ for different values of M^2 when $We = A = \alpha = \beta^* = 0$.

M^2	Makinde <i>et al.</i> [104]	Present survey
0.0	-1.17372	-1.173720
0.5	-1.36581	-1.365830
1.0	-1.53571	-1.535710
2.0	-1.83049	-1.830510
3.0	-2.08484	-2.084850

Chapter 6

Unsteady Mixed Convective Flow of Williamson Nanofluid with Variable Thermal Conductivity

This chapter focuses on time-dependent flow of Williamson fluid past a radially stretched surface in the presence of nanoparticles. The analysis is done under the influence of variable magnetic field, mixed convection and newly proposed zero nanoparticles mass flux condition. An efficient Runge-Kutta integration scheme is implemented to obtain the numerical solutions for velocity, temperature and concentration distributions for various set of physical parameters. The obtained results disclose that higher magnetic field reduces the nanofluids velocity as well as momentum boundary layer thickness. We observe an increment in heat transport rate with Schmidt number.

6.1 Problem Formulation

We examine the unsteady and incompressible Williamson nanofluid flow past a radially stretched surface coinciding with plane ($z = 0$) and the fluid appears in the upper half of the space ($z \geq 0$), as depicted in **Fig. 6.1**. The basic assumptions for current analysis are listed below:

1. Time-dependent flow.
2. Williamson fluid model.
3. Mixed convection flow.
4. Impact of variable thermal conductivity on heat transport.
5. Revised model for nanoparticles mass flux.
6. Heat generation/absorption effects.

Further, the surface fluid temperature T_w and ambient fluid temperature T_∞ are supposed to be constant where $T_w > T_\infty$. A variable magnetic field $B(t) = \frac{B_0}{(1-ct)^{1/2}}$ is applied perpendicular to the plane of sheet.

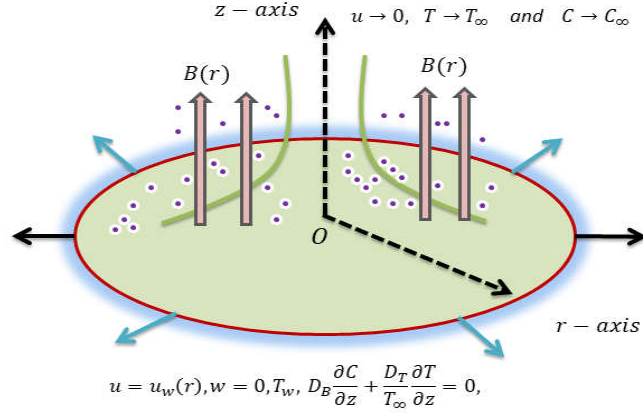


Fig. 6.1: Schematic diagram.

In view of aforesaid assumptions, the basic relations take the form:

$$\frac{\partial u}{\partial r} + \frac{u}{r} + \frac{\partial w}{\partial z} = 0, \quad (6.1)$$

$$\begin{aligned} \frac{\partial u}{\partial t} + u \frac{\partial u}{\partial r} + w \frac{\partial u}{\partial z} &= \nu \frac{\partial^2 u}{\partial z^2} \left[\beta^* + (1 - \beta^*) \left(1 - \Gamma \frac{\partial u}{\partial z} \right)^{-1} \right] + g\beta_T(T - T_\infty) + g\beta_C(C - C_\infty) \\ &+ \nu \Gamma \left(\frac{\partial u}{\partial z} \right) \frac{\partial^2 u}{\partial z^2} \left[(1 - \beta^*) \left(1 - \Gamma \frac{\partial u}{\partial z} \right)^{-2} \right] - \frac{\sigma B(t)^2}{\rho} u, \end{aligned} \quad (6.2)$$

$$\begin{aligned} \frac{\partial T}{\partial t} + u \frac{\partial T}{\partial r} + w \frac{\partial T}{\partial z} &= \frac{1}{(\rho c)_f} \frac{\partial}{\partial z} \left(K(T) \frac{\partial T}{\partial z} \right) \\ + \tau \left[D_B \frac{\partial C}{\partial z} \frac{\partial T}{\partial z} + \frac{D_T}{T_\infty} \left(\frac{\partial T}{\partial z} \right)^2 \right] &+ \frac{Q_0}{(\rho c)_f} (T - T_\infty), \end{aligned} \quad (6.3)$$

$$\frac{\partial C}{\partial t} + u \frac{\partial C}{\partial r} + v \frac{\partial C}{\partial z} = D_B \frac{\partial^2 C}{\partial z^2} + \frac{D_T}{T_\infty} \frac{\partial^2 T}{\partial z^2}. \quad (6.4)$$

The boundary conditions are:

$$u = u_w(r, t) = \frac{ar}{1 - ct}, \quad w = 0, \quad T = T_w, \quad D_B \frac{\partial C}{\partial z} + \frac{D_T}{T_\infty} \frac{\partial T}{\partial z} = 0, \quad \text{at } z = 0, \quad (6.5)$$

$$u \rightarrow 0, \quad T \rightarrow T_\infty, \quad C \rightarrow C_\infty \quad \text{as } z \rightarrow \infty. \quad (6.6)$$

The stream-function and non-dimensional variables are defined as:

$$\eta = \frac{z}{r} \text{Re}^{1/2}, \quad \psi(r, z, t) = -r^2 u_w \text{Re}^{-1/2} f(\eta), \quad \theta(\eta) = \frac{T - T_\infty}{T_w - T_\infty} \quad \text{and} \quad \phi(\eta) = \frac{C - C_\infty}{C_\infty}. \quad (6.7)$$

The variable thermal conductivity $K(T)$ is given by the following relation:

$$K(T) = k_\infty \left[1 + \varepsilon \left(\frac{T - T_\infty}{\Delta T} \right) \right]. \quad (6.8)$$

The new velocity components are defined as:

$$u = u_w f'(\eta), \quad w = -2u_w \text{Re}^{-1/2} f(\eta). \quad (6.9)$$

Substituting Eqs. (6.7) – (6.9) into Eqs. (6.2) – (6.4), we finally get

$$\begin{aligned} \left[\beta^* + (1 - \beta^*) (1 - We f'')^{-2} \right] f''' - A \left(f' + \frac{\eta}{2} f'' \right) + 2f f'' - (f')^2 \\ - M^2 f' + \lambda (\theta + N\phi) = 0, \end{aligned} \quad (6.10)$$

$$(1 + \varepsilon\theta) \theta'' + \varepsilon (\theta')^2 + \text{Pr} \left(2f\theta' - \frac{A}{2} \eta \theta' + Nb\theta' \phi' + Nt (\theta')^2 + \delta\theta \right) = 0, \quad (6.11)$$

$$\phi'' + 2Sc_f \phi' - \frac{A}{2} Sc_\eta \phi' + \frac{Nt}{Nb} \theta'' = 0, \quad (6.12)$$

with associated boundary conditions:

$$\begin{aligned} f(0) &= 0, & f'(0) &= 1, & \theta(0) &= 1, & Nb\phi'(0) + Nt\theta'(0) &= 0, \\ f'(\infty) &\rightarrow 0 & \theta(\infty) &\rightarrow 0, & \phi(\infty) &\rightarrow 0. \end{aligned} \quad (6.13)$$

The dimensionless physical parameters are defined as below:

$\xi \left(= \frac{g\beta_T(T_w - T_\infty)r}{u^2} \right)$ the buoyancy force parameter, $N \left(= \frac{\beta_C}{\beta_T} \left(\frac{C_\infty}{T_w - T_\infty} \right) \right)$ buoyancy forces ratio parameter, $Nb \left(= \frac{\tau D_B C_\infty}{\nu} \right)$ the Brownian motion parameter and $\delta \left(= \frac{Q_0(1-ct)}{a(\rho c)_f} \right)$ the heat generation/absorption parameter.

6.1.1 Engineering and Industrial Parameters of Interest

Quantities of pragmatic importance in this analysis are the coefficient of skin-friction and Nusselt number, which are written as:

$$C_f = \frac{\tau_w|_{z=0}}{\rho u_w^2}, \quad Nu_r = \frac{r q_w|_{z=0}}{k(T_w - T_\infty)}, \quad (6.14)$$

where

$$\tau_w = \mu_0 \frac{\partial u}{\partial z} \left[\beta^* + (1 - \beta^*) \left(1 - \Gamma \frac{\partial u}{\partial z} \right)^{-1} \right] \Big|_{z=0}, \quad q_w = -k \left(\frac{\partial T}{\partial z} \right)_w. \quad (6.15)$$

On substituting Eq. (6.16) into Eq. (6.15), we get

$$\text{Re}^{1/2} C_f = f''(0) \left[\beta^* + (1 - \beta^*) \{1 - We f''(0)\}^{-1} \right], \quad \text{Re}^{-1/2} Nu = -\theta'(0). \quad (6.16)$$

6.1.2 Numerical Method for Solution

The governing Eqs. (6.10) – (6.12) with BCs (6.13) are solved numerically using RK-Fehlberg method with shooting scheme. To do this, the system of nonlinear ODEs must be transformed to a first-order linear system.

Let

$$f = u_1, \quad f' = u_2, \quad f'' = u_3, \quad \theta = u_4, \quad \theta' = u_5, \quad \phi = u_6, \quad \phi' = u_7. \quad (6.17)$$

Therefore, the leading equations become

$$u'_1 = u_2, \quad u'_2 = u_3, \quad u'_3 = \frac{u_2^2 + A(u_2 + \frac{\eta}{2}u_3) + M^2u_2 - 2u_1u_3 - \lambda(u_4 + Nu_6)}{\left[\beta^* + (1 - \beta^*)(1 - Weu_3)^{-2}\right]}, \quad (6.18)$$

$$u'_4 = u_5, \quad u'_5 = \frac{-\varepsilon u_5^2 - Pr \left[2u_1u_5 - \frac{A}{2}\eta u_5 + Nbu_5u_7 + Ntu_5^2 - \delta u_4\right]}{[1 + \varepsilon u_4]}, \quad (6.19)$$

$$u'_6 = u_7, \quad u'_7 = -2Scu_1u_7 - \frac{A}{2}Sc\eta u_7 + \frac{Nt}{Nb}u'_5, \quad (6.20)$$

and the boundary conditions

$$u_1(0) = 0, \quad u_2(0) = 1, \quad Ntu_5(0) + Nbu_7(0) = 0, \quad (6.21)$$

$$u_2(\infty) = 0, \quad u_4(\infty) = 0, \quad u_6(\infty) = 0. \quad (6.22)$$

Now, Runge-Kutta Fehlberg technique is employed for step by step integration and calculation are carried out using MATLAB software.

6.1.3 Numerical Validation of the Algorithm

To have a check on the accuracy of computed results in this study via Runge-Kutta-Fehlberg integration scheme, a comparison of presently computed values of skin friction coefficient is made for several values of M and A . To do this, the acquired results are validated against Makinde *et al.* [104], as shown in **Table 6.1**. It is seen that the numerical data of the current investigation are in an excellent agreement.

6.2 Numerical Results

In this section, we have noticed the effects of mixed convection, variable thermal conductivity, heat generation/absorption and magnetic field for momentum, thermal and concentration boundary layers. The emerging mathematical problem is governed by active physical parameters which include unsteadiness parameter A , viscosity ratio parameter β^* , magnetic parameter M , buoyancy force parameter ξ , buoyancy forces ratio parameter N , Weissenberg number We , thermophoresis parameter Nt , Prandtl number Pr , Brownian movement parameter Nb and heat generation/absorption parameter δ . The dimensionless profiles of velocity, temperature, concentration, skin-friction and Nusselt number are delineated graphically in **Figs. 6.2 – 6.8**. In the present study, the accompanying default values of physical parameters are: $We = 1.0$, $\beta^* = 0.001$, $A = 0.2$, $M = 1.0$, $Nb = 0.1$, $Nt = 0.2$, $N = 0.1$, $0 \leq Pr \leq 5.0$, $0 \leq Sc \leq 2.0$, $0 \leq \xi \leq 0.1$, $0 \leq \delta \leq 0.1$, $0 \leq \varepsilon \leq 0.1$. All graphs therefore correspond to these values unless particularly demonstrated in the appropriate graph.

Figs. 6.2(a – c) render the variation of M on $f'(\eta)$, $\theta(\eta)$ and $\phi(\eta)$, respectively. It is visualized via **Fig. 6.2(a)** that the $f'(\eta)$ is decreased for higher M . It has been described in

many physical situations that magnetic field reduces the velocity of fluid particles. Physically, we can say that a drag force that applies normal to sheet surface and hence reduces the motion of fluid. It is further noticed that a growth in magnetic parameter tends to enhance the temperature distribution as seen through **Fig. 6.2(b)**. **Fig. 6.2(c)** displays the deviation of concentration profile $\phi(\eta)$ for distinct M . One can see that a dual behavior for concentration profiles. The pattern of species concentration is initially raised by higher M near the solid surface. However, a contrary behavior is portrayed as we go along the dimensionless parameter η , that is a reduction in concentration is observed with larger M .

The characteristics of $f'(\eta)$ and $\theta(\eta)$ for different ξ are shown in **Figs. 6.3(a, b)**. It is observed that higher values of ξ rises the velocity and diminishes the temperature field. Since the buoyancy force is dominant over viscous force for higher ξ . Subsequently, buoyancy force parameter enhances the fluid flow which tends to increase $f'(\eta)$ and associated boundary layer thickness. Additionally, since the buoyancy force tends to enhance the temperature gradient, hence, $\theta(\eta)$ and corresponding boundary layer thickness decrease by higher values of ξ . Effect of N on $f'(\eta)$ and $\theta(\eta)$ are displayed in **Figs. 6.4(a, b)**. From these graphs, it is evident that an increase in N decreases the fluid velocity but an opposite is true for temperature profiles. When both thermal and concentration buoyancy forces are acting which results in uplift the momentum boundary layer and velocity shoots are computed. However, thickness of the thermal boundary layer is improved with increasing efficient buoyancy opposition.

Figs. 6.5(a, b) are sketched to inspect the influence of ε and δ on $\theta(\eta)$. It is reported that the fluid temperature enhances with an expansion in ε and δ . Physically, a lot of heat is exchange from surface to the material when ε is raised and thus temperature of the fluid increases. It is also reported that heat generation occurs in thermal boundary layer for growing

estimations of δ (heat source) and henceforth temperature rises.

Figs. 6.6(a, b) are drawn to explore the effect of Nt on $\theta(\eta)$ and $\phi(\eta)$, respectively. From figure **6.6(a)**, it is analyzed that an enlargement in thermophoresis parameter leads to boost the fluid temperature. The physical fact behind this phenomenon is that the large values of Nt , produces a strong thermophoresis force which have a tendency to transport the nanoparticles from heated surface to cold ambient fluid and consequently the fluid temperature is elevated in boundary-layer regime. Furthermore, higher values of Nt correspond to a greater boundary layer thickness. It is interesting to note that $\phi(\eta)$ decays with growing estimations of Nt within the small region $0 \leq \eta \leq 0.8$. However, after this region they change their physical behavior and goes on increasing with Nt . **Fig. 6.6(b)** depicts the concentration distribution due to variation in thermophoresis parameter. Since concentration profiles are driven by temperature gradient which is an increasing function of Nt . Therefore, an increasing value of Nt improves the concentration and solutal boundary layer thickness.

The Brownian motion is an important factor to check the proficiency of heat transfer during the motion of nanofluids. Due to this random motion, nanoparticles collide with each other and transfer the kinetic energy between each other. **Figs. 6.7(a)** and **6.7(b)** demonstrate the consequence of Brownian motion parameter Nb on $\theta(\eta)$ and $\phi(\eta)$. It is found that $\theta(\eta)$ decreases for larger values of Nb . In addition, the concentration profiles elucidate an opposite behavior for growing values of Nb . We observe that both concentration and thickness of boundary-layer reduce subjected to large estimations of Brownian motion parameter.

The variation of $Re^{1/2} C_f$ with diverse values of ξ is depicted in **Fig. 6.8(a)**. Wall shear stress at the surface enhances by higher buoyancy force parameter. We further anticipate that as the value of magnetic parameter M becomes higher, the friction coefficient takes the smaller

values. This behavior occurs due to drag force which creates resistance in the motion of fluid particles. **Fig. 6.8(b)** explains the impact of Schmidt number Sc on heat transfer coefficient as a function of Nt . It is shown in **Fig. 6.8(b)** that the heat transport coefficient reduces for increasing values of Schmidt number by keeping Nt fixed. But in contrast, the numerical results of heat transport coefficients with increasing values of Nt are completely different. This is due to the fact that higher Sc relates to a poor thermophoresis diffusion coefficient which tends to short penetration depth for nanoparticles concentration. It is also reported that in contrast with the past investigations on constant wall nanoparticles volume fraction, here the reduced Nusselt number is not depending on Nb . This result is predictable and can be effectively checked by utilizing $\phi'(0) = -(Nt/Nb)\theta'(0)$ in the energy equation (6.31) as we move towards the surface. In **Fig. 6.8(c)**, results of Nusselt number are shown as a function of Nt for varying Pr . We can see that, the Nusselt number is a decreasing functions of Nt due to loss of concentration at the surface. It is further revealed that the rate of heat transfer increases for augmenting Pr .

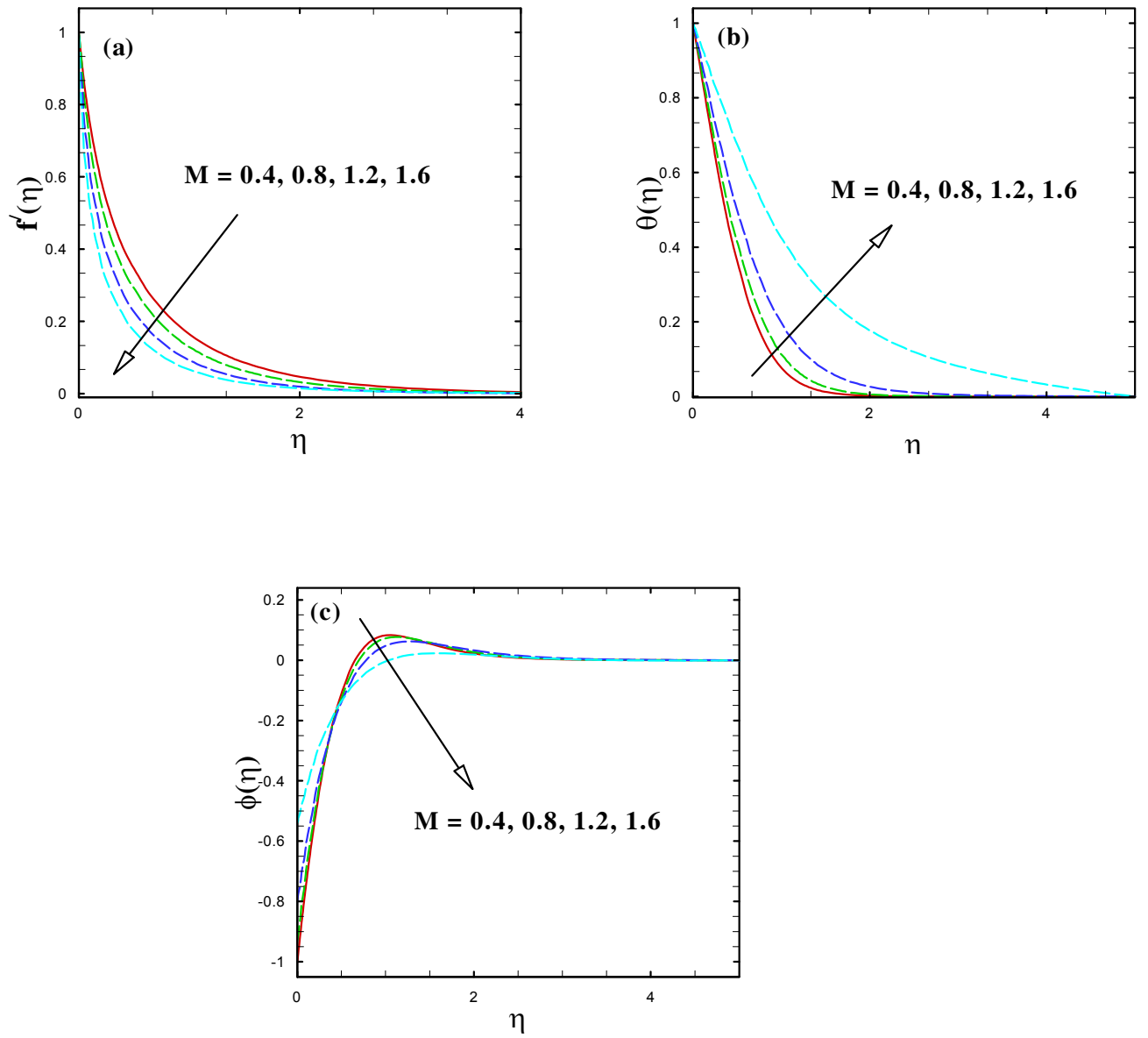


Fig. 6.2: Influence of varying M on $f'(\eta)$, $\theta(\eta)$ and $\phi(\eta)$.

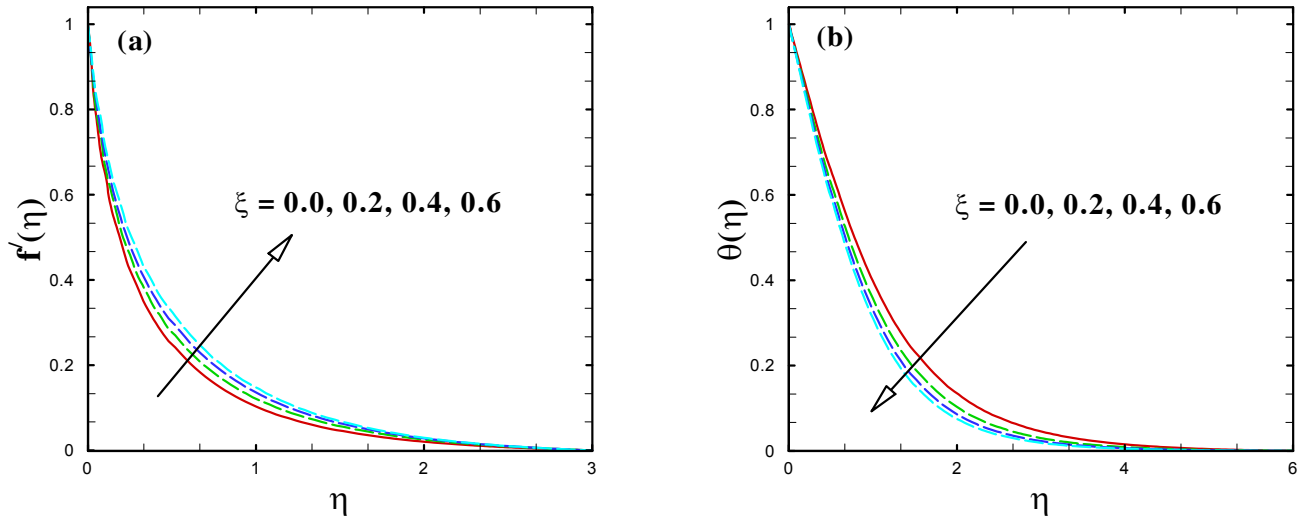


Fig. 6.3: Influence of varying ξ on $f'(\eta)$ and $\theta(\eta)$.

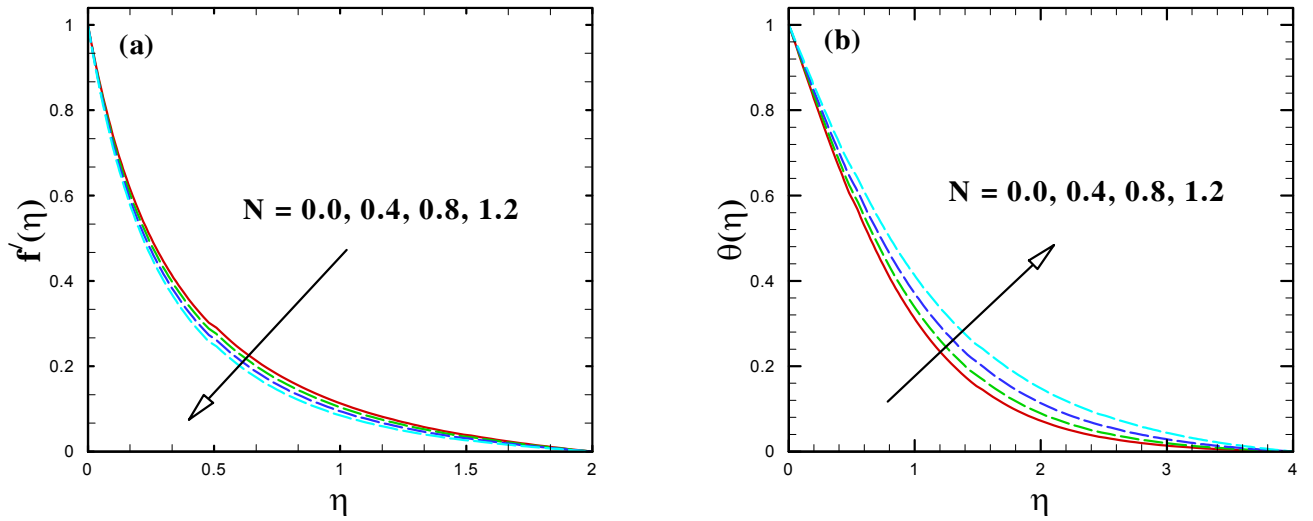


Fig. 6.4: Influence of varying N on $f'(\eta)$ and $\theta(\eta)$.

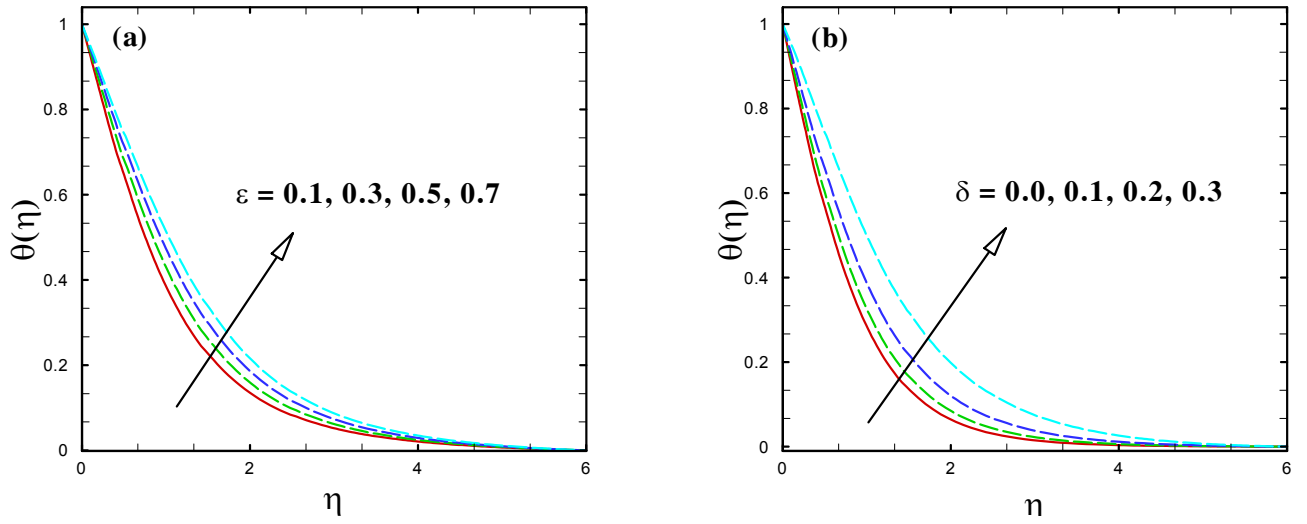


Fig. 6.5: Influence of varying ε and δ on $\theta(\eta)$.

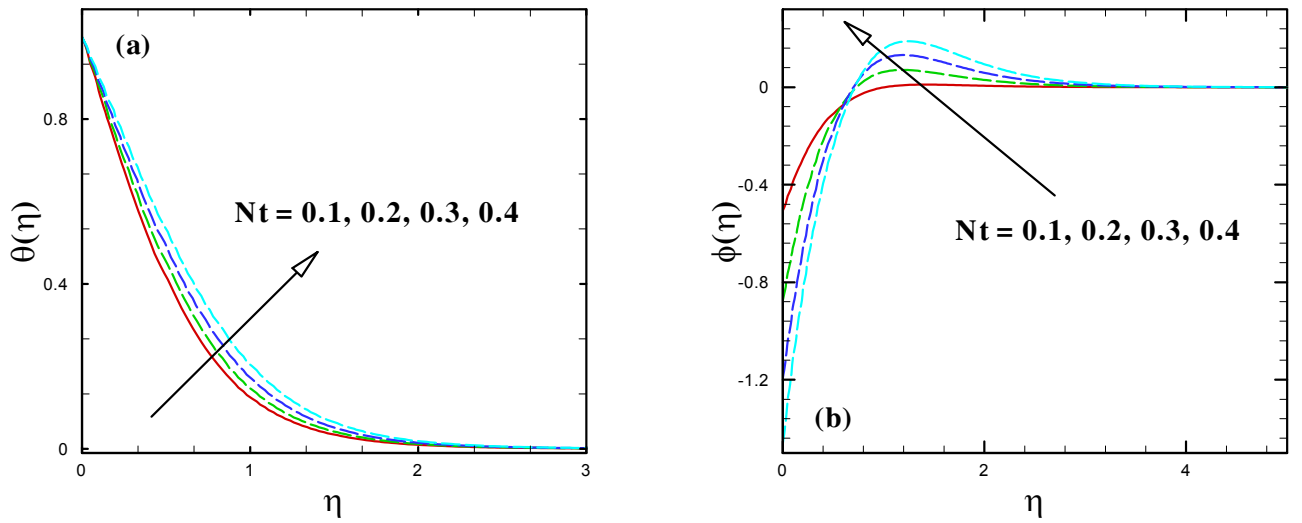


Fig. 6.6: Influence of varying Nt on $\theta(\eta)$ and $\phi(\eta)$.

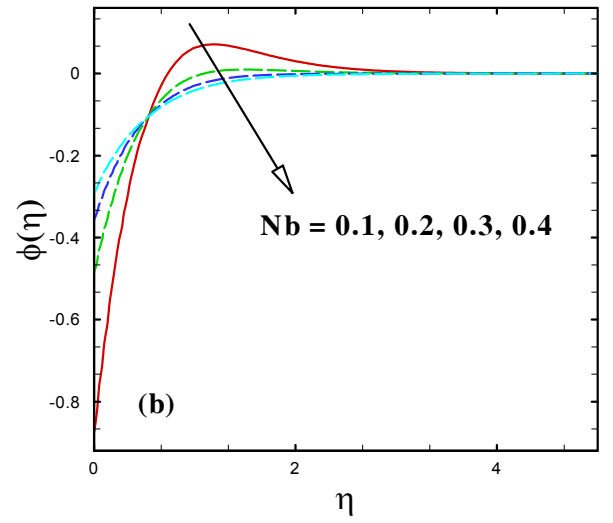
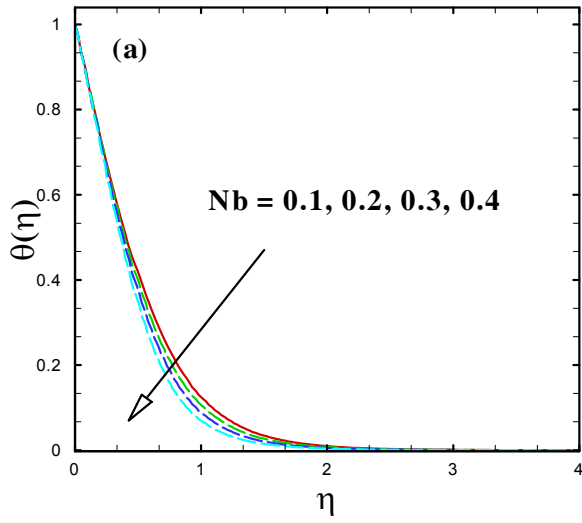


Fig. 6.7: Influence of varying Nb on $\phi(\eta)$.

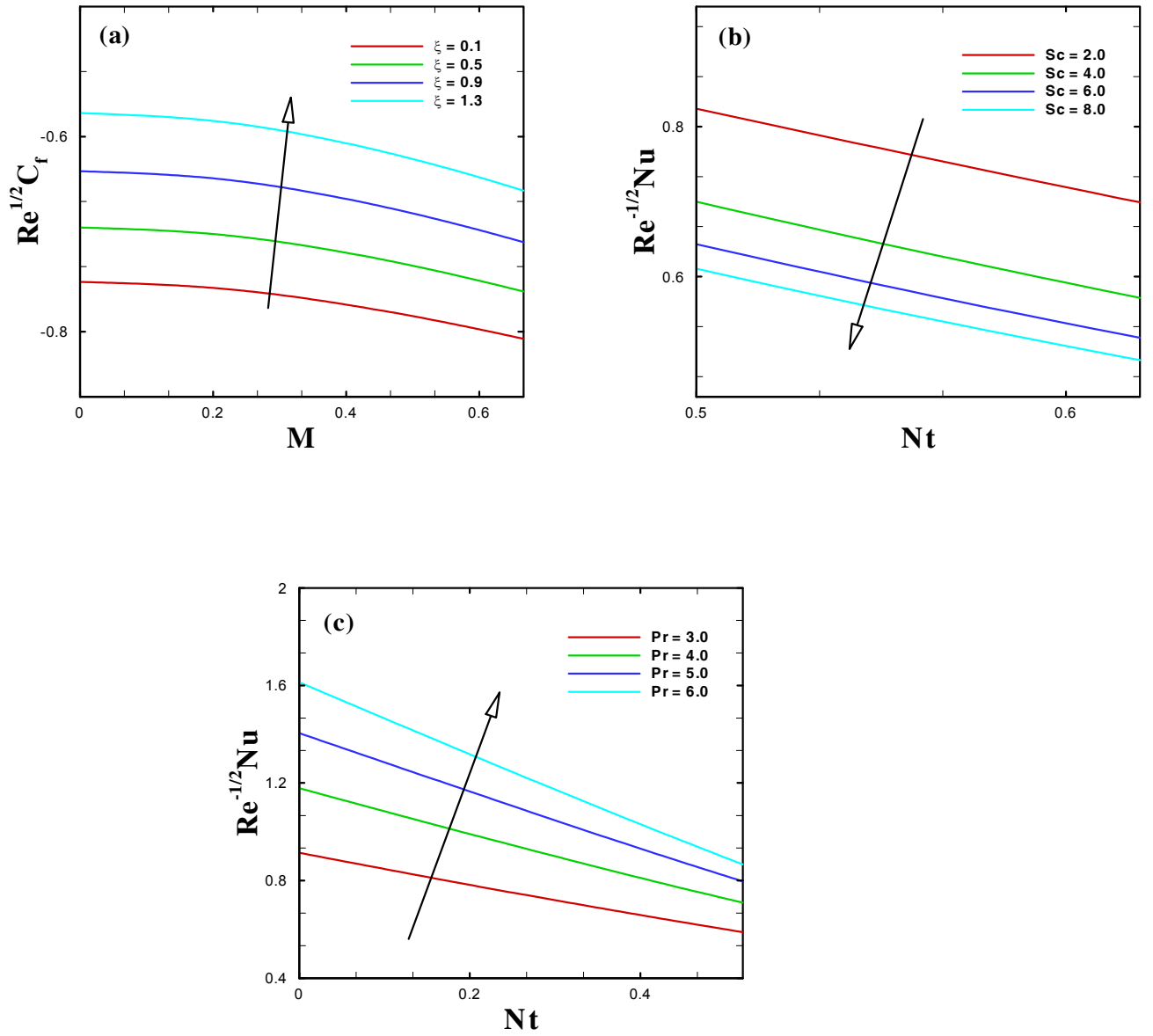


Fig. 6.8: Influence of varying ξ on $Re^{1/2} C_f$, Sc and Pr on $Re^{-1/2} Nu$.

Table 6.1: A comparison of the $\text{Re}^{1/2} C_f$ for varying M^2 when $We = \xi = N = A = \beta^* = 0$.

M^2	Makinde <i>et al.</i> [104]	Present results
0.0	-1.17372	-1.173988
0.5	-1.36581	-1.3658126
1.0	-1.53571	-1.5357173
2.0	-1.83049	-1.8304917
3.0	-2.08484	-2.0848529

Chapter 7

Chemically Reacting Flow of Williamson Nanofluid by a Stretching Cylinder

In this chapter, the simultaneous characteristics of heat absorption/generation and variable magnetic field on unsteady flow of Williamson fluid by a stretched cylinder subject to nanoparticles have been studied. An important prospective of this chapter is to incorporate the impacts of binary chemical reaction and activation energy for revised Buongiorno's model of nanofluid. The notion of Boussinesq-approximations is utilized to model the leading equations of momentum, thermal energy and nanoparticles concentration for Williamson nanofluids. The numerical simulations are carried out with the help of Runge-Kutta Fehlberg scheme coupled with shooting iteration procedure. The analysis of the obtained results revealed that the assumed physical model is significantly influenced by the key physical parameters, like, magnetic parameter, chemical reaction parameter, activation energy parameter,

heat generation/absorption parameter, Brownian motion and thermophoresis parameter. The physical performance of influential parameters are exhibited through graphs.

7.1 Problem Modelling

A time-dependent flow of chemically reacting Williamson fluid past a circular stretched cylinder subject to suspended nanoparticles has been investigated. The impact of Arrhenius activation energy and heat absorption/generation are further exhibited. The geometry and coordinate system for the current model is shown in **Fig. 7.1**. A non-uniform magnetic field is imposed normal to cylinder and fluid is presumed to be electrically conducting with strength $B(t) = \frac{B_0}{\sqrt{1-ct}}$, where B_0 is a constant. Finally, $u_w(x, t) = \frac{ax}{1-ct}$ is the stretching velocity of the cylinder.

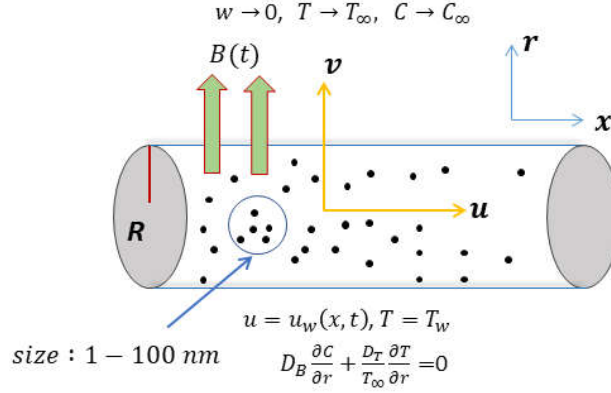


Fig. 7.1: Flow configuration.

As per as the stated restrictions, the pertinent equations of momentum, energy and concentration conservations for Williamson nanofluids flow are given by:

Continuity equation:

$$\frac{\partial (ru)}{\partial x} + \frac{\partial (rv)}{\partial r} = 0, \quad (7.1)$$

Momentum equation:

$$\begin{aligned} \frac{\partial u}{\partial t} + u \frac{\partial u}{\partial x} + v \frac{\partial u}{\partial r} &= \frac{\nu}{r} \frac{\partial u}{\partial r} \left[\beta^* + (1 - \beta^*) \left(1 - \Gamma \frac{\partial u}{\partial r} \right)^{-1} \right] \\ &+ \nu \Gamma \frac{\partial u}{\partial r} \frac{\partial^2 u}{\partial r^2} \left[(1 - \beta^*) \left(1 - \Gamma \frac{\partial u}{\partial r} \right)^{-2} \right] \\ &+ \nu \frac{\partial^2 u}{\partial r^2} \left[\beta^* + (1 - \beta^*) \left(1 - \Gamma \frac{\partial u}{\partial r} \right)^{-1} \right] - \frac{\sigma B^2(t)}{\rho} u, \end{aligned} \quad (7.2)$$

Energy equation:

$$\frac{\partial T}{\partial t} + u \frac{\partial T}{\partial x} + v \frac{\partial T}{\partial r} = \frac{k}{\rho c_p} \left(\frac{\partial^2 T}{\partial r^2} + \frac{1}{r} \frac{\partial T}{\partial r} \right) + \tau \left[D_B \frac{\partial C}{\partial r} \frac{\partial T}{\partial r} + \frac{D_T}{T_\infty} \left(\frac{\partial T}{\partial r} \right)^2 \right] + \frac{Q_0}{(\rho c)_f} (T - T_\infty), \quad (7.3)$$

Concentration equation:

$$\begin{aligned} \frac{\partial C}{\partial t} + u \frac{\partial C}{\partial x} + v \frac{\partial C}{\partial r} = \frac{D_B}{r} \frac{\partial}{\partial r} \left(r \frac{\partial C}{\partial r} \right) + \frac{D_T}{T_\infty} \frac{1}{r} \frac{\partial}{\partial r} \left(r \frac{\partial T}{\partial r} \right) \\ - k_r^2 (C - C_\infty) \left(\frac{T}{T_\infty} \right)^n \exp \left(-\frac{E_a}{k^* T} \right). \end{aligned} \quad (7.4)$$

The realistic BCs are

$$u = u_w(x, t), \quad v = 0, \quad T = T_w, \quad D_B \frac{\partial C}{\partial r} + \frac{D_T}{T_\infty} \frac{\partial T}{\partial r} = 0 \quad \text{at} \quad r = R, \quad (7.5)$$

$$u \rightarrow 0, \quad T \rightarrow T_\infty, \quad C \rightarrow C_\infty \quad \text{as} \quad r \rightarrow \infty. \quad (7.6)$$

Here (u, v) signifies the velocities along x - and r -directions and Q_0 the heat generation/absorption coefficient.

To solve the governing equations (7.1) – (7.4) subject to the corresponding boundary conditions (7.5) and (7.6), we make use of the following transformations and dimensionless quantities:

$$\eta = \frac{r^2 - R^2}{2R} \left(\frac{u_w}{\nu x} \right)^{1/2}, \quad \psi = (u_w \nu x)^{1/2} R f(\eta), \quad \theta(\eta) = \frac{T - T_\infty}{T_w - T_\infty}, \quad \phi(\eta) = \frac{C - C_\infty}{C_\infty}. \quad (7.7)$$

The stream function $\psi(r, x)$ is given by $u = \frac{1}{r} \frac{\partial \psi}{\partial r}$ and $v = -\frac{1}{r} \frac{\partial \psi}{\partial x}$, so that the continuity equation (7.1) is automatically satisfied.

Now, by adopting Eq. (7.7), the governing Eqs. (7.2) – (7.4) are transformed into a set of

dimensionless equations as:

$$(1 + 2\gamma_1\eta) [\beta^* + (1 - \beta^*)(1 - We f'')^{-2}] f''' + f f'' - A \left(f' + \frac{\eta}{2} f'' \right) - M^2 f' + 2\gamma_1 f'' \left[\beta^* + (1 - \beta^*) \left(1 - \frac{We f''}{2} \right) (1 - We f'')^{-2} \right] = 0, \quad (7.8)$$

$$(1 + 2\gamma_1\eta) \theta + 2\gamma_1 \theta' + Pr f \theta' + Pr (1 + 2\gamma_1\eta) (Nb \theta' \phi' + Nt \theta'^2) - Pr A \frac{\eta}{2} \theta' + Pr \delta \theta = 0, \quad (7.9)$$

$$(1 + 2\gamma_1\eta) \phi'' + 2\gamma_1 \phi' + Sc f \phi' + \frac{Nt}{Nb} [(1 + 2\gamma_1\eta) \theta'' + 2\gamma_1 \theta'] - Sc A \frac{\eta}{2} \phi' - Sc \sigma^* (1 + \delta^* \theta)^n \phi \exp \left(-\frac{E}{1 + \delta^* \theta} \right) = 0, \quad (7.10)$$

with

$$f(0) = 0, \quad f'(0) = 1, \quad \theta(0) = 1, \quad Nb \phi' + Nt \theta' = 0, \quad (7.11)$$

$$f'(\infty) \rightarrow 0, \quad \theta(\infty) \rightarrow 0, \quad \phi(\infty) \rightarrow 0. \quad (7.12)$$

Here, the local Weissenberg number We , curvature parameter γ , heat generation/absorption parameter δ , magnetic parameter M , thermophoresis parameter Nt , Brownian motion parameter Nb , Prandtl number Pr , Schmidt number Sc , unsteadiness parameter A , viscosity ratio parameter β^* , reaction rate parameter σ^* , activation energy parameter E and temperature difference parameter δ^* are defined as follows:

$$\begin{aligned}
We &= \left(\frac{a^3 x^2 r^2 \Gamma^2}{(1-ct)^3 R^2 \nu} \right)^{1/2}, \quad \gamma_1 = \left(\frac{\nu(1-ct)}{aR^2} \right)^{1/2}, \quad \delta = \frac{Q_0(1-ct)}{a(\rho c)_f}, \\
M &= \left(\frac{\sigma^* B_0^2}{\rho a} \right)^{1/2}, \quad Nt = \frac{\tau D_T (T_f - T_\infty)}{\nu T_\infty}, \quad Nb = \frac{\tau D_B C_\infty}{\nu}, \quad Pr = \frac{\mu c_p}{k}, \\
Sc &= \frac{\nu}{D_B}, \quad A = \frac{c}{a}, \quad \beta^* = \frac{\mu_\infty}{\mu_0}, \quad \sigma^* = \frac{k_r^2}{a}, \quad E = \frac{E_a}{kT_\infty}, \quad \delta^* = \frac{T_w - T_\infty}{T_\infty}. \quad (7.13)
\end{aligned}$$

7.1.1 Parameters of Physical Significance

The friction and heat transport coefficients are given by:

$$C_f = \frac{\tau_{rx}|_{r=R}}{\rho u_w^2}, \quad Nu = \frac{xq_w|_{r=R}}{k(T_f - T_\infty)}, \quad (7.14)$$

where

$$\tau_{rx} = \mu_0 \frac{\partial u}{\partial r} \left[\beta^* + (1 - \beta^*) \left(1 - \Gamma \frac{\partial u}{\partial r} \right)^{-1} \right], \quad q_w = -k \left(\frac{\partial T}{\partial r} \right). \quad (7.15)$$

The non-dimensional surface drag and heat transport rate takes the form:

$$\text{Re}^{1/2} C_f = f''(0) \left[\beta^* + (1 - \beta^*) (1 - We f''(0))^{-1} \right], \quad \text{Re}^{-1/2} Nu = -\theta'(0), \quad (7.16)$$

7.1.2 Computational Procedure

The system of highly non-linear ODEs with associated boundary conditions Eqs. (7.8) – (7.12) has been tackled numerically via RKF method coupled with Nachtsheim-Swigert shooting technique for the non-dimensional velocity, temperature and nanoparticle concentration distributions. The ruling equations are transformed into a system of first order ODEs and Runge-Kutta

method with shooting technique is utilized for step by step integration and calculations are carried out on MATLAB software. The computations are performed until some convergence criterion of 10^{-6} is fulfilled.

7.2 Results and Discussion

The numerical simulation of $f'(\eta)$, $\theta(\eta)$ and $\phi(\eta)$ for varying pertinent physical parameters have been performed in a MATLAB routine based on Runge-Kutta method. We investigate the physical behavior of all involved dimensionless parameters. For instance, unsteadiness parameter A , magnetic parameter M , local Weissenberg number We , curvature parameter γ_1 , heat generation/absorption parameter δ , Brownian motion parameter Nb , thermophoresis parameter Nt , Schmidt number Sc , activation energy parameter E , temperature difference parameter δ^* , reaction rate parameter σ^* and fitted rate constant n on $f'(\eta)$, $\theta(\eta)$ and $\phi(\eta)$, which are illustrated through **Figs. 7.2 – 7.14**. We have put default values for leading parameters such as $A = 0.1$, $M = 0.2$, $We = 1.0$, $\delta = 0.2$, $\beta^* = 0.1$, $\gamma_1 = 0.2$, $Nb = 0.5$, $Nt = 0.5$, $Sc = 5.0$, $E = 2.0$, $Pr = 7.0$, $\delta^* = 0.1$, $\sigma^* = 1.0$ and $n = 0.5$ during the entire computations.

7.2.1 Velocity and Temperature Profiles

The dimensionless velocity field for several values of γ_1 is displayed in **Fig. 7.2**. The computational values are plotted for two different cases of M i.e., hydrodynamic flow ($M = 0$) and hydromagnetic flow ($M = 1$). It can be viewed from **Fig. 7.2** that the velocity distribution inside the boundary-layer rises for higher γ_1 for both cases. This fact is justified physically because the higher values of γ_1 lead to reduce the cylinder radius. So a smaller amount of resistance is being offered by the surface and subsequently the fluid velocity increases. In addition,

the liquid velocity is reduced subject to a rise in M . Owing to the reality that presence of transverse magnetic field to an electrically conducting liquid ascend the retarding force, known as the Lorentz force and this force accelerates the movement of the fluid within the boundary layer region. We further inspected that the computed results are much notable after a certain distance from the solid surface. The impact of curvature parameter in the unsteady two-dimensional flow on $\theta(\eta)$ is well exhibited through **Fig. 7.3**. The graphs are sketched in the presence of magnetic field ($M = 1$) and absence of magnetic field ($M = 0$). It is witnessed that higher values of curvature parameter resulted in an increment in fluid temperature as well as the corresponding boundary-layer thickness. As expected, the $\theta(\eta)$ exhibit a significant growth due to magnetic field presence.

Fig. 7.4 is about the behavior of $\theta(\eta)$ with varying values of δ . The behavior of $\theta(\eta)$ is depicted for two cases of curvature parameter i.e., $\gamma_1 = 0$ and $\gamma_1 = 1$. Here, it is perceived that the $\theta(\eta)$ in case of $\gamma_1 = 1$ dominates over the flow by a flat plate and also the $\theta(\eta)$ increases significantly for higher estimations of heat generation/absorption parameter. Further, we noticed that all $\theta(\eta)$ curves start with no-slip boundary condition at 1 and meet the far-away boundary condition asymptotically. It is fascinating to mention that boundary-layer is attained quite earlier in case of $\gamma_1 = 0$. Now, we will elaborate the impact of Nt on $\theta(\eta)$ which has ample physical importance regarding fluid temperature. It is seen that the temperature distribution reveals magnification phenomenon and an improving values of Nt enhances the fluid temperature as seen through **Fig. 7.5**. This is due to the reason that temperature difference between surface and ambient fluid rises for larger Nt and hence the fluid temperature accelerates for both cases. Moreover, the fluid temperature has higher value in case of $\gamma_1 = 1$.

7.2.2 Nanoparticles Concentration Profiles

We now disclose the conduct of nanoparticles concentration for diverse physical parameters through **Figs. 7.6 – 7.11**. The behavior of the curvature parameter γ_1 in both the presence/absence of M on $\phi(\eta)$ is displayed in **Fig. 7.6**. It is interesting to note that all the concentration curves $\phi(\eta)$ are initiated from negative value fulfilling the boundary condition at the surface, reaches its peak value and then tends to zero asymptotically. This figure demonstrates that the concentration distributions increases for higher values of curvature parameter in both cases. Clearly, concentration field heightens with enlarging M . **Fig. 7.7** depicts the concentration curves $\phi(\eta)$ for distinct values of Nb for $M = 1$ and $M = 0$. For both the cases, it is scrutinized that the concentration profiles have dual behavior with larger Brownian motion parameter. A useful insight of this figure discloses that the concentration profiles change their behavior near $\eta \approx 0.38$ i.e., within the region $0 \leq \eta \lesssim 0.38$, the concentration profiles rise with augmenting values of Nb while for the region $0.38 \lesssim \eta \leq 8$, it has decreasing behavior. The significance of thermophoresis parameter Nt against concentration profiles is presented in **Fig. 7.8**. Initially, these profiles increases with inside the boundary layer, reaches up to maximum value and then goes on decreasing monotonically to satisfy the boundary condition. Also, for enlarged Nt , near the solid boundary, the concentration profile decrease and after a definite distance it goes on increasing for both the cases. It is appealing to note that the peak in the nanoparticles concentration close to the sheet is because of the fact that the nanoparticle volume fraction close to the sheet is higher in comparison to nanoparticles volume fraction at the surface.

The simulated concentration profiles $\phi(\eta)$ for various δ^* are drawn in **Fig. 7.9** in the

absence/presence of M . The concentration curves shown in this figure perceived to have a decaying behavior with higher δ^* . Additionally, for $M = 0$, the δ^* is higher in comparison with the influence of magnetic field. **Fig. 7.10** elucidates the behavior of $\phi(\eta)$ with the variation in σ^* . From this plot, it is seen that an increase in the destructive chemical reaction parameter $\sigma^* > 0$ tends to reduce the nanoparticles concentration. Influence of E on $\phi(\eta)$ is illustrated in **Fig. 7.11**. In chemistry, the term ‘activation energy’ was first introduced by a Swedish scientist Svante Arrhenius which is described as the energy that must be used to proceed the chemical reaction. It is also be defined as the minimum amount of energy that is require to continue a chemical reaction. It is generally denoted by E_a and given in units of $kJ \cdot mol^{-1}$. The modified Arrhenius function $\left(\frac{T}{T_\infty}\right)^n \exp\left(-\frac{E_a}{kT}\right)$ declines as activation energy E_a amplifies. We observe that increasing the values of activation energy E leads to enhance the nanoparticles concentration. In **Fig. 7.12**, the variation of fitted rate constant n on nanoparticles concentration is shown. The $\phi(\eta)$ and thickness of associated boundary layer enhance as fitted rate constant changes its values from $n = 2$ to 8.

7.2.3 Skin friction and Nusselt number

The simulated values of $Re^{1/2} C_f$ and $Re^{-1/2} Nu$ are obtained for distinct values of pertinent parameters and presented through **Fig. 7.13** and **Fig. 7.14**. The variation in $Re^{1/2} C_f$ against M for varying We is shown in **Fig. 7.13**. A significant rise in $Re^{1/2} C_f$ is marked for higher We which means that the wall shear stress is higher for larger We . In **Fig. 7.14**, we exhibit $-\theta'(0)$ against the Nt for deviating values of σ^* . As the surface heat flux has an inverse relation with σ^* and as a result the heat transfer rate decreases for greater σ^* . Further, the temperature gradient collapse in non-linear pattern when Nt is increased.

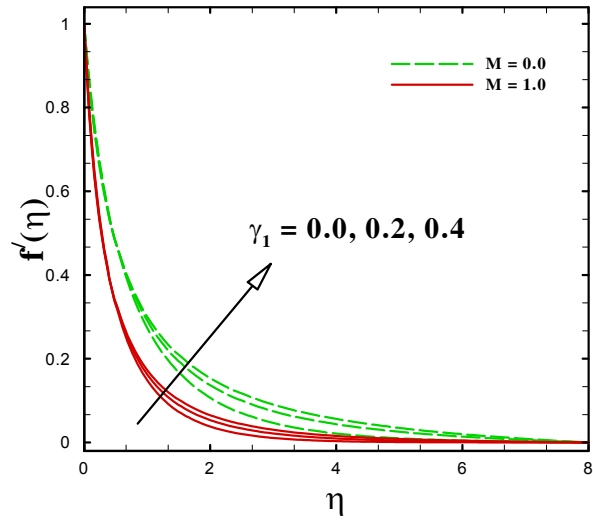


Fig. 7.2: Illustration of $f'(\eta)$ for varying γ_1 .

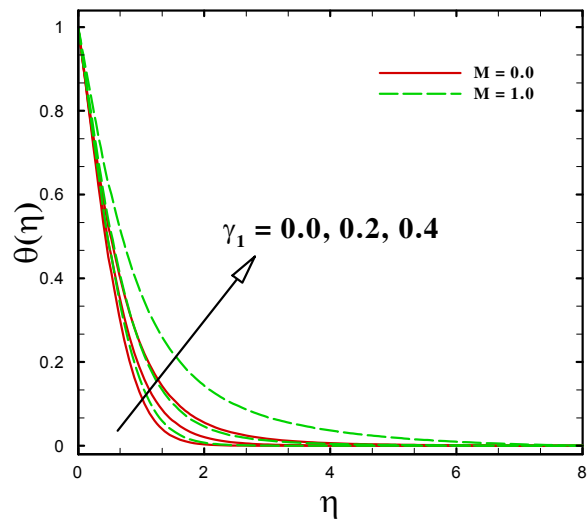


Fig. 7.3: Illustration of $\theta(\eta)$ for varying γ_1 .

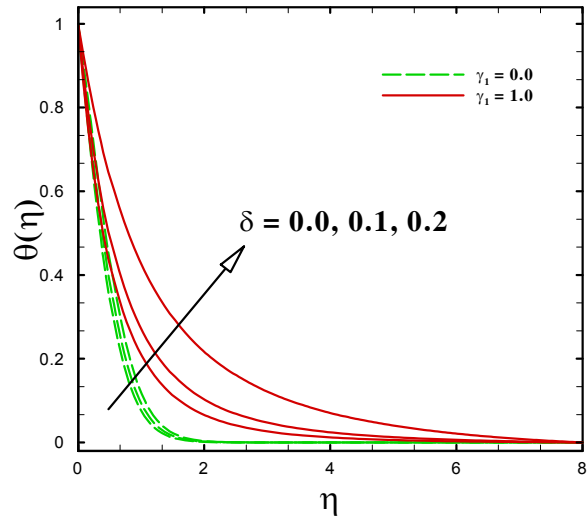


Fig. 7.4: Illustration of $\theta(\eta)$ for varying δ .

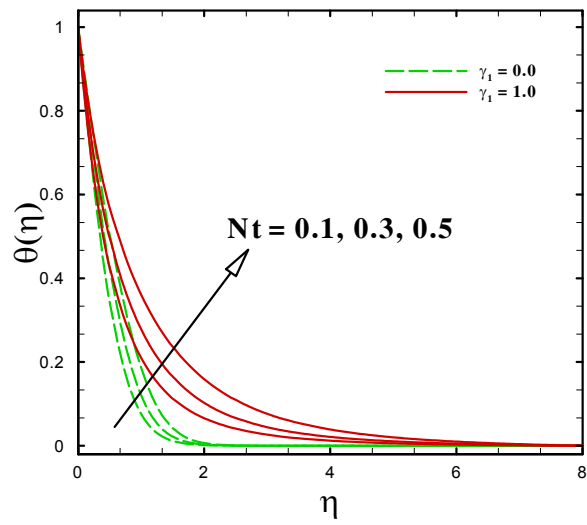


Fig. 7.5: Illustration of $\theta(\eta)$ for varying Nt .

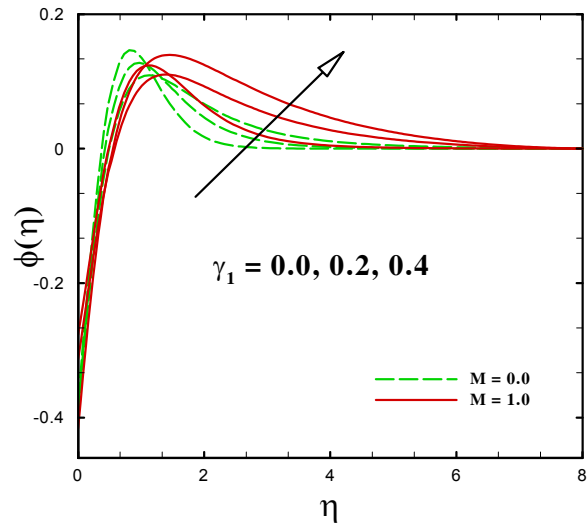


Fig. 7.6: Illustration of $\phi(\eta)$ for varying γ_1 .

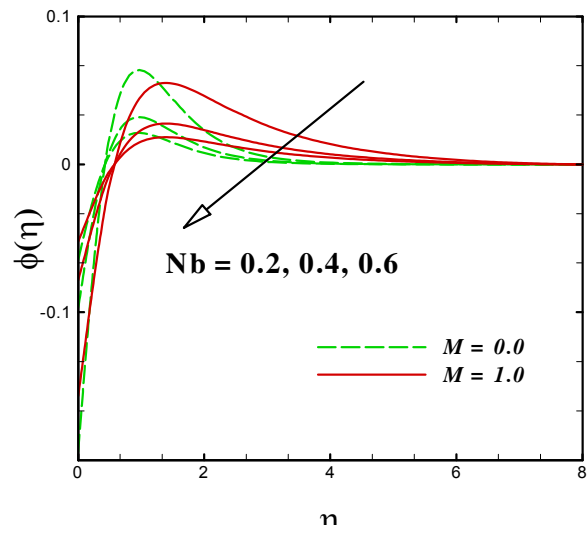


Fig. 7.7: Illustration of $\phi(\eta)$ for varying Nb .

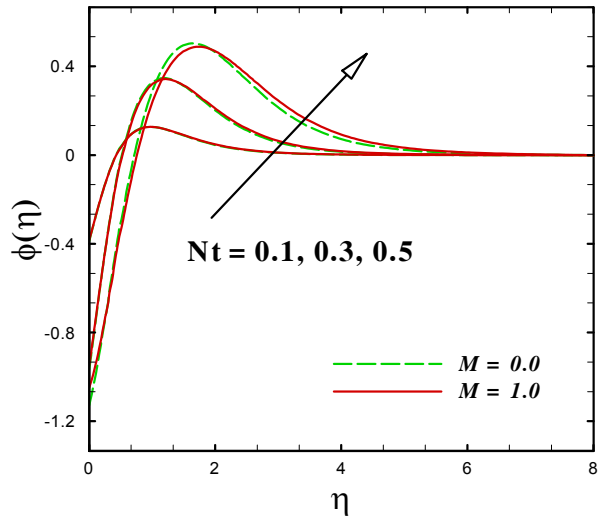


Fig. 7.8: Illustration of $\phi(\eta)$ for varying Nt .

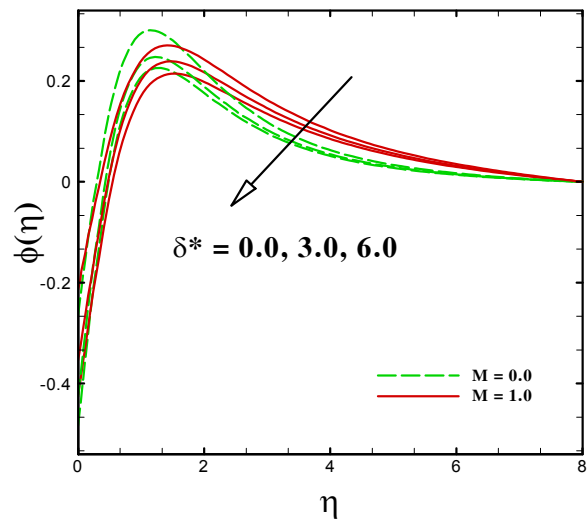


Fig. 7.9: Illustration of $\phi(\eta)$ for varying δ^* .

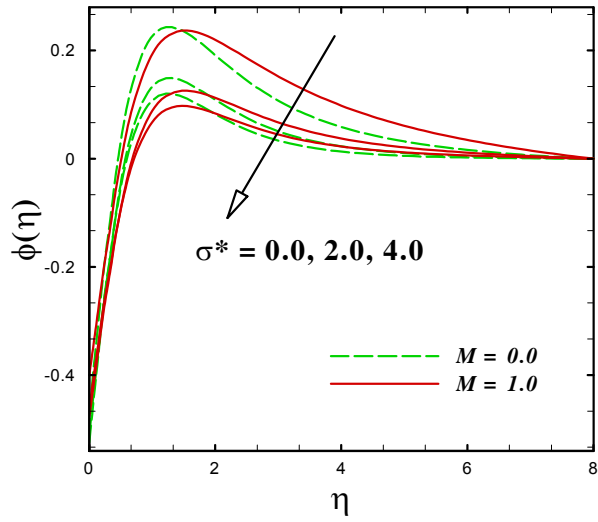


Fig. 7.10: Illustration of $\phi(\eta)$ for varying σ^* .

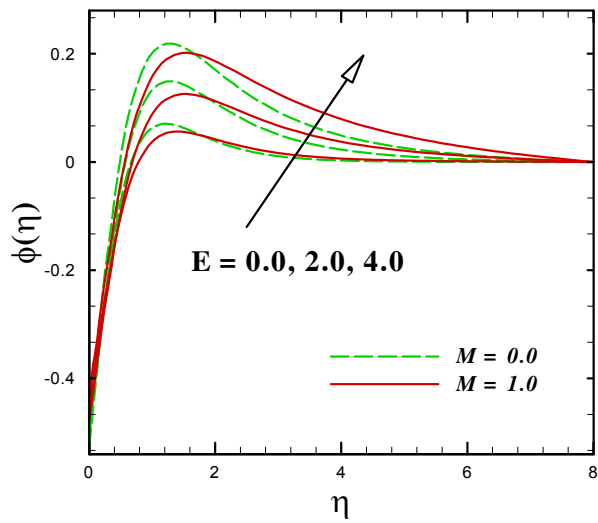


Fig. 7.11: Illustration of $\phi(\eta)$ for varying E .

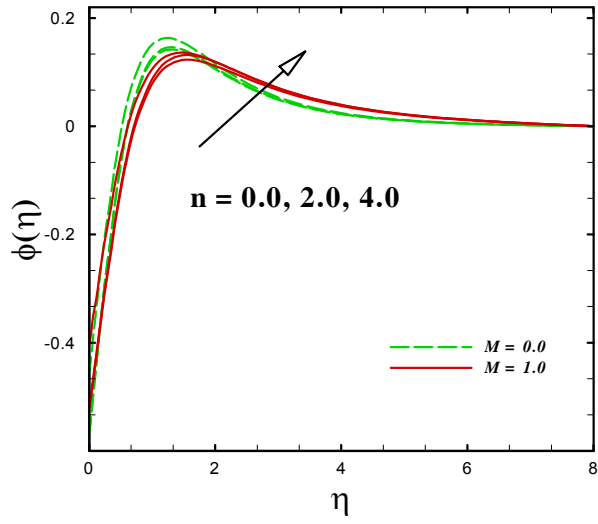


Fig. 7.12: Illustration of $\phi(\eta)$ for varying n .

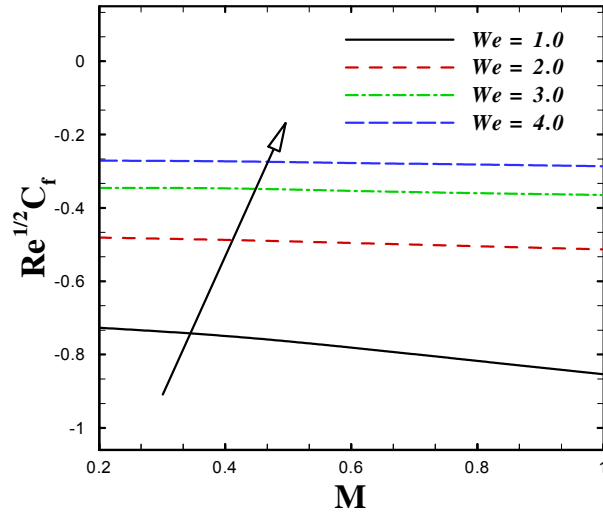


Fig. 7.13: Illustration of $Re^{1/2} C_f$ for varying We .

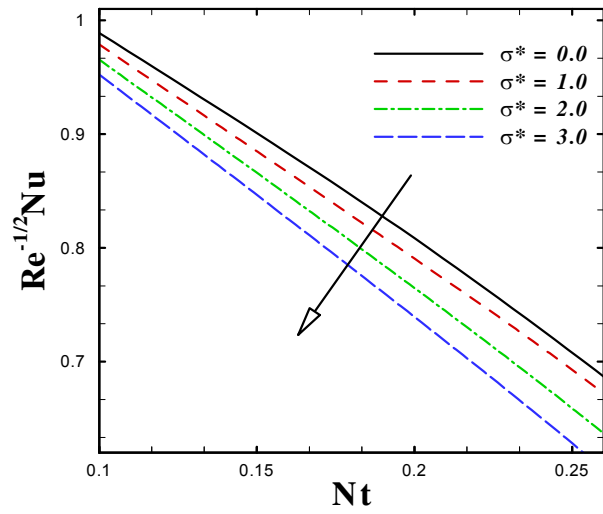


Fig. 7.14: Illustration of $Re^{-1/2} Nu$ for varying σ^* .

Chapter 8

Williamson Fluid Flow driven by Shrinking Surface

This chapter deals with multiple solutions for an electrically conducting Williamson fluid flow caused by a stretching/shrinking surface by considering Ohmic heating and viscous dissipation. Flow is subjected to a time-dependent magnetic field which is employed in transverse direction. The dimensionless variables are used to transform the governing PDEs into ODEs and then tackled numerically. In addition, the multiple solutions for dimensionless fluid velocity and temperature distribution are captured when a certain quantity of mass suction is employed through the porous shrinking surface. It is visualized from multiple branches that the skin friction enhances with magnetic parameter for the upper branch solution and it reduces for lower branch solution.

8.1 Problem Description

Assuming transient, 2D, incompressible and laminar flow of magneto-Williamson fluid induced by a permeable shrinking surface in the vicinity of stagnation point. The physical model is depicted in **Fig. 8.1**. It is considered that the stretching/shrinking sheet velocity is $u_w = \chi u_w(x, t)$, where χ is a constant with $\chi < 0$ relates to a shrinking sheet and $\chi > 0$ represents a stretching sheet and the velocity of the far flow (inviscid flow) is $u_e(x, t)$. It is illustrated that the sheet is permeable and the mass flux velocity is $v_w(x, t)$. The surface temperature $T_w(x, t)$ along with ambient temperature T_∞ are considered as constants.

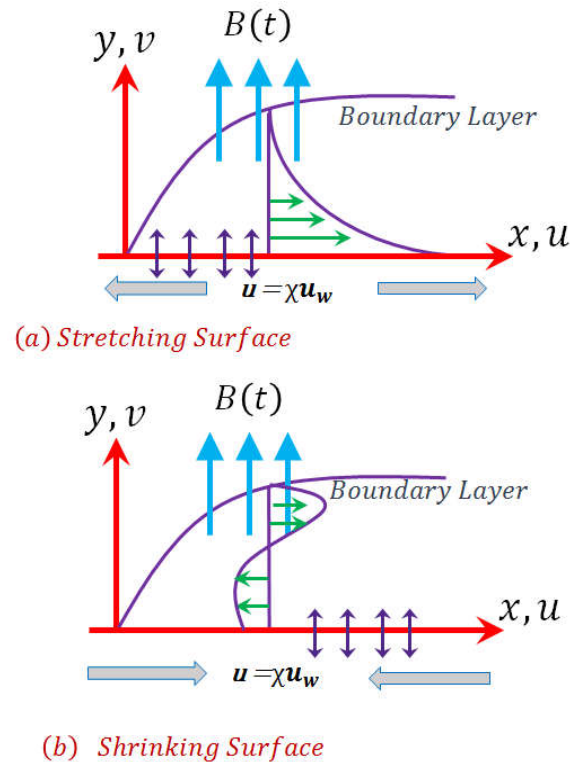


Fig. 8.1: Schematic diagram.

The equations of motion that govern the unsteady flow of Williamson fluid can be written

as:

$$\frac{\partial u}{\partial x} + \frac{\partial v}{\partial y} = 0, \quad (8.1)$$

$$\begin{aligned} \frac{\partial u}{\partial t} + u \frac{\partial u}{\partial x} + v \frac{\partial u}{\partial y} &= \frac{\partial u_e}{\partial t} + \frac{\partial u_e}{\partial x} + \nu \frac{\partial^2 u}{\partial y^2} \left[\beta^* + (1 - \beta^*) \left(1 - \Gamma \frac{\partial u}{\partial y} \right)^{-1} \right] \\ &\quad - \frac{\sigma B^2(t)}{\rho} (u_e - u) + \nu \Gamma \left(\frac{\partial u}{\partial y} \right) \left(\frac{\partial^2 u}{\partial y^2} \right) \left[(1 - \beta^*) \left(1 - \Gamma \frac{\partial u}{\partial y} \right)^{-2} \right], \end{aligned} \quad (8.2)$$

$$\begin{aligned} \frac{\partial T}{\partial t} + u \frac{\partial T}{\partial x} + v \frac{\partial T}{\partial y} &= \alpha \frac{\partial^2 T}{\partial y^2} + \frac{\nu}{C_p} \left[\beta^* \left(\frac{\partial u}{\partial y} \right)^2 + (1 - \beta^*) \left(1 - \Gamma \frac{\partial u}{\partial y} \right)^{-1} \left(\frac{\partial u}{\partial y} \right)^2 \right] \\ &\quad + \frac{\sigma B^2}{\rho C_p} (u_e - u)^2, \end{aligned} \quad (8.3)$$

with physical boundary conditions:

$$\begin{aligned} t < 0 : \quad u = v = 0, \quad T = T_\infty \text{ for any } x, y \\ t \geq 0 : \quad u = \lambda u_w(x, t), \quad v = v_w(x, t) \quad T = T_w(x, t) \quad \text{at} \quad y = 0, \\ u \rightarrow u_e(x, t), \quad T \rightarrow T_\infty \quad \text{as} \quad y \rightarrow \infty. \end{aligned} \quad (8.4)$$

We assume the following forms of u_w , u_e , v_w , T_w and $B(t)$:

$$\begin{aligned} u_w(x, t) &= \frac{\alpha x}{1 - \beta t}, \quad u_e(x, t) = \frac{\alpha x}{1 - \beta t}, \quad v_w(x, t) = -\frac{v_0}{\sqrt{1 - \beta t}}, \\ T_w(x, t) &= T_\infty + \frac{bx^2}{(1 - \beta t)^2}, \quad B^2(t) = \frac{B_0^2}{1 - \beta t}, \end{aligned} \quad (8.5)$$

where α , b and β are constants having the dimension $(\text{time})^{-1}$.

Now the necessary non-dimensional variables are

$$\eta = y\sqrt{\frac{\alpha}{\nu(1-\beta t)}}, \quad \psi(x, y, t) = \sqrt{\frac{\nu\alpha}{1-\beta t}}xf(\eta), \quad \theta(\eta) = \frac{T - T_\infty}{T_w - T_\infty}. \quad (8.6)$$

Substituting Eq. (8.6) into Eqs. (8.3) – (8.5), we obtain

$$\left[\beta^* + (10 - \beta^*) (1 - We f'')^{-2}\right] f''' + f f'' + 1 - (f')^2 - A \left(f' - 1 + \frac{\eta}{2} f''\right) + M(1 - f') = 0, \quad (8.7)$$

$$\begin{aligned} \theta'' + Pr (f\theta' - 2f'\theta) - Pr A \left(\frac{1}{2}\eta\theta' + 2\theta\right) + Pr Ec[M(1 - f')^2 \\ + \beta^* f''^2 + (1 - \beta^*) (1 - We f'')^{-1} f''^2] = 0, \end{aligned} \quad (8.8)$$

with associated boundary conditions:

$$f(0) = s, \quad f'(0) = \chi, \quad \theta(0) = 1 \quad \text{at} \quad \eta = 0, \quad (8.9)$$

$$f'(\infty) = 1, \quad \theta(\infty) = 0 \quad \text{as} \quad \eta \rightarrow \infty. \quad (8.10)$$

The emerging physical parameters that appeared in the above equations are:

$$We = \sqrt{\frac{\Gamma^2 u_w^3}{\nu x}}, \quad A = \frac{\beta}{\alpha}, \quad M = \frac{\sigma B_0^2}{\rho \alpha}, \quad s = \frac{-v_0}{\sqrt{\nu \alpha}}, \quad Ec = \frac{u_w^2}{C_p(T_w - T_\infty)}, \quad (8.11)$$

where We , A , M , s , Ec denote the local Weissenberg number, unsteadiness parameter, magnetic parameter, mass transfer parameter and the Eckert number, respectively.

8.1.1 Engineering Coefficients

The quantities regarding engineering significance are coefficient of skin friction (C_f) and Nusselt number (Nu_x) are defined by the relations:

$$C_f = \frac{v(1 - \beta t)^{-1/2}}{u_w^2} \left(\frac{\partial u}{\partial y} \right)_{y=0}, \quad Nu_x = \frac{x(1 - \beta t)^{1/2}}{(T_w - T_\infty)} \left(\frac{\partial T}{\partial y} \right)_{y=0}, \quad (8.12)$$

with

$$\tau_w = \mu_0 \frac{\partial u}{\partial y} \left[\beta^* + (1 - \beta^*) \left(1 - \Gamma \frac{\partial u}{\partial y} \right)^{-1} \right]. \quad (8.13)$$

Making use of Eq. (8.6), we obtain

$$\text{Re}^{1/2} C_f = f''(0) [\beta^* + (1 - \beta^*) \{1 - \text{We} f''(0)\}^{-1}], \quad \text{Re}^{-1/2} Nu = -\theta'(0). \quad (8.14)$$

8.2 Numerical Methodology

The nonlinear differential Eqs. (8.7) and (8.10) are elucidated numerically using the RKF method.

Let

$$\left. \begin{aligned} f' &= p \\ p' &= q \\ q' &= \frac{p^2 - fq - 1 + A(p - 1 + \frac{2}{3}q) - M(1 - p)}{\beta^* + (1 - \beta^*)(1 - \text{We}q)^{-2}} \end{aligned} \right\} \quad (8.15)$$

and

$$\left. \begin{aligned} \theta' &= l \\ l' &= -\text{Pr} fl + 2\text{Pr} p\theta + \text{Pr} A (2\theta + \frac{q}{2}l) \\ -Ec\text{Pr} &\left[M(1-p)^2 + \beta^* q^2 + (1-\beta^*)(1-Weq)^{-1} q^2 \right] \end{aligned} \right\} \quad (8.16)$$

with boundary conditions

$$f(0) = s, \quad Xp(0) = \chi, \quad \theta(0) = 1, \quad p(\infty) \rightarrow 1 \quad \theta(\infty) \rightarrow 0. \quad (8.17)$$

In order to integrate Eqs. (8.15) and (8.16) with (8.17) as an IVP, the estimations for $q(0)$ *i.e.*, $f''(0)$ and $l(0)$ *i.e.*, $\theta'(0)$ are not mentioned at this stage. The initial guess values for $f''(0)$ and $\theta'(0)$ are selected and then RKF 45 method is employed to get an approximate solution. Then the obtained values for $f'(\eta)$ and $\theta(\eta)$ at η_∞ varying from 5 to 15 depending on the physical parameters are compared with the far field boundary conditions $f'(\eta_\infty) = 1$ and $\theta(\eta_\infty) = 0$, and the values of $f''(0)$ and $\theta'(0)$ are modified using "Newton Raphson method" to determine the required significant digit. Hence the step size is chosen as $\Delta\eta = 0.001$ and the solution process is repeated until the desired outcomes are converged up to the error tolerance of 10^{-6} .

8.2.1 Validation of Numerical Data

To evaluate the accuracy of employed numerical scheme, **Tables 8.1** and **8.2** present a comparison of $f''(0)$ and $-\theta'(0)$ for varying values of M and χ with those of Wang [105] and Soid *et al.* [106]. These comparisons are given quantitatively in **Tables 8.1** and **8.2**, and revealed in a good agreement. From both tables a conspicuous perception could be made that computed outcomes are in decent agreement with published data. Now, we have the confidence to say

that the numerical scheme produces correct results.

8.3 Computational Results

In the current work, numerical simulations for the heat transfer subject to Ohmic heating and dissipation aspects in stagnation-point flow of time-dependent Williamson liquid are developed. The computations for varying values of the suction parameter s , viscosity ratio parameter β^* , magnetic parameter M , Weissenberg number We and unsteadiness parameter A have been presented. To conserve space we choose to plot the profiles of velocity, temperature, wall shear stress and heat transport rate for the case of $We = 3.0$, $\beta^* = 0.1$, $\chi = -1.3$, $s = 1.0$, $Pr = 1.0$, $M = 0.1$, $A = 0.1$ and $Ec = 0.5$ only to show the existence of dual solutions in the profiles. The results obtain in this study are illustrated through **Figs. 8.2 – 8.11**. Since, when we assume the stagnation region towards a shrinking surface there may exist dual solutions in a certain range of governing parameters, where the sheet is being shrunk. First solution is illustrated by solid lines whereas second solution is portrayed by dotted lines. The edge of the boundary layer has been chosen $\eta_\infty = 10$ for the first solution and $\eta_\infty = 20$ for the second solution.

The computed data of $Re^{1/2} C_f$ and $Re^{-1/2} Nu$ is written in **Table 8.3**. Clearly, increasing values of We strengthen the $Re^{1/2} C_f$ in first solution while reverse characteristics are observed for second solution. **Table 8.3** also depicts the variation of $Re^{-1/2} Nu$ for distinct values of We and β^* . Here, heat transportation rate is lower with the growth of We in the upper solution whereas a reverse pattern is seen for lower solution. Further, the higher values of β^* lead to increase the $Re^{-1/2} Nu$ in the first solution. It is also noticed that the $Re^{-1/2} Nu$ is a decreasing function of β^* in the second solution.

In **Fig. 8.2**, two solutions being developed for $\text{Re}^{1/2} C_f$ against higher values of M . Further, critical values of s , when solution being divided into two branches (lower and upper branch solutions), are $s_c \approx -0.4499, -0.7731, -1.1188$. In this plot, the variation of $\text{Re}^{1/2} C_f$ with $s < 0$ (blowing case), $s > 0$ (suction case) and $s = 0$ (absence of suction/blowing) for several values of M is shown. It is revealed from **Fig. 8.2**, that the wall shear stress rises with enlarged values of M for the first solution while for the second solution it deprecates with larger M . **Fig. 8.3** elaborates the performance of $\text{Re}^{1/2} C_f$ with χ for varying A . It is seen in **Fig. 8.3** that there are dual solutions for $\chi_c < \chi < 0$, where the critical values of χ are $\chi_c \approx -1.4972, -1.5241, -1.5522$. It can be seen that dual nature of solution exists for shrinking situation ($\chi < 0$), whereas the solution is unique for stretching situation ($\chi > 0$). It is further observed χ_c declines as A increases. Moreover, if the unsteadiness A is increased then $\text{Re}^{1/2} C_f$ also rises for first solution while for second solution a conflicting nature is observed. **Fig. 8.4** interprets the variation of rate of heat transfer with $\chi < 0$ (shrinking sheet) and $\chi > 0$ (stretching sheet) for different values of A ($A = 0.0, 0.05, 0.1$). This plot reveals that an increment in A the heat transfer rate enhances in both branches. The associated critical values corresponding to χ are $\chi_c \approx -1.4972, -1.5241, -1.5522$. Variation of $\text{Re}^{1/2} C_f$ against λ for β^* is portrayed in **Fig. 8.5**. This figure reveals that $\text{Re}^{1/2} C_f$ diminishes with the growth of β^* in the lower branch solution and opposite impact is noticed for upper branch solution. The trajectories of $\text{Re}^{-1/2} Nu$ for varying values of β^* are depicted through **Fig. 8.6** against χ . The range of χ , for which these dual nature solution exists, illustrate an increasing trend for higher values of β^* . The critical values of shrinking parameter λ_c varies from -1.5566 to -1.5692 as β^* changes from 0.3 to 0.7 . **Fig. 8.7** is presented to look at the influence of s on $f'(\eta)$. One can easily observed from this profile that dual solutions exists for certain values

of s . The fluid velocity improves with growing values of suction parameter s in case of upper branch solution, whereas the fluid velocity initially decreases with s and after that for large η , changing the nature it increases with s in the lower branch solution. Further, it is evident to say that in every case of dual solutions of the velocity profile, the thickness of momentum boundary layer for the second solution is higher in comparison to first solution. In **Fig. 8.8**, the features of s versus temperature profile are exhibited. The dual temperature profiles show that the temperature of the fluid rises with increasing suction parameter s in both solutions. The values of s varies from -0.75 to -0.73 , represent the blowing case in which $s < 0$. One can conclude from this graph that the fluid temperature as well as thickness of thermal boundary layer for both cases intensifies by higher suction parameter ($s < 0$). Moreover, the momentum boundary layer in the second solution is thicker in comparison to the first solution. From this, one can conclude that solutions for lower branch are not stable whereas the upper branch solutions are stable. The $f'(\eta)$ for varying A is shown in **Fig. 8.9**. Clearly, velocity is decreased for varying values of A for both lower and upper solution. Further, it is witnessed that second solution is much thicker than the first solution. **Fig. 8.10** shows velocity field for varying estimations of β^* . It is examined that both the upper and lower branch solutions increase for larger values of viscosity ratio parameter. This plot reveals that initially the fluid velocity decreases, while at a certain range of η the velocity profile improves remarkably. **Fig. 8.11** depicts the aspect of We on $f'(\eta)$. Fluid velocity is found to decrease with increase in We . It is noticed that the velocity corresponding to the first solution shows a similar trend to that of the second solution and it is found to be higher than those of the first solution for all values of We .

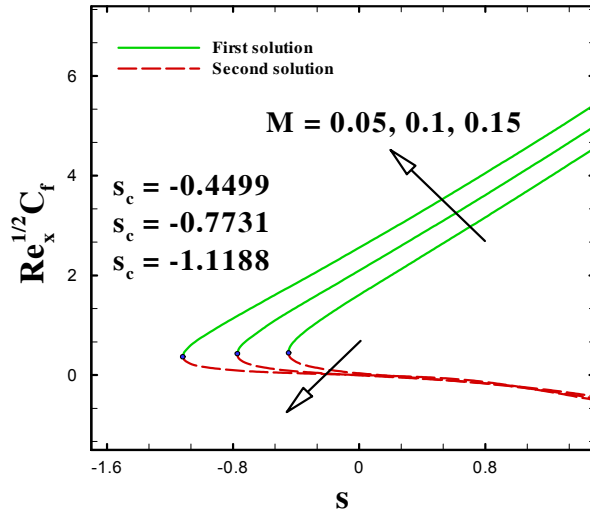


Fig. 8.2: Effect of M on $\text{Re}^{1/2} C_f$.

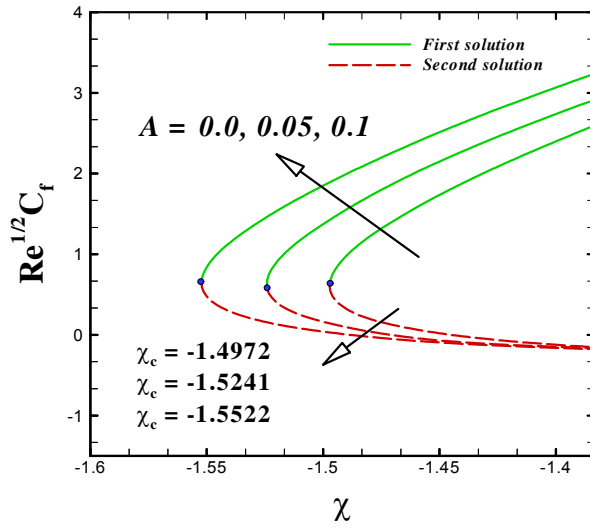


Fig. 8.3: Effect of A on $\text{Re}^{1/2} C_f$.

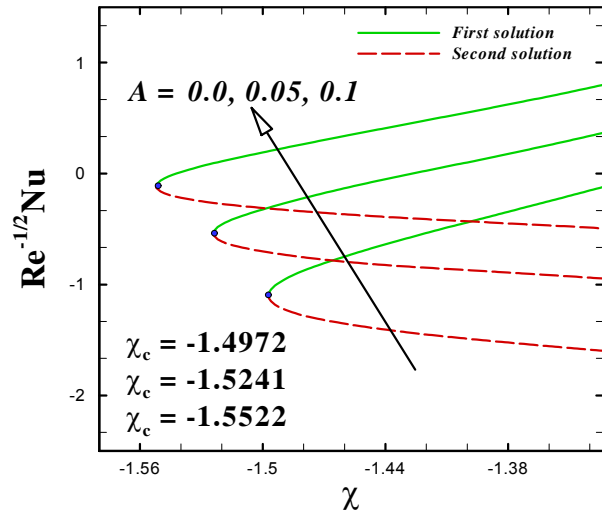


Fig. 8.4: Effect of A on $\text{Re}^{-1/2} Nu$.

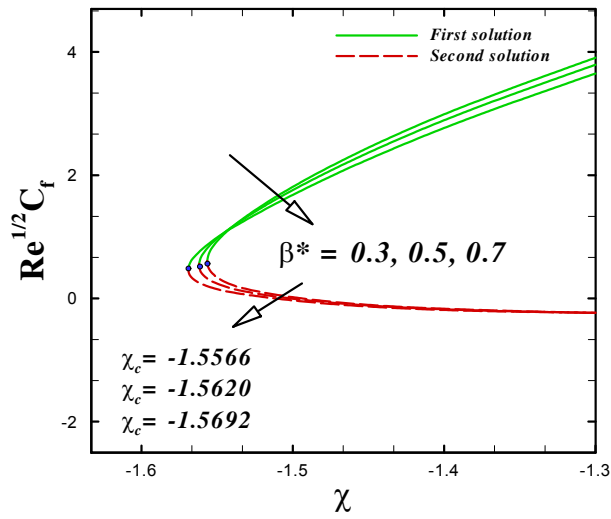


Fig. 8.5: Effect of β^* on $\text{Re}^{1/2} C_f$.

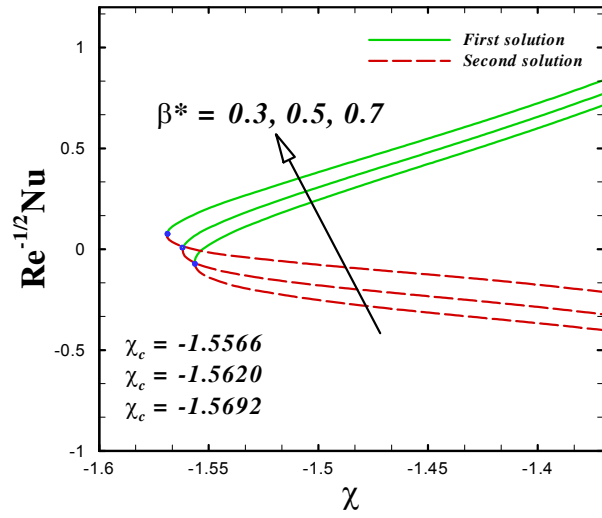


Fig. 8.6: Effect of β^* on $\text{Re}^{-1/2}Nu$.

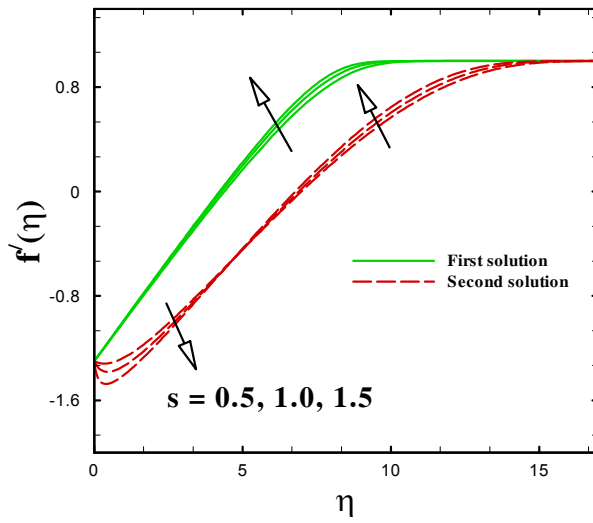


Fig. 8.7: $f'(\eta)$ for several values of s .

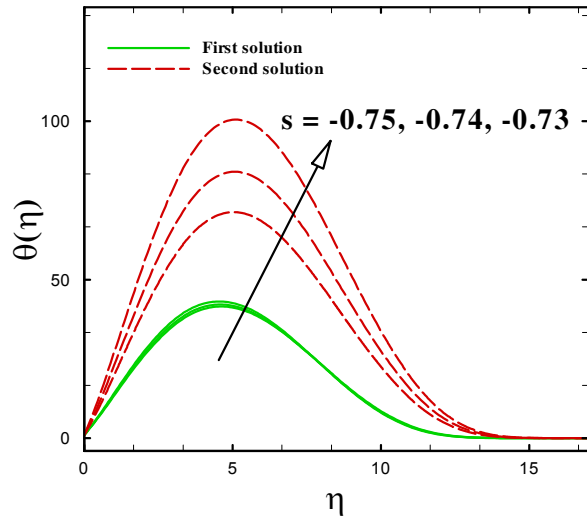


Fig. 8.8: $\theta(\eta)$ for several values of s .

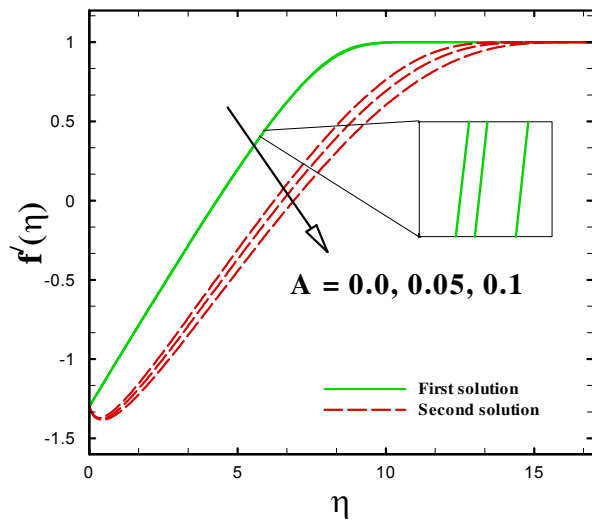


Fig. 8.9: $f'(\eta)$ for several values of A .

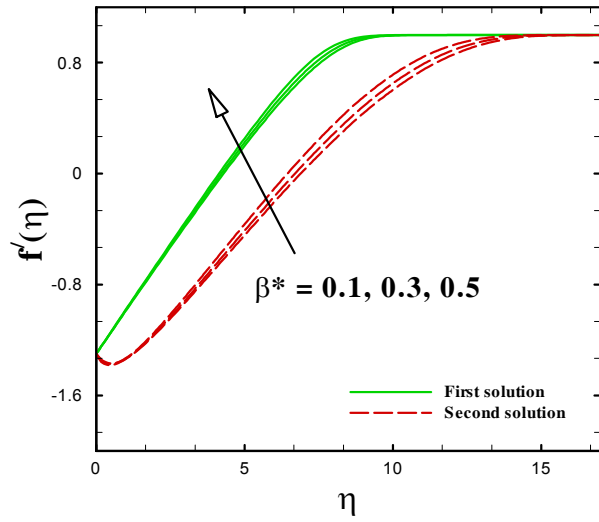


Fig. 8.10: $f'(\eta)$ for several values of β^* .

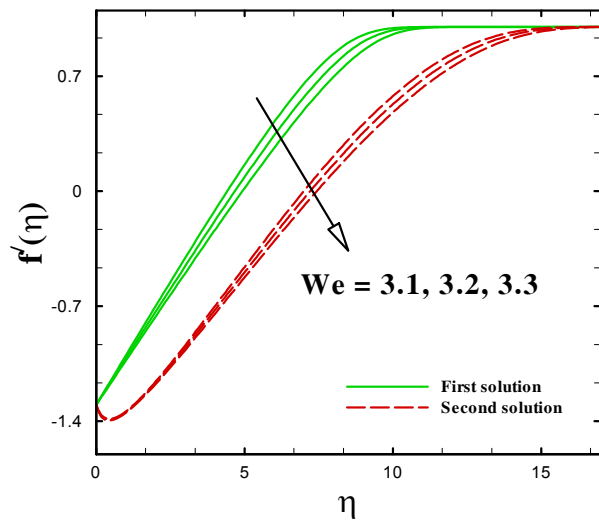


Fig. 8.11: $f'(\eta)$ for several values of We .

Table 8.1: A comparison of $\text{Re}^{1/2} C_f$ for $A = 0.0$, $Ec = 1.0$, $\text{Pr} = 1.0$, $We = 0.0$, $\beta^* = 0.0$ and $s = 0.0$.

Upper solution () and lower solution [] .

M	λ	Wang		[105]		Soid <i>et al.</i>		[106]		Present		study	
		()	[]	()	[]	()	[]	()	[]	()	[]	()	[]
0	0					1.23258765				1.2325854			
	-0.5	1.49567				1.49566976				1.4956667			
	-1.15	1.08223	0.11670			1.08223117	0.11670214			1.0822298	0.11670213		
	-1.2					0.93247335	0.23364973			0.93247131	0.23364972		
	-1.24657					0.57452574	0.56398927			0.57451987	0.56400733		
0.05	1									0			
	0.5									0.72188364			
	0					1.25253676				1.252533			
	-0.5					1.53308133				1.5330776			
	-1.29					0.62952288	0.54290217			0.62951133	0.54290214		
	-1.2906					0.59713221	0.57494863			0.59712483	0.5749298		
	-1.29064					0.58849210	0.58356583			0.58846158	0.5835657		

Table 8.2: A comparison of $\text{Re}^{-1/2} Nu$ for $A = 0.1$, $Ec = 1$, $\text{Pr} = 1$, $We = 0$, $\beta^* = 0$ and $s = 0$.

M	χ	Soid <i>et al.</i>	[106]	Present	study
		First solution	Second solution	First solution	Second solution
0.1	1	1.64764430		1.6476415	
	0.5	1.64764430		1.2308236	
	0	1.23082763		0.52573067	
	-0.5	-0.41366075		-0.41365927	
	-1.4	-5.15777141	-7.50772285	-5.1577797	-7.5077223
	-1.401	-5.43163891	-6.92183393	-5.4316397	-6.9218344
	-1.4017	-5.88601576	-6.26069817	-5.886029	-6.2608658
	-1.401774	-5.98573932	-6.14943330	-5.9855983	-6.1494436

Table 8.3: Skin friction coefficient and heat transfer coefficient for $A = 0.1$, $Ec = 0.5$, $Pr = 1.0$, $\chi = -1.3$, $M = 0.1$ and $s = 1.0$.

We	β^*	$Re^{1/2} C_f$		$Re^{-1/2} Nu$	
		First solution	Second solution	First solution	Second solution
3.0	0.1	4.00142	-0.238608	0.943479	-0.53743
3.1		4.02985	-0.242479	0.843177	-0.558032
3.2		4.05831	-0.246062	0.751221	-0.578591
3.3		4.08681	-0.249364	0.666442	0.59908
	0.2	4.03935	-0.248459	0.685843	-0.578345
	0.3	3.98833	-0.248128	0.706342	-0.553149
	0.4	3.93299	-0.248106	0.72804	-0.523119

Chapter 9

Thermal Radiation Impact on Williamson Nanofluid Flow induced by an Expanding/Contracting Cylinder

In this chapter, numerical results for the transient flow of Williamson nanofluid generated by an expanding/contracting circular cylinder are investigated. This critical review further explores the impact of variable magnetic field, thermal radiation, velocity slip and convective boundary conditions. The non-dimensional form of partially coupled ordinary differential equations are solved numerically by utilizing versatile Runge-Kutta integration scheme. The momentum, thermal and concentration characteristics are investigated with respect to diverse active parameters, like, Weissenberg number, unsteadiness parameter, viscosity ratio parameter, slip parameter, suction parameter, magnetic parameter, thermophoresis

parameter, Brownian motion parameter, Prandtl number, Lewis number and Biot number. The outcomes of the systematic review of these parameters and forecast plots are illustrated. The study reveals that multiple solutions for the considered problem exist for diverse physical parameters. The computed results indicate that the skin friction and heat transfer coefficients are significantly raised by the magnetic parameter for upper branch solution.

9.1 Problem Statement

We modeled transient flow of Williamson nanofluid caused by an expanding/contracting cylinder. The geometrical view of the considered physical model is illustrated in **Fig. 9.1**. It is assumed that cylinder diameter depends on time i.e., $a(t) = a_0\sqrt{1 - \beta t}$, where a_0 is the positive constant, t is the time and β is the expansion/contraction strength constant. A strength of magnetic field $B(t) = \frac{B_0}{\sqrt{1 - \beta t}}$ is operated in r -direction. The cylindrical surface is heated by convection through a hot liquid with temperature T_f and coefficient of heat transfer h_f .

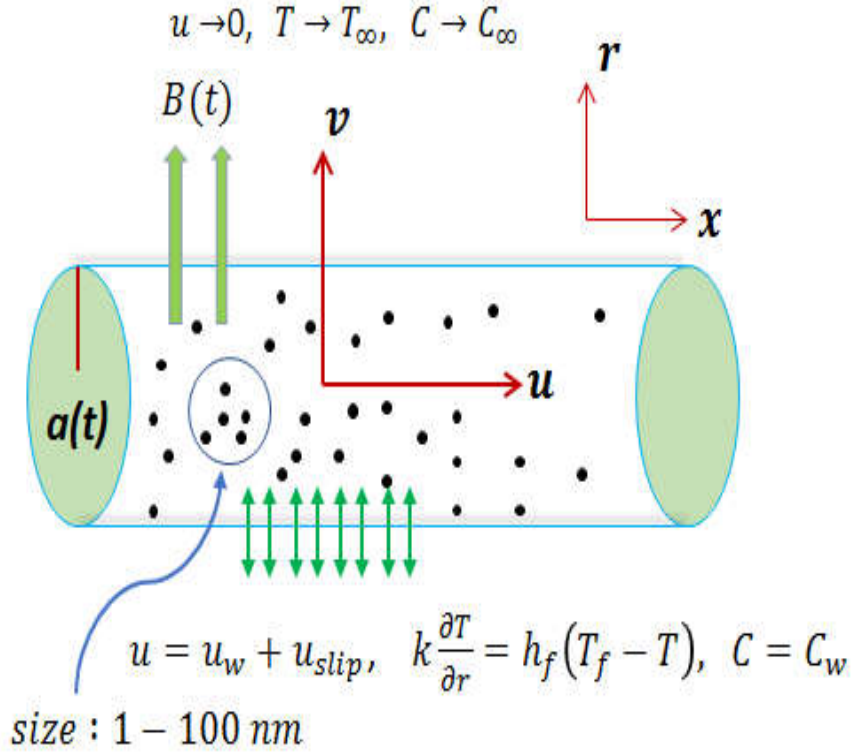


Fig. 9.1: Schematic diagram of considered problem.

According to above mentioned assumptions, the leading equations for Williamson nanofluids flow are given by:

Continuity equation:

$$\frac{\partial (ru)}{\partial x} + \frac{\partial (rv)}{\partial r} = 0, \quad (9.1)$$

Momentum equation:

$$\begin{aligned}
\frac{\partial u}{\partial t} + u \frac{\partial u}{\partial x} + v \frac{\partial u}{\partial r} &= \frac{\nu}{r} \frac{\partial u}{\partial r} \left[\beta^* + (1 - \beta^*) \left(1 - \Gamma \frac{\partial u}{\partial r} \right)^{-1} \right] \\
&\quad + \nu \Gamma \frac{\partial u}{\partial r} \frac{\partial^2 u}{\partial r^2} \left[(1 - \beta^*) \left(1 - \Gamma \frac{\partial u}{\partial r} \right)^{-2} \right] \\
+ \nu \frac{\partial^2 u}{\partial r^2} &\left[\beta^* + (1 - \beta^*) \left(1 - \Gamma \frac{\partial u}{\partial r} \right)^{-1} \right] - \frac{\sigma B^2(t)}{\rho} u,
\end{aligned} \tag{9.2}$$

Energy equation:

$$\begin{aligned}
\frac{\partial T}{\partial t} + u \frac{\partial T}{\partial x} + v \frac{\partial T}{\partial r} &= \frac{k}{\rho c_p} \left(\frac{\partial^2 T}{\partial r^2} + \frac{1}{r} \frac{\partial T}{\partial r} \right) + \tau \left[D_B \frac{\partial C}{\partial r} \frac{\partial T}{\partial r} + \frac{D_T}{T_\infty} \left(\frac{\partial T}{\partial r} \right)^2 \right] \\
&\quad + \frac{1}{r} \frac{\partial (r q_r)}{\partial r} + \frac{Q(T - T_\infty)}{\rho c_p},
\end{aligned} \tag{9.3}$$

Concentration equation:

$$\frac{\partial C}{\partial t} + u \frac{\partial C}{\partial x} + v \frac{\partial C}{\partial r} = \frac{D_B}{r} \frac{\partial}{\partial r} \left(r \frac{\partial C}{\partial r} \right) + \frac{D_T}{T_\infty} \frac{1}{r} \frac{\partial}{\partial r} \left(r \frac{\partial T}{\partial r} \right). \tag{9.4}$$

9.1.1 Boundary Conditions

The physically realistic boundary conditions are described as:

$$u = u_w + u_{slip}, \quad v = -\frac{1}{a_0^2} \frac{4\nu x}{1 - \beta t}, \quad -k \frac{\partial T}{\partial r} = h_f(T_f - T), \quad C = C_w \quad \text{at} \quad r = a(t), \tag{9.5}$$

$$w \rightarrow 0, \quad T \rightarrow T_\infty, \quad C \rightarrow C_\infty \quad \text{as} \quad r \rightarrow \infty. \tag{9.6}$$

The slip velocity is given by

$$u_{slip} = L_1 \frac{\partial u}{\partial r} \left[\beta^* + (1 - \beta^*) \left(1 - \Gamma \frac{\partial u}{\partial r} \right)^{-1} \right]. \quad (9.7)$$

9.1.2 Dimensionless forms of Equations

We introduce the following dimensionless variables:

$$\begin{aligned} v &= -\frac{1}{a_0} \frac{2\nu}{\sqrt{1-\beta t}} \frac{f(\eta)}{\sqrt{\eta}}, & u &= \frac{1}{a_0^2} \frac{4\nu x}{1-\beta t} f'(\eta), & \eta &= \left(\frac{r}{a_0} \right)^2 \frac{1}{1-\beta t}, \\ \theta(\eta) &= \frac{T - T_\infty}{T_f - T_\infty}, & \phi(\eta) &= \frac{C - C_\infty}{C_w - C_\infty}. \end{aligned} \quad (9.8)$$

Substituting Eq. (9.8) into Eqs. (9.2) – (9.4), the flow equations are reduced as:

$$\begin{aligned} &\eta f''' (\beta^* + (1 - \beta^*) (1 - We f'')^{-1} + We f'' (1 - \beta^*) (1 - We f'')^{-2}) \\ &+ f'' [\beta^* + (1 - \beta^*) (1 - We f'')^{-1}] + \frac{We}{2} f''^2 ((1 - \beta^*) (1 - We f'')^{-2}) \\ &+ f f'' - f'^2 - A (f' + \eta f'') - M f' = 0, \end{aligned} \quad (9.9)$$

$$\frac{1}{Pr} [(1 + Rd(1 + (\theta_w - 1)\theta)^3 \eta \theta')] + f \theta' - A \eta \theta' + \eta (N_b \theta' \phi' + N_t \theta'^2) + \delta \theta = 0, \quad (9.10)$$

$$\eta \phi'' + \phi' + Le (f \phi' - A \eta \phi') + \frac{N_t}{N_b} [\eta \theta'' + \theta'] = 0, \quad (9.11)$$

subjected to boundary conditions

$$\begin{aligned} f(1) &= s, & f'(1) &= \chi + \delta_1 \left[\beta^* + (1 - \beta^*) (1 - We f''(1))^{-1} \right], \\ \theta'(1) &= -\gamma (1 - \theta(1)), & \phi(1) &= 1, \end{aligned} \quad (9.12)$$

$$f'(\infty) \rightarrow 0, \quad \theta(\infty) \rightarrow 0, \quad \phi(\infty) \rightarrow 0. \quad (9.13)$$

The dimensionless physical variables We , M , Nt , Nb , Le , s , γ , A , δ_1 , δ , θ_w and Rd denote the local Weissenberg number, the magnetic parameter, thermophoresis parameter, the Brownian motion parameter, the Lewis number, the mass transfer parameter, the Biot number (convective parameter), the unsteadiness parameter, the velocity slip factor, the heat generation/absorption parameter, the temperature ratio parameter and the radiation parameter. The above-mentioned parameters are

$$\begin{aligned} We & \left(= \frac{8\nu\Gamma r x}{(1-\beta t)^2 a_0^4} \right), \quad M \left(= \frac{\sigma a_0^2 B_0^2}{4\rho\nu} \right), \quad Nt \left(= \frac{\tau D_B (T_f - T_\infty)}{\nu T_\infty} \right), \quad Nb \left(= \frac{\tau D_B (C_w - C_\infty)}{\nu} \right), \\ Le & \left(= \frac{\nu}{D_B} \right), \quad s \left(= -\frac{a_0 u_w}{2\nu} \right), \quad \gamma \left(= \frac{a_0 h_f (1-\beta t)}{2kr} \right), \quad A \left(= \frac{a_0^2 \beta}{4\nu} \right), \\ \delta_1 & \left(= \frac{2L_1 r}{(1-\beta t) a_0^2} \right), \quad \delta \left(= \frac{Q(1-\beta t)}{u_w \rho c_p} \right), \quad \theta_w \left(= \frac{T_f}{T_\infty} \right) \quad \text{and} \quad Rd \left(= \frac{16\sigma^{**} T_\infty^3}{3k^* k} \right). \end{aligned} \quad (9.14)$$

9.1.3 Engineering Parameters

The most important physical and engineering related quantities are drag force along the cylindrical surface and rates of heat and mass transportation. The mathematical form of such quantities is written as:

$$C_f = \frac{\tau_{rx}|_{r=a(t)}}{\rho u_w^2/2}, \quad Nu = \frac{a(t)q_w|_{r=a(t)}}{2k(T_f - T_\infty)}, \quad Sh = \frac{a(t)q_m|_{r=a(t)}}{2D_B(C_w - C_\infty)}, \quad (9.15)$$

where τ_{rx} , q_w and q_m are expressed as:

$$\tau_{rx} = \mu_0 \frac{\partial u}{\partial r} \left[\beta^* + (1-\beta^*) \left(1 - \Gamma \frac{\partial u}{\partial r} \right)^{-1} \right], \quad q_w = -k \left(\frac{\partial T}{\partial r} \right) + q_r, \quad q_m = -D_B \left(\frac{\partial C}{\partial r} \right). \quad (9.16)$$

On substituting Eq. (9.8) into Eqs. (9.15) and (9.16), we obtain

$$\begin{aligned}
\frac{C_{fx}}{a(t)} &= f''(1) \left[\beta^* + (1 - \beta^*) (1 - We f''(1))^{-1} \right], \\
Nu &= -\theta'(1) \left[1 + Rd \left\{ [1 + (\theta_w - 1)\theta(1)]^3 \right\} \right], \\
Sh &= -\phi'(1).
\end{aligned} \tag{9.17}$$

9.2 Numerical Procedure

The nonlinear ODEs (9.9) – (9.11) along with (9.12) and (9.13) are solved by Runge-Kutta Fehlberg method. In this approach, the BVP is converted into the IVP. Let $f = p_1$, $f' = p_2$, $f'' = p_3$, $\theta = p_4$, $\theta' = p_5$, $\phi = p_6$, $\phi' = p_7$. Making use of these variables into Eqs. (9.9 – 9.13), the new system of ODEs is given below:

$$\begin{aligned}
&\eta p_3' (\beta^* + (1 - \beta^*) (1 - We p_3)^{-1} + We p_3 (1 - \beta^*) (1 - We p_3)^{-2}) \\
&+ p_3 [\beta^* + (1 - \beta^*) (1 - We p_3)^{-1}] + \frac{We}{2} p_3^2 ((1 - \beta^*) (1 - We p_3)^{-2}) \\
&+ p_1 p_3 - p_2^2 - A(p_2 + \eta p_3) - M p_2 = 0,
\end{aligned} \tag{9.18}$$

$$\frac{1}{Pr} [(1 + Rd(1 + (\theta_w - 1)p_4)^3 \eta p_5)'] + p_1 p_5 - A \eta p_5 + \eta (Nb p_5 p_7 + Nt p_5^2) + \delta p_4 = 0, \tag{9.19}$$

$$\eta p_7' + p_7 + Le(p_1 p_7 - A \eta p_7) + \frac{Nt}{Nb} [\eta p_5' + p_5] = 0, \tag{9.20}$$

$$\begin{aligned}
p_1(1) &= s, \quad p_2(1) = \chi + \delta_1 \left[\beta^* + (1 - \beta^*) (1 - We p_3(1))^{-1} \right], \\
p_5(1) &= -\gamma (1 - p_4(1)), \quad p_7(1) = 1,
\end{aligned} \tag{9.21}$$

$$p_2(\infty) \rightarrow \xi_1, \quad p_4(\infty) \rightarrow \xi_2, \quad p_6(\infty) \rightarrow \xi_3. \quad (9.22)$$

We find the solution of the above system of first order differential equations via Runge-Kutta numerical technique, which requires seven initial conditions. But, the above system contains three unknown values ξ_1 , ξ_2 and ξ_3 i.e., $f''(0)$, $\theta'(0)$ and $\phi(0)$, respectively. Thus, it is necessary to select the appropriate values of these unknowns such that far field conditions (at infinity) with the suitable domain length η_∞ . These guessed value are adjusted by Newton Raphson method such that iterative process is terminated when the following condition is satisfied:

$$\sum_i |\Theta_i^n - \Theta_i^{n-1}| \leq 10^{-6}.$$

9.2.1 Validation of Numerical Results

Table 9.1 elaborates numerical outcomes of $f''(1)$ for impermeable stretched cylinder $f''(1) = 1$ for varying δ_1 when $\beta^* = M = A = We = 0$. This table reveals that rising values of δ_1 leads to a decrease the skin friction magnitude. Moreover, it is observed that the obtained numerical data is in extremely decent agreement with those presented by Wang and Ng [107], Ishak *et al.* [108] and Abbas *et al.* [109] for stretched cylinder $f''(1) = 1$ and elucidates the accuracy and validity of the current numerical scheme.

9.3 Discussion of Numerical Approach

The system of Eqs. (9.9) – (9.11) with appropriate boundary conditions (9.12) and (9.13) is solved numerically via shooting scheme. The impact of pertinent physical parameters on the dimensionless velocity, temperature, nanoparticles concentration, skin friction coefficient, Nusselt number and Sherwood number is illustrated graphically through **Figs. 9.2 – 9.18**.

In this investigation, dual nature of solutions is captured for some particular values of mass transfer parameter s and shrinking parameter χ by setting distinct initial guesses. The range of controlling parameters is taken as: $0.1 \leq M \leq 0.3$, $0 \leq \delta \leq 0.2$, $0.1 \leq \gamma \leq 0.5$, $1.1 \leq R_d \leq 2.5$, $0 \leq A \leq -0.2$, $2.8 \leq s \leq 3.5$, $0.1 \leq Nb \leq 0.5$ and $2.0 \leq Le \leq 10$. The default values of controlling parameters are considered as: $We = 0.2$, $\beta^* = 0.1$, $Pr = 5.0$, $Le = 2.0$, $M = 0.2$, $Nt = 0.3$, $Nb = 0.3$, $R_d = 1.1$, $\delta = 0.1$, $\theta_w = 0.5$, $s = 3.0$, $A = -0.2$, $\gamma = 0.1$, $\delta_1 = 0.1$ and $\chi = -1.5$ throughout the computation, otherwise mentioned.

9.3.1 Momentum Boundary Layer

In this segment, our prime intention is to investigate the impact of active physical parameters on the flow characteristics, i.e., the skin friction coefficient and $f'(\eta)$, which are demonstrated graphically through **Figs. 9.2 – 9.7**. The plots of skin friction coefficient against the shrinking parameter χ for particular values of M and δ_1 are shown in **Fig. 9.2** and **Fig. 9.3**. From **Fig. 9.2**, it is revealed that for rising values of M , the critical value χ_c reduces from -1.9129 to -2.1633 and the magnitude of the absolute critical value $|\chi_c|$ increases. In upper branch solution case, the fluid velocity is higher in comparison to lower branch solution. Physically, with a rise in magnetic parameter M , the drag force named as Lorentz force rises and therefore accelerates the flow for upper branch solution while an opposite behavior is noted for lower branch solution. The impact of velocity slip parameter on the skin friction coefficient is illustrated through **Fig. 9.3**. In this plot, we noted existence range of dual solutions with respect to shrinking parameter χ . The dual solutions are calculated for $\chi < \chi_c$ and beyond the critical value i.e., $\chi_c < \chi$ solutions are not possible. The critical values χ_c are lessening from -1.7267 to -2.3745 as velocity slip parameter increases from 0 to 0.2. We reported that the upper solution is always higher than

lower branch solution. In this sense, we noticed that reduced skin friction decreases in case of upper branch solution and showing an opposite trend for lower branch solution. The variation of magnetic parameter versus $f'(\eta)$ is illustrated in **Fig. 9.4**. An enhancement in magnetic field creates a resistive force, which have an ability to decelerate the fluid's movement along the stretched surfaces which generates a declination in the velocity field. From this plot, we observe that the transverse magnetic field opposes the transport phenomenon. Therefore, for larger values of magnetic parameter M , velocity profile in case of first solution increases and it decreases monotonically for second solution. **Fig. 9.5** describes the pattern of $f'(\eta)$ for distinct δ_1 for both first and second solutions. This figure reveals that $f'(\eta)$ increases for higher δ_1 in upper branch and reduces for lower branch solutions. The influence of $f'(\eta)$ for A is depicted in **Fig. 9.6**. The curves depict that the velocity of the fluid rises for upper branch and reduces for lower branch. Here, magnitude of the velocity rises for the first solution and reduces for the second solution with higher A which justifies that the upper solution is physically stable in comparison to lower branch solution. The impact of s against $f'(\eta)$ is demonstrated in **Fig. 9.7**. By definition of mass transfer parameter, we can analyze three cases (i) $s < 0$ corresponds to mass injection case (ii) $s = 0$ refers to the solid surface without permeability, and (iii) $s > 0$ indicates the mass suction case. Here, we discussed the case of mass suction and reported that $f'(\eta)$ decreases in first solution and a reverse is noted in second solution.

9.3.2 Thermal Boundary Layer

The variation in Nu for different parameters is illustrated in **Figs. 9.8 – 9.11** for stretching and shrinking cylinder cases. **Fig. 9.8** elaborates the magnetic parameter M impact on the Nusselt number. The critical value χ_c decreases from -1.9129 to -2.1633 as M rises from 0.1

to 0.3. The heat transport rate increases for upper branch with magnetic parameter M while a reverse pattern is observed for lower branch and both solutions are terminated at critical value χ_c . It is illustrated from **Fig. 9.9**, as δ_1 increases from 0 to 0.2, χ_c decreases from -1.7267 to -2.3745 . As the velocity slip parameter δ_1 rises, the rate of heat transport increases for upper branch and decreases for lower branch. The variations of local Nusselt number against mass transfer parameter s for distinct γ are presented in **Fig. 9.10**. It is noted from this figure that the critical value related to suction parameter s_c decreases from 2.4101 to 2.4077, as the Biot number γ varies from 0.1 to 0.5. On the other hand, one can observe that the existence domain for dual solutions reduces. **Fig. 9.11** is plotted to examine the heat transport rate effects against shrinking parameter χ for varying values of R_d . It is noteworthy to mention that the critical value relating to shrinking parameter χ_c depreciates from -1.17267 to -2.0400 as radiation parameter R_d goes on 1.1 to 2.5. It is evident from this figure that the existence range of dual solutions decreases. **Fig. 9.12** illustrates the impact of Nb on $\theta(\eta)$. Clearly, Brownian motion parameter rises the temperature distribution for both solutions. It is due to the fact that the different nanoparticles have various values of Nb which upgrades the rate of heat transfer. **Fig. 9.13** describes the impacts of Biot number versus temperature profiles. Biot number releases the heat energy to the flow, it helps to raise the temperature profiles for upper and lower branch solutions.

9.3.3 Concentration Boundary Layer

Fig. 9.14 illustrates the distributions of Sherwood number against the shrinking parameter χ . We have sketched these graphs for varying values of M by keeping the rest of parameters fixed. As expected, the dual solution exists in case of shrinking cylinder. One can notice that

when M increases, the Sherwood number slightly rises for the first solution. On the other hand, an increasing behavior is observed for the second solution and results are more prominent in this case. This figure further indicates that the range of χ for which the multiple solutions are possible enhances by higher values of magnetic parameter M . **Fig. 9.15** describes the impact of δ_1 on Sherwood number. The plotted curves are visualized against shrinking parameter while all other parameters are fixed. We noticed higher Sherwood number for growing values of δ_1 for the upper branch solution whereas a dual behavior for lower branch solution is observed. Moreover, at the expansion of velocity slip parameter, the magnitude of critical values $|\chi_c|$ is greater in comparison with lower values of δ_1 . Variation in the profiles of Sherwood number for shrinking cylinder $\chi < 0$ is displayed in **Fig. 9.16**, for different γ . It is reported that the rise in Biot number γ diminishes the Sh for both solutions. The critical values for varying values of γ with respect to mass transfer parameter s are computed and depicted in this figure. The role of Le against concentration profile has been discussed in **Fig. 9.17**. Physically, Lewis number describes the relation of thermal to mass diffusivity, hence for large value of Le , thermal boundary layer is higher than concentration boundary layer. The existence of multiple solutions is presented in this graph. The influence of Nb on nanoparticles concentration is presented in **Fig. 9.18**. It is confirmed that an increment in Nb declines the nanoparticles concentration for both cases of first and second solutions.

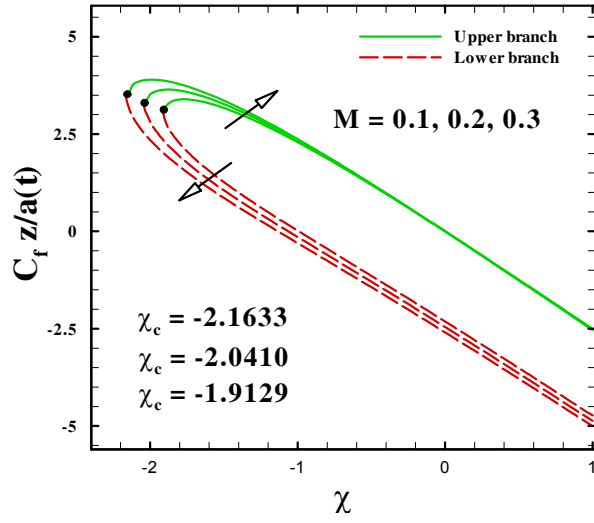


Fig. 9.2: Variation of friction coefficient against χ for varying M .

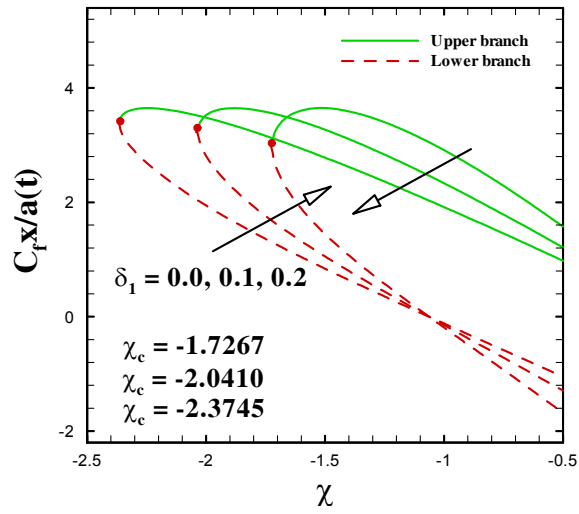


Fig. 9.3: Variation of friction coefficient against χ for varying δ_1 .

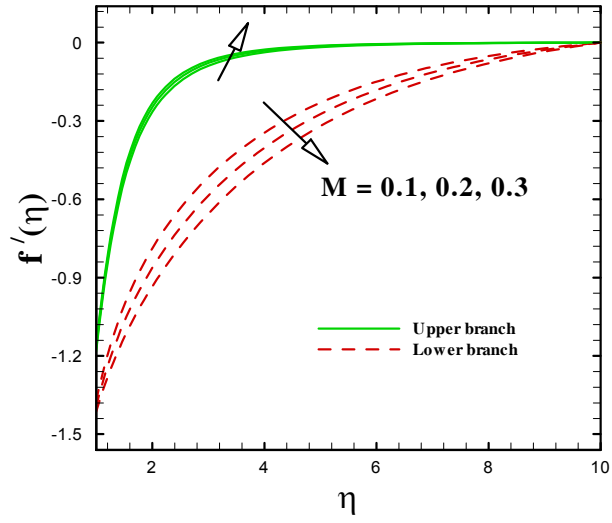


Fig. 9.4: Variation in $f'(\eta)$ for different values of M .

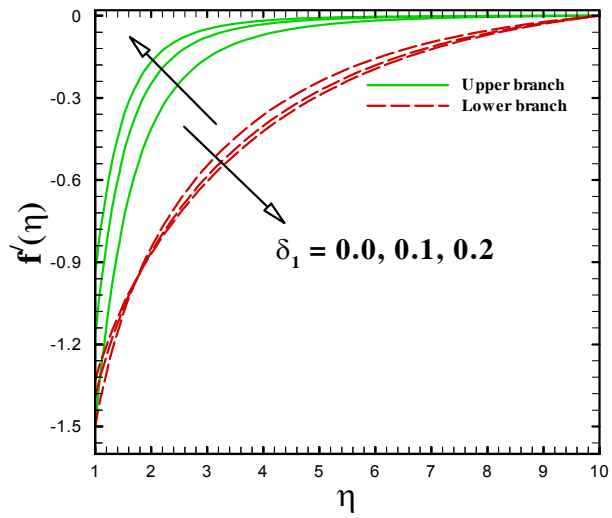


Fig. 9.5: Variation in $f'(\eta)$ for different values of δ_1 .

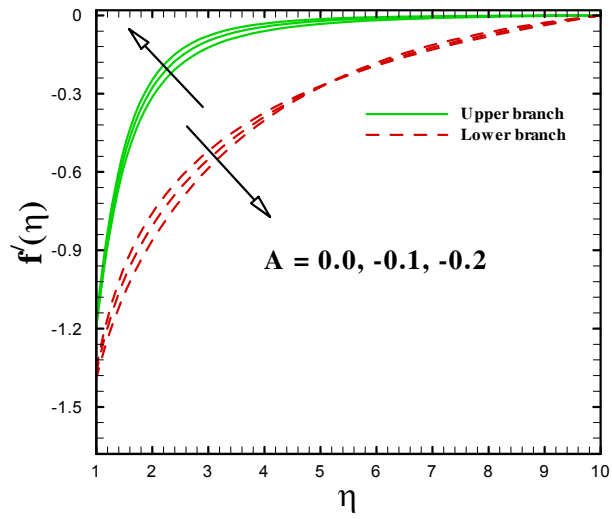


Fig. 9.6: Variation in $f'(\eta)$ for different values of A .

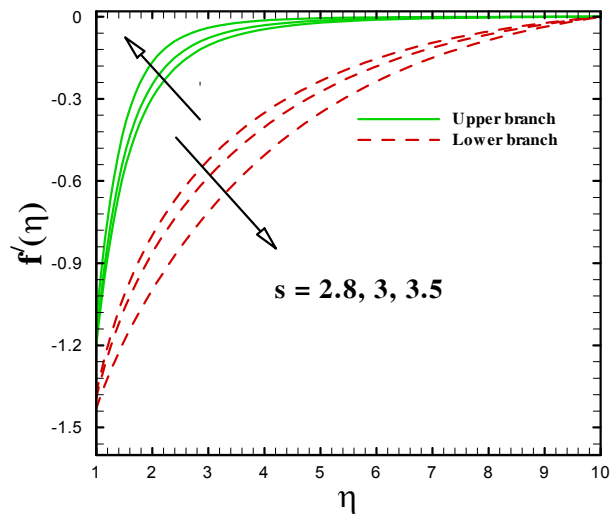


Fig. 9.7: Variation in $f'(\eta)$ for different values of s .

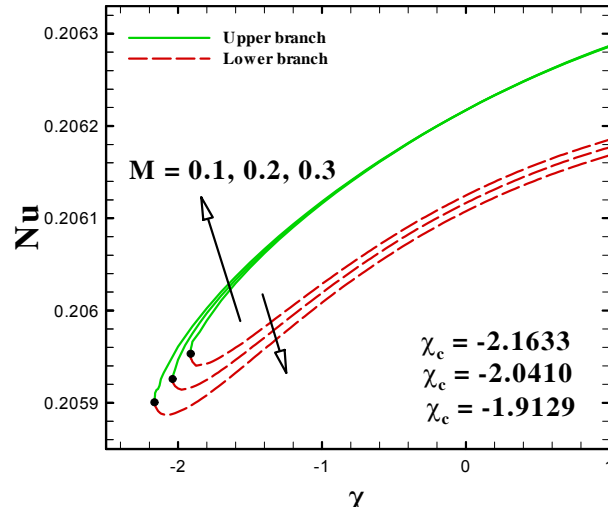


Fig. 9.8: Variation of Nu against χ for varying M .

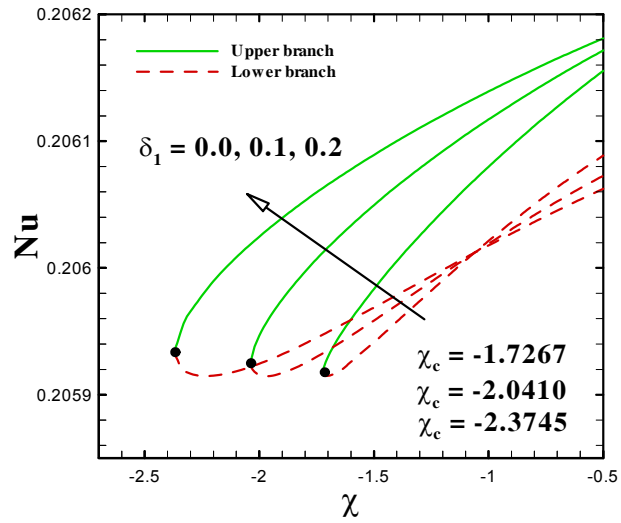


Fig. 9.9: Variation of Nu against χ for varying δ_1 .

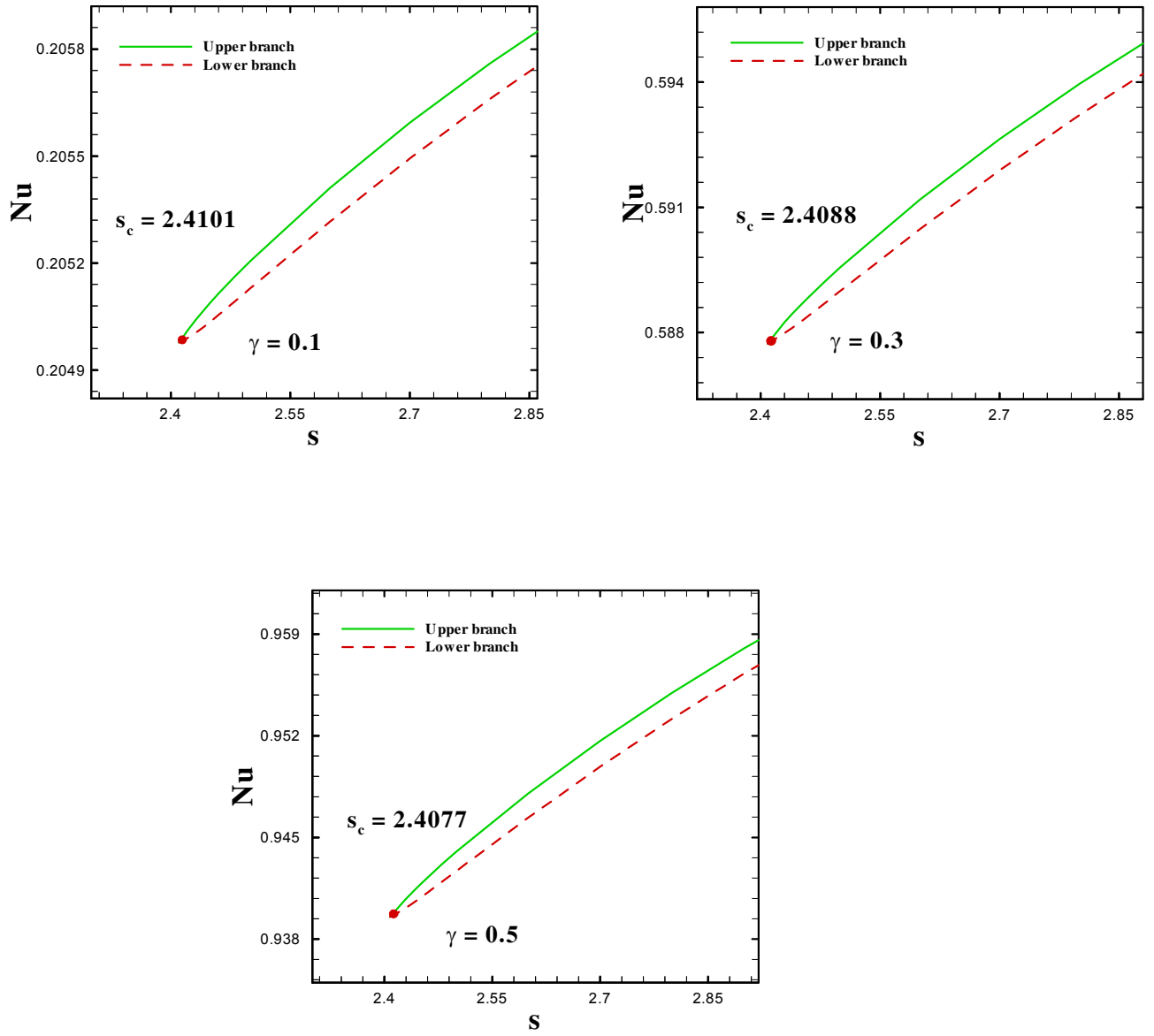


Fig. 9.10: Variation of Nu against χ for varying γ .

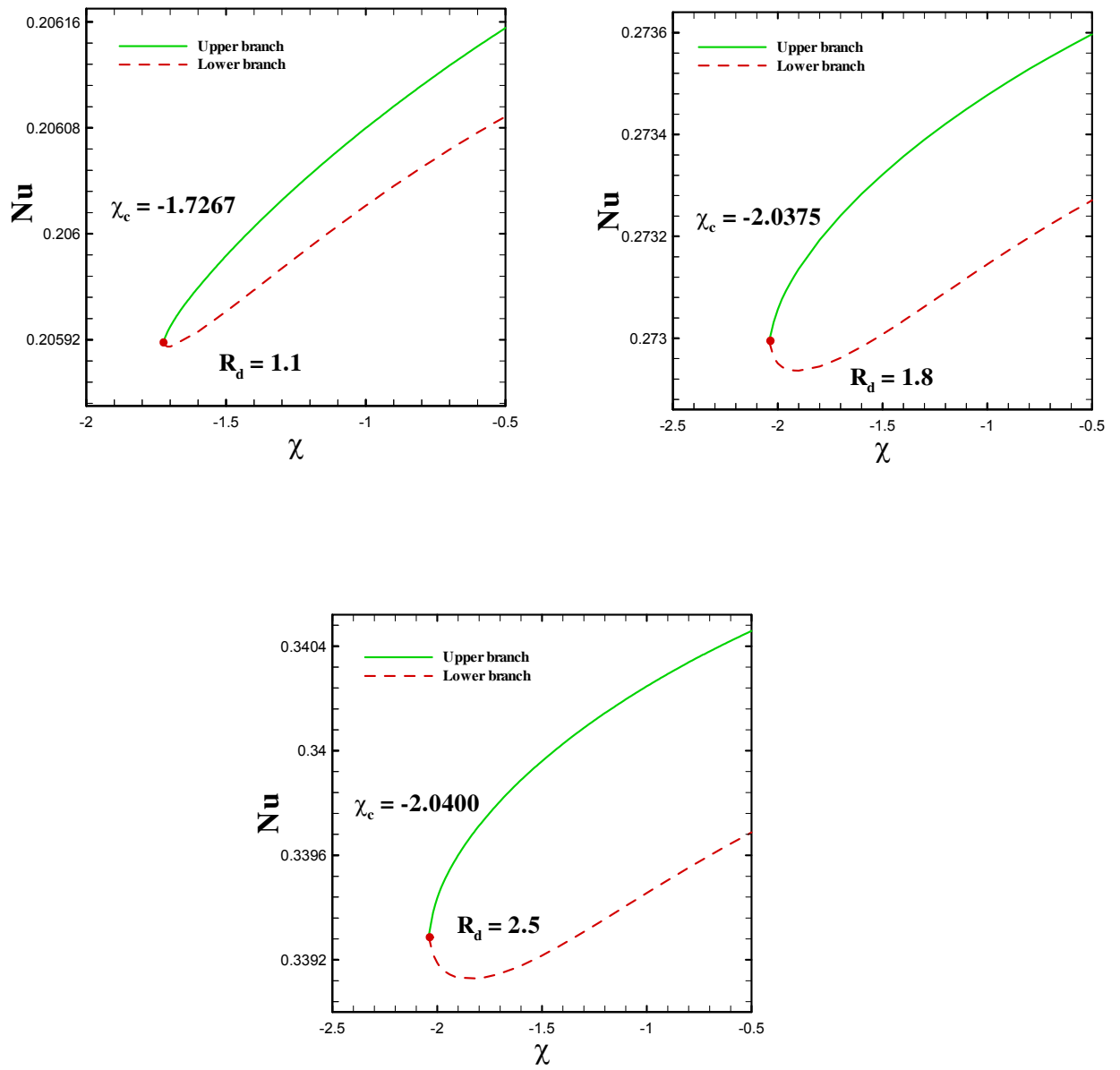


Fig. 9.11: Variation of Nu against χ for varying R_d .

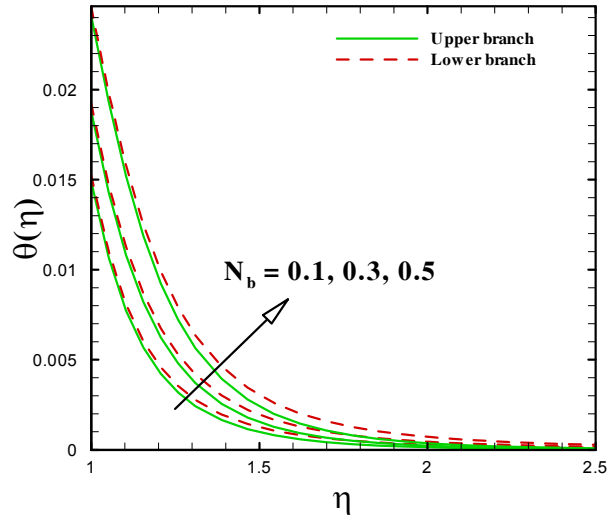


Fig. 9.12: Variation in $\theta(\eta)$ for different values of Nb .

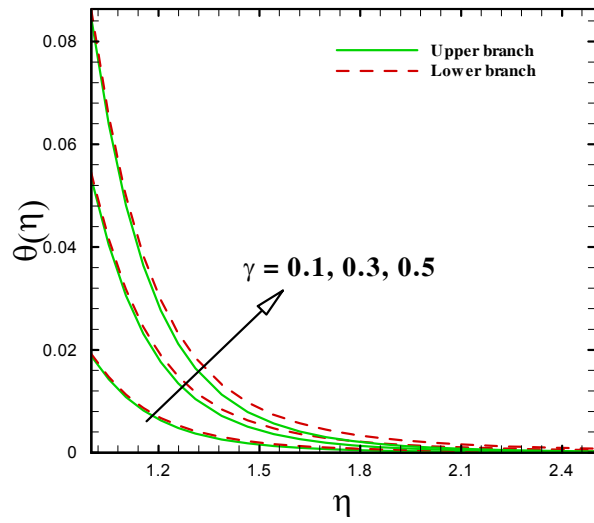


Fig. 9.13: Variation in $\theta(\eta)$ for different values of γ .

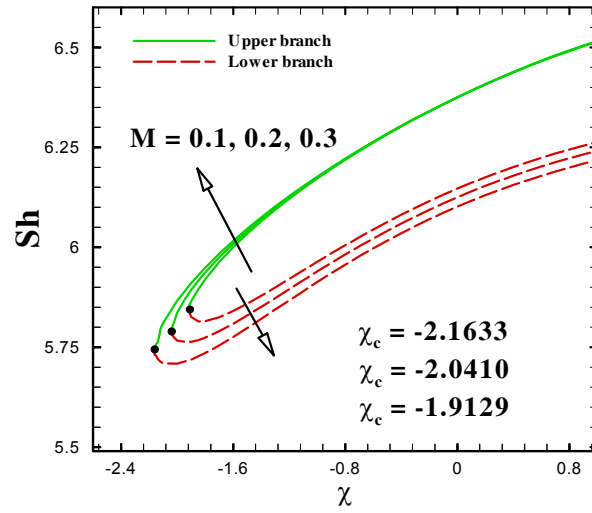


Fig. 9.14: Variation of Sh against χ for varying M .

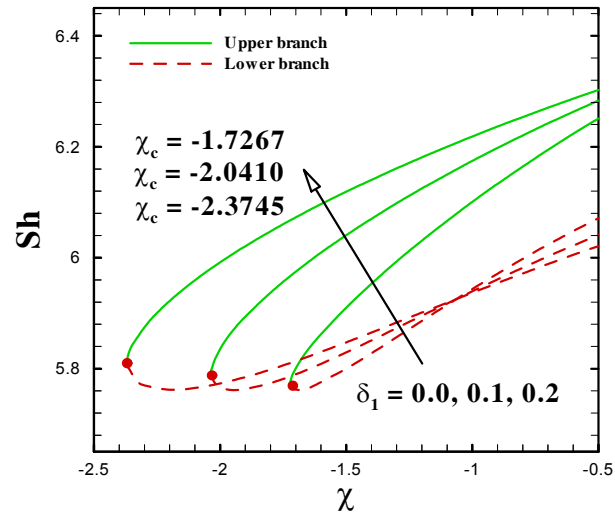


Fig. 9.15: Variation of Sh against χ for varying δ_1 .

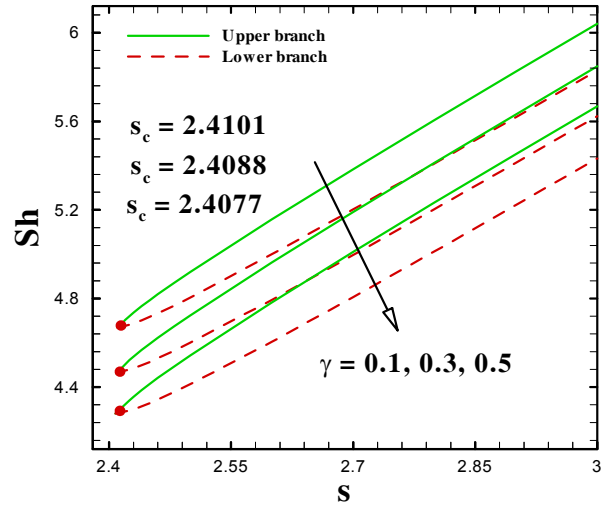


Fig. 9.16: Variation of Sh against s for varying δ .

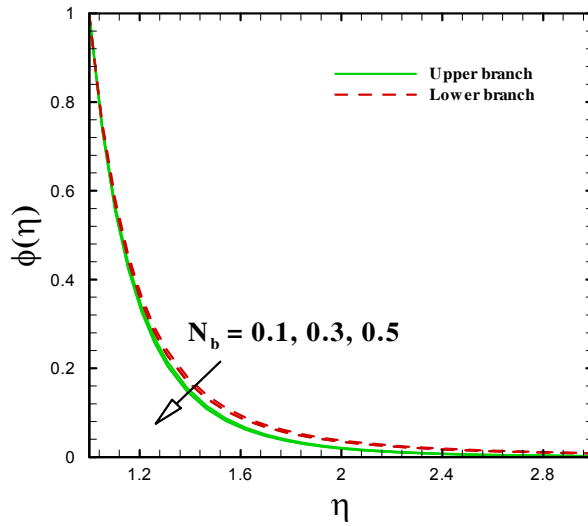


Fig. 9.17: Variation in $\phi(\eta)$ for different values of N_b .

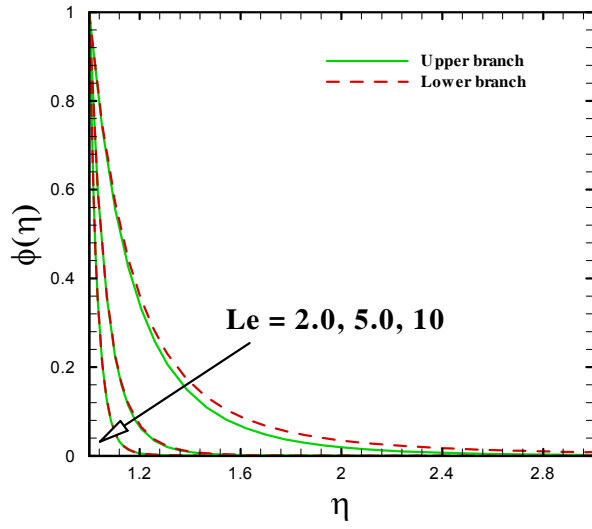


Fig. 9.18: Variation in $\phi(\eta)$ for different values of Le .

Table 9.1: The values of $f''(1)$ in case of $f''(1) = 1$ for varying δ_1 when $We = \beta^* = A = M = 0$.

δ_1	Wang and Ng [107]	Ishak <i>et al.</i> [108]	Abbas <i>et al.</i> [109]	Present result
0	-1.1778	-1.17810	-1.1860	-1.1863
0.1	-1.0116	—	-1.068	-1.01923
0.5	-0.6638	—	-0.664	-0.669442
1.0	-0.4739	—	-0.4743	-0.478448
2.0	-0.3070	—	-0.3073	-0.310147
5.0	-0.1532	—	-0.1534	-0.155021
10	-0.0848	—	-0.0850	-0.085875
20	—	—	-0.04536	-0.0457963
30	—	—	-0.0310	-0.0313121
50	—	—	-0.0210	-0.0192143

Chapter 10

Conclusions and Forthcoming Work

The research performed in this thesis has contributed in a number of ways in the field of non-Newtonian fluid mechanics. Particularly, this thesis has focused on the mathematical modelling for the non-Newtonian Williamson fluid by incorporating the effects of infinite shear rate viscosity. Additionally, the interest in this thesis was the transient behavior of Williamson fluid in various circumstances. This final chapter summarizes the results of this thesis and also suggest directions for future work.

10.1 Summary of Results

The key outcomes of this research work are precised as follows:

- The non-dimensional velocity profiles in addition to temperature profiles were reduced with an increment in the unsteadiness parameter.
- An increment in the Weissenberg number resulted in a decrease in fluid velocity; however, quite the opposite behavior was true for temperature field.

- On uplifting the viscosity ratio parameter, the momentum boundary-layer thickness was raised while an inverse behavior was observed for thermal boundary-layer thickness.
- The fluid temperature and its related thermal boundary-layer thickness were uplifted with higher temperature ratio and radiation parameters.
- The temperature field and thermal boundary-layer thickness were depressed by higher Prandtl number while an opposite trend was true for growing a Biot number.
- The augmented magnetic parameter was depreciated the nanofluid temperature as well as corresponding boundary-layer thickness.
- The influence of Brownian movement versus temperature and concentration profiles was opposite to each other.
- The fluid temperature along with thermal boundary-layer thickness were developing functions of Biot number.
- The fluid temperature was substantially raised by higher thermal conductivity parameter.
- The temperature and nanoparticles concentration were uplifted with an increment in thermophoretic parameter.
- The heat transport coefficient was noted to grow up with a higher Prandtl number.
- An increment in temperature difference parameter reduced the nanoparticles concentration.
- The friction coefficient was significantly raised by a higher Weissenberg number.

- Due to the higher thermophoresis parameter, the rate of heat transfer was found to decrease.
- It was observed that dual solutions occurred only for definite ranges of the shrinking parameter, while the solution was unique for the stretching case.
- We observed a substantial decline in local Sherwood number with an increment in Biot number.
- The nanoparticles concentration was reduced by increasing the values of Lewis number.

10.2 Suggestions for Future Work

This thesis is mainly concerned with the numerical solutions for transient flow of Williamson fluid due to diverse stretched geometries. The consequences of our numerical computations leave room for further development and expansion for the work that has just been carried out. However, there are still few suggestions that will be pursued in the future research, which are described as follows:

- This thesis presents the mathematical modelling for the 2D boundary layer flows. However, it could be extended for unsteady 3D boundary layer flow of Williamson fluid.
- We plan to extend this study for fluid flow through complex geometries like, flow through annular pipe, flow through curved surface, rotating disk, flow in a nozzle, thin film flow, channel flow, peristaltic flow, flow in cavity, flow in air ducts and flow through bundles of circular fibres.

- Regarding the numerical simulation, it could be interesting to study the Williamson fluid flows via advanced numerical methods, namely: the finite difference method (FDM), finite volume method (FVM), finite element method (FEM) and lattice Boltzmann method (LBM).

Bibliography

- [1] J. Walker, Serious fun with polyox, silly putty, slime and other non-Newtonian fluids, *Scientific American*, **239** (1978).
- [2] R.B. Bird, O. Hassager, R.C. Armstrong and C.F. Curtiss, *Dynamics of Polymeric Fluids*, **1** (1977).
- [3] H.A. Barnes, J.F. Hutton and K. Walters, An introduction to rheology, Elsevier, (1989).
- [4] J.F. Morris, A review of microstructure in concentrated suspensions and its implication for rheology and bulk flow, *Rheol. Acta*, **48** (2009) 909-923.
- [5] A.Y. Malkin, Non-Newtonian viscosity in steady-state shear flows, *J. Non-Newton. Mech.*, **192** (2013) 48–65.
- [6] R.V. Williamson, The flow of pseudo plastic materials, *Ind. Eng. Chem.*, **21** (1929) 1108-1111.
- [7] S. Nadeem and S. Akram, Influence of inclined magnetic field on peristaltic flow of a Williamson fluid model in an inclined symmetric or asymmetric channel, *Math. Comp. Modell.*, **52** (2010) 107.

- [8] C. Vasudev, U.R. Rao, M.V.S Reddy and G.P. Rao, Peristaltic pumping of Williamson fluid through a porous medium in a horizontal channel with heat transfer, *Amer. J. Sci. Ind. Res.*, **1** (2010) 656-666.
- [9] N.S. Akbar, S. Nadeem, C. Lee, Z.H. Khan and R.U. Haq, Numerical study of Williamson nanofluid flow in an asymmetric channel, *Results Phys.*, **3** (2013) 161-166.
- [10] N.T. Eldabe, M.A. Elogail, S.M. Elshaboury and A.A. Hasan, Hall effects on the peristaltic transport of Williamson fluid through a porous medium with heat and mass transfer, *Appl. Math. Modell.*, **40** (2016) 315-328.
- [11] R.S.R. Gorla and B.J. Gireesha, Dual solutions for stagnation-point flow and convective heat transfer of a Williamson nanofluid past a stretching/shrinking sheet, *Heat Mass Transf.*, **52** (2016) 1153-1162.
- [12] K.G. Kumar, N.G. Rudraswamy, B.J. Gireesha and S. Manjunatha, Non linear thermal radiation effect on Williamson fluid with particle-liquid suspension past a stretching surface, *Results Phys.*, **7** (2017) 3196-3202.
- [13] M. Ramzan, M. Bilal and J.D. Chung, MHD stagnation point Cattaneo-Christov heat flux in Williamson fluid flow with homogeneous-heterogeneous reactions and convective boundary condition: A numerical approach, *J. Mol. Liq.*, **225** (2017) 856-862.
- [14] S.U.S. Choi, Enhancing thermal conductivity of fluids with nanoparticles, *Develop Appl. Non- New. Flows*, **231** (1995) 99 – 105.
- [15] H. Masuda, A. Ebata, K. Teramae and N. Hishinuma, Alteration of thermal conductivity and viscosity of liquid by dispersing ultra-fine particles, *Netsu Bussei*, **7** (1993) 227 – 233.

- [16] J.A. Eastman, S.U.S. Choi, S. Li, W. Yu and L.J. Thompson, Anomalously increased effective thermal conductivities of ethylene glycol-base nanofluids containing copper nanoparticles, *Appl. Phys. Lett.*, **78** (2001) 718-720.
- [17] J. Buongiorno, Convective transport in nanofluids, *ASME J. Heat Transf.*, **128** (2006) 240–250.
- [18] R.J. Tiwari and M.K. Das, Heat transfer augmentation in a two sided lid driven differentially heated square cavity utilizing nanofluids, *Int. J. Heat Mass Transf.*, **50** (2007) 2002–2018.
- [19] K.V. Wong and O.D. Leon, Applications of nanofluids: current and future, *Adv. Mech. Eng.*, **2010** (2010) 1 – 12.
- [20] A.V. Kuznetsov and D.A. Nield, Natural convective boundary-layer flow of a nanofluid past a vertical plate, *Int. J. Therm. Sci.*, **49** (2010) 243–247.
- [21] W.A. Khan and I. Pop, Free convection boundary layer flow past a horizontal flat plate embedded in a porous medium filled with a nanofluid, *ASME J. Heat Transf.*, **133** (2011) 157 – 163.
- [22] M.A.A. Hamad and I. Pop, Unsteady MHD free convection flow past a vertical permeable flat plate in a rotating frame of reference with constant heat surface in a nanofluid, *Heat Mass Transf.*, **47** (2012) 1517 – 1524.
- [23] M. Sheikholeslami and D.D. Ganji, Three dimensional heat and mass transfer in a rotating system using nanofluid, *Powd. Tech.*, **253** (2014) 789 – 796.

- [24] R. Dhanai, P. Rana and L. Kumar, Multiple solutions of MHD boundary layer flow and heat transfer behavior of nanofluids induced by a power-law stretching/shrinking permeable sheet with viscous dissipation, *Powd. Tech.*, **273** (2015) 62 – 70.
- [25] Hashim and M. Khan, A revised model to analyze the heat and mass transfer mechanisms in the flow of Carreau nanofluids, *Int. J. Heat Mass Transf.*, **103** (2016) 291 – 297.
- [26] T. Hayat, S. Qayyum, A. Alsaedi and B. Ahmad, Magnetohydrodynamic (MHD) nonlinear convective flow of Walters-B nanofluid over a nonlinear stretching sheet with variable thickness, *Int. J. Heat Mass Transf.*, **110** (2017) 506 – 514.
- [27] M.K. Nayak, N.S. Akbar, V.S. Pandey, Z.H. Khan and D. Tripathi, 3D free convective MHD flow of nanofluid over permeable linear stretching sheet with thermal radiation, *Powd. Tech.*, **315** (2017) 205 – 215.
- [28] A.S. Dogonchi and D.D. Ganji, Analytical solution and heat transfer of two-phase nanofluid flow between non-parallel walls considering Joule heating effect, *Powd. Tech.*, **318** (2017) 390 – 400.
- [29] P.H. Roberts, Introduction to Magnetohydrodynamics, Longmans, New York, (1967).
- [30] K.B. Pavlov, Magnetohydrodynamic flow of an incompressible viscous fluid caused by deformation of a surface, *Magnetohydrodynamics*, **10** (1974) 146–148.
- [31] A. Chakrabarti and A.S. Gupta, Hydromagnetic flow and heat transfer over a stretching sheet, *Quarterly Appl. Math.*, **37** (1979) 73–78.
- [32] T. Hayat, M. Qasim and S. Mesloub, MHD flow and heat transfer over permeable stretching sheet with slip conditions, *Int. J. Numer. Methods Fluids*, **66** (2011) 63-75.

- [33] M. Turkyilmazoglu, Exact analytical solutions for heat and mass transfer of MHD slip flow in nanofluids, *Chem. Eng. Sci.*, **84** (2012) 182-187.
- [34] H. Dessie and N. Kishan, MHD effects on heat transfer over stretching sheet embedded in porous medium with variable viscosity, viscous dissipation and heat source/sink, *Ain Shams Eng. J.*, (2014) doi.org/10.1016/j.asej.2014.03.008.
- [35] M. Waqas, M. Farooq, M.I. Khan, A. Alsaedi, T. Hayat and T. Yasmeen, Magnetohydrodynamic (MHD) mixed convection flow of micropolar liquid due to nonlinear stretched sheet with convective condition, *Int. J. Heat Mass Transf.*, **102** (2016) 766 – 772.
- [36] P.B.A. Reddy and R. Das, Estimation of MHD boundary layer slip flow over a permeable stretching cylinder in the presence of chemical reaction through numerical and artificial neural network modeling, *Eng. Sci. Tech. Int. J.*, **19** (2016) 1108-1116.
- [37] K.L. Hsiao, Combined electrical MHD heat transfer thermal extrusion manufacturing system efficiency by using Carreau-nanofluid with parameters control method, *Energy*, **130** (2017) 486-499.
- [38] K.L. Hsiao, Stagnation electrical MHD nanofluid mixed convection with slip boundary on a stretching sheet, *Appl. Therm. Eng.*, **112** (2017) 1281-1288.
- [39] R.U. Haq, Z. Hamouch, S.T. Hussain and T. Mekkaoui, MHD mixed convection flow along a vertically heated sheet, *Int. J. Hydrog. Energy*, **42** (2017) 15925 – 15932.
- [40] Z. Shah, E. Bonyah, S. Islam, W. Khan and M. Ishaq, Radiative MHD thin film flow of Williamson fluid over an unsteady permeable stretching sheet, *Heliyon*, **4** (2018) e00825.

- [41] X.Y. Tian, B.W. Li and Z.M. Hu, Convective stagnation point flow of a MHD non-Newtonian nanofluid towards a stretching plate, *Int. J. Heat Mass Transf.*, **127** (2018) 768-780.
- [42] M. Azam, A. Shakoor, H F. Rasool and M. Khan, Numerical simulation for solar energy aspects on unsteady convective flow of MHD Cross nanofluid: A revised approach, *Int. J. Heat Mass Transf.*, **131** (2019) 495-505.
- [43] S. Mukhopadhyay, K. Bhattacharyya and G. C. Layek, Steady boundary layer flow and heat transfer over a porous moving plate in presence of thermal radiation, *Int. J. Heat Mass Transf.*, **54** (2011) 2751 – 2757.
- [44] R. Cortell, MHD (magneto-hydrodynamic) flow and radiative nonlinear heat transfer of a viscoelastic fluid over a stretching sheet with heat generation/absorption, *Energy*, **74** (2014) 896 – 905.
- [45] T. Hayat, M. Imtiaz, A. Alsaedi and M.A. Kutbi, MHD three-dimensional flow of nanofluid with velocity slip and nonlinear thermal radiation, *J. Magn. Magn. Mater.*, **396** (2015) 31 – 37.
- [46] W.A. Khan, O.D. Makinde and Z.H. Khan, Non-aligned MHD stagnation point flow of variable viscosity nanofluids past a stretching sheet with radiative heat, *Int. J. Heat Mass Transf.*, **96** (2016) 525 – 534.
- [47] D. Pal and P. Saha, Influence of nonlinear thermal radiation and variable viscosity on hydromagnetic heat and mass transfer in a thin liquid film over an unsteady stretching surface, *Int. J. Mech. Sci.*, **119** (2016) 208-216.

- [48] M. Waqas, M.I. Khan, T. Hayat and A. Alsaedi, Numerical simulation for magneto Carreau nanofluid model with thermal radiation: A revised model, *Comp. Meth. Appl. Mech. Eng.*, **324** (2017) 640 – 653.
- [49] B.C. Prasannakumara, B.J. Gireesha, M.R. Krishnamurthy and K.G. Kumar, MHD flow and nonlinear radiative heat transfer of Sisko nanofluid over a nonlinear stretching sheet, *Inf. Med. Unlocked*, **9** (2017) 123-132.
- [50] P. Sreedevi, P.S. Reddy and A.J. Chamkha, Heat and mass transfer analysis of nanofluid over linear and non-linear stretching surfaces with thermal radiation and chemical reaction, *Powd. Tech.*, **315** (2017) 194-204.
- [51] F.A. Soomro, R.U. Haq, Q.M. Al-Mdallal and Q. Zhang, Heat generation/absorption and nonlinear radiation effects on stagnation point flow of nanofluid along a moving surface, *Res. Phys.*, **8** (2018) 404-414.
- [52] C.L.M. Navier, Sur les lois du mouvement des fluids, *C.R. Acad. Sci. France*, **6** (1827) 389–440.
- [53] C.Y. Wang, Flow due to a stretching boundary with partial slip-an exact solutions of the Navier-Stokes equations, *Chem. Eng. Sci.*, **57** (2002) 3745–3747.
- [54] L. Zheng, C. Zhang, X. Zhang and J. Zhang, Flow and radiation heat transfer of a Nanofluid over a stretching sheet with velocity slip and temperature jump in porous medium, *J. Franklin Inst.*, **350** (2013) 990-1007.
- [55] S. Mukhopadhyay, Analysis of boundary layer flow over a porous nonlinearly stretching sheet with partial slip at the boundary, *Alex. Eng. J.*, **52** (2013) 563-569.

- [56] M. Khan and Hashim, Effects of multiple slip on flow of magneto-Carreau fluid along wedge with chemically reactive species, *Neural Comput. Appl.*, (2016) doi:10.1007/s00521-016-2825-3.
- [57] F. Xie, Y. Li, X. Wang, Y. Wang, G. Lei and K. Xing, Numerical study on flow and heat transfer characteristics of low pressure gas in slip flow regime, *Int. J. Thermal Sci.*, **124** (2018) 131 – 145.
- [58] A.R. Bestman, Radiative heat transfer to flow of a combustible mixture in a vertical pipe, *Int. J. Energy Res.*, **15** (1991) 179–184.
- [59] R. Kandasamy, K. Periasamy, and K.K.S. Prabhu, Effects of chemical reaction, heat and mass transfer along a wedge with heat source and concentration in the presence of suction or injection, *Int. J. Heat Mass Transf.*, **48** (2005) 1388–1394.
- [60] O.D. Makinde, P.O. Olanrewaju and W.M. Charles, Unsteady convection with chemical reaction and radiative heat transfer past a flat porous plate moving through a binary mixture, *Afrika Matematika*, **21** (2011) 1-17.
- [61] K. A. Maleque, Unsteady natural convection boundary layer heat and mass transfer flow with exothermic chemical reactions, *J. Pure Appl. Math.*, **9** (2013) 17–41.
- [62] M. Wahiduzzaman, M.S. Khan and I. Karim, MHD convective stagnation flow of nanofluid over a shrinking surface with thermal radiation, heat generation and chemical reaction, *Procedia Eng.*, **105** (2015) 398-405.

- [63] F. Mabood, S. Shateyi, M.M. Rashidi, E. Momoniat and N. Freidoonimehr, MHD stagnation point flow heat and mass transfer of nanofluids in porous medium with radiation, viscous dissipation and chemical reaction, *Adv. Powd. Tech.*, **27** (2016) 742-749.
- [64] O.D. Makinde and I.L. Animasaun, Thermophoresis and Brownian motion effects on MHD bioconvection of nanofluid with nonlinear thermal radiation and quartic chemical reaction past an upper horizontal surface of a paraboloid of revolution, *J. Mol. Liq.*, **221** (2016) 733-743.
- [65] M.R. Eid, Chemical reaction effect on MHD boundary-layer flow of two-phase nanofluid model over an exponentially stretching sheet with a heat generation, *J. Mol. Liq.*, **220** (2016) 718-725.
- [66] P.S. Reddy, P. Sreedevi and A.J. Chamkha, MHD boundary layer flow, heat and mass transfer analysis over a rotating disk through porous medium saturated by Cu-water and Ag-water nanofluid with chemical reaction, *Powd. Tech.*, **307** (2017) 46-55.
- [67] M. Mustafa, J.A. Khan, T. Hayat and A. Alsaedi, Buoyancy effects on the MHD nanofluid flow past a vertical surface with chemical reaction and activation energy, *Int. J. Heat Mass Transf.*, **108** (2017) 1340-1346.
- [68] K.L. Hsiao, To promote radiation electrical MHD activation energy thermal extrusion manufacturing system efficiency by using Carreau-nanofluid with parameters control method, *Energy*, **130** (2017) 486-499.

- [69] M.I. Khan, S. Qayyum, T. Hayat, M. Waqas and A. Alsaedi, Entropy generation minimization and binary chemical reaction with Arrhenius activation energy in MHD radiative flow of nanomaterial, *J. Mol. Liq.*, **259** (2018) 274-283.
- [70] T.C. Chaim, Hydromagnetic flow over a surface stretching with a power-law velocity, *Int. Eng. Sci.*, **33** (1995) 429-435.
- [71] F. Aman, A. Ishak and I. Pop, Magneto hydrodynamic stagnation-point flow towards a stretching/shrinking sheet with slip effects, *Int. Commun. Heat Mass Transf.*, **47** (2013) 68-72.
- [72] S.K. Nandy and T.R. Mahapatra, Effects of slip and heat generation/absorption on MHD stagnation flow of nanofluid past a stretching/shrinking surface with convective boundary conditions, *Int. Heat Mass Transf.*, **64** (2013) 1091-1100.
- [73] S.H.M. Saleh, N.M. Arifin, R. Nazar, F.M. Ali and I. Pop, Mixed convection stagnation flow towards a vertical shrinking sheet, *Int. J. Heat Mass Transf.*, **73** (2014) 839-848.
- [74] G.C. Dash, R.S. Tripathy, M.M. Rashidi and S.R. Mishra, Numerical approach to boundary layer stagnation-point flow past a stretching/shrinking sheet, *J. Mol. Liq.*, **221** (2016) 860-866.
- [75] N.A.A.M. Nasir, A. Ishak and I. Pop, Stagnation-point flow and heat transfer past a permeable quadratically stretching/shrinking sheet, *Chin. J. Phys.*, **55** (2017) 2081-2091.
- [76] G.S. Seth, A.K. Singha, M.S. Mandal, A. Banerjee and K. Bhattacharyya, MHD stagnation-point flow and heat transfer past a non-isothermal shrinking/stretching sheet in porous medium with heat sink or source effect, *Int. J. Mech. Sci.*, **134** (2017) 98-111.

- [77] L.J. Crane, Flow past a stretching plate, *ZAMP*, **21** (1970) 645-647.
- [78] L.J. Grubka and K.M. Bobba, Heat transfer characteristics of a continuous, stretching surface with variable temperature, *J. Heat Transf.*, **107** (1985) 248-250.
- [79] R. Cortell, Viscous flow and heat transfer over a nonlinearly stretching sheet, *Appl. Math. Comp.*, **184** (2007) 864 – 873.
- [80] M. Khan, Hashim, M. Hussain and M. Azam, Magnetohydrodynamic flow of Carreau fluid over a convectively heated surface in the presence of non-linear radiation, *J. Magn. Magn. Mat.*, **412** (2016) 63-68.
- [81] J. Rahimi, D.D. Ganji, M. Khaki and K. Hosseinzadeh, Solution of the boundary layer flow of an Eyring-Powell non-Newtonian fluid over a linear stretching sheet by collocation method, *Alex. Eng. J.*, **56** (2017) 621-627.
- [82] U.S. Mahabaleshwar, I.E. Sarris and G. Lorenzini, Effect of radiation and Navier slip boundary of Walters' liquid B flow over a stretching sheet in a porous media, *Int. J. Heat Mass Transf.*, **127** (2018) 1327-1337.
- [83] V.M. Falkner and S.W. Skan, Some approximate solutions of the boundary-layer for flow past a stretching boundary, *SIAM J. Appl. Math.*, **49** (1931) 1350 – 1358.
- [84] R. Rajagopal, A.S. Gupta and T.Y. Na, A note on the Falkner-Skan flows of a non-Newtonian fluid, *Int. J. Non Linear Mech.*, **18** (1983) 313 – 320.
- [85] A.J. Chamkha, M. Mujtaba, A. Quadri and C. Issa, Thermal radiation effects on MHD forced convection flow adjacent to a non-isothermal wedge in the presence of heat source or sink, *Heat Mass Transf.*, **39** (2003) 305-312.

- [86] M.A. Hossain, S. Bhowmik, R.S.R. Gorla, Unsteady mixed-convection boundary layer flow along a symmetric wedge with variable surface temperature, *Int. J. Eng. Sci.*, **44** (2006) 607-620.
- [87] A. Ishaq, R. Nazar, I. Pop, MHD Boundary-layer flow of a micropolar fluid past a wedge with variable wall temperature, *Acta Mech.*, **196** (2008) 75 – 86.
- [88] K.L. Hsiao, MHD mixed convection for viscoelastic fluid past a porous wedge, *Int. J. Eng. Sci.*, **46** (2011) 1 – 8.
- [89] T. Hayat, A. Shafiq, M. Imtiaz and A. Alsaedi, Impact of melting phenomenon in the Falkner-Skan wedge flow of second grade nanofluid: A revised model, *J. Mol. Liq.*, **215** (2016) 664 – 670.
- [90] L.J. Crane, Boundary layer flow due to a stretching cylinder, *ZAMP*, **26** (1975) 619–622.
- [91] C.Y. Wang, Fluid flow due to a stretching cylinder, *Phys. Fluids*, **31** (1988) 466 – 468.
- [92] A. Ishak and R. Nazar, Laminar boundary layer flow along a stretching cylinder, *Eur. J. Sci.*, **36** (2009) 22–29.
- [93] Y.Y. Lok and I. Pop, Wang’s shrinking cylinder problem with suction near a stagnation point, *Phys. Fluids*, **23** (2011) 083102.
- [94] T. Fang, J. Zhang and Y. Zhong, Note on unsteady viscous flow on the outside of an expanding or contracting cylinder, *Commun. Nonlinear Sci. Numer. Simul.*, **17** (2012) 3124 – 3128.

- [95] K. Zaimi, A. Ishak and I. Pop, Unsteady flow due to a contracting cylinder in a nanofluid using Buongiorno's model, *Int. J. Heat Mass Transf.*, **68** (2014) 509-513.
- [96] S. Sharidan, T. Mahmood and I. Pop, Similarity solutions for the unsteady boundary layer flow and heat transfer due to a stretching sheet, *Int. J. Appl. Mech. Eng.*, **11** (2006) 647 – 654.
- [97] A.J. Chamkha, A.M. Aly and M.A. Mansour, Similarity solution for unsteady heat and mass transfer from a stretching surface embedded in a porous medium with suction/injection and chemical reaction effects, *Chem. Eng. Commun.*, **197** (2010) 846 – 858.
- [98] M. Khan and M. Azam, Unsteady boundary layer flow of a Carreau fluid over a permeable stretching surface, *Results Phys.*, **6** (2016) 1168 – 1174.
- [99] L.J. Grubka and K.M. Bobba, Heat transfer characteristics of a continuous stretching surface with variable temperature, *ASME J. Heat Transf.*, **107** (1985) 248 – 250.
- [100] C.H. Chen, Laminar mixed convection adjacent to vertical continuously stretching sheets, *Heat Mass Transf.*, **33** (1998) 471 – 476.
- [101] B.L. Kuo, Application of the differential transformation method to the solutions of Falkner-Skan wedge flow, *Acta Mech.*, **164** (2003) 161 – 174.
- [102] A. Ishaq, R. Nazar, I. Pop, Moving wedge and flat plate in a micropolar fluid, *Int. J. Eng. Sci.*, **44** (2006) 1225 – 1236.
- [103] P.D. Ariel, Axisymmetric flow due to a stretching sheet with partial slip, *Int. J. Comput. Math. Appl.*, **54** (2007) 69 – 83.

- [104] O.D. Makinde, F. Mabood, W.A. Khan and M.S. Tshehla, MHD flow of a variable viscosity nanofluid over a radially stretching convective surface with radiative heat, *J. Mol. Liq.*, **219** (2016) 24 – 30.
- [105] C.Y. Wang, Stagnation flow towards a shrinking sheet, *Int. J. Nonlinear Mech.*, **43** (2008) 377–382.
- [106] S.K. Soid, A. Ishak and I. Pop, Unsteady MHD flow and heat transfer over a shrinking sheet with ohmic heating, *Chin. J. Phys.*, **55** (2017) 1626-1636.
- [107] C.Y. Wang and C. Ng, Slip flow due to a stretching cylinder, *Int. J. Non-Linear Mech.*, **46** (2011) 1191-1195.
- [108] A. Ishak, R. Nazar and I. Pop, Uniform suction/blowing effect on flow and heat transfer due to a stretching cylinder, *Appl. Math. Model.*, **32** (2008) 2059-2066.
- [109] Z. Abbas, R. Perveen, M. Sheikh and I. Pop, Thermophoretic diffusion and nonlinear radiative heat transfer due to a contracting cylinder in a nanofluid with generalized slip condition, *Results Phys.*, **6** (2016) 1080-1087.

 Turnitin Originality Report

Numerical Simulation of Time-dependent Flow of Williamson Fluid with Heat Transfer by Aamir Hamid.

From DRSM (DRSML)

- Processed on 02-Dec-2019 14:16 PKT
- ID: 1225006861
- Word Count: 29116

Similarity Index
16%
Similarity by Source

Internet Sources:
3%
Publications:
10%
Student Papers:
12%


3/12/2019
Cal Person (Turnitin)
Quaid-i-Azam University
Islamabad

sources:
1

1% match (student papers from 06-Jun-2018)

Submitted to Higher Education Commission Pakistan on 2018-06-06

2

< 1% match (publications)

M. Khan, M. Azam, A.S. Alshomrani. "Effects of melting and heat generation/absorption on unsteady Falkner-Skan flow of Carreau nanofluid over a wedge", International Journal of Heat and Mass Transfer, 2017

3

< 1% match (publications)

Hashim, Masood Khan, Ali Saleh Alshomrani. "Numerical simulation for flow and heat transfer to Carreau fluid with magnetic field effect: Dual nature study", Journal of Magnetism and Magnetic Materials, 2017

4

< 1% match (publications)

Hashim, Masood Khan. "Critical values in flow patterns of Magneto-Carreau fluid over a circular cylinder with diffusion species: Multiple solutions", Journal of the Taiwan Institute of Chemical Engineers, 2017

5

< 1% match (publications)

Prabhakar Besthapu, Rizwan UI Haq, Shankar Bandari, Qasem M. Al-Mdallal. "Mixed convection flow of thermally stratified MHD nanofluid over an exponentially stretching surface with viscous dissipation effect", Journal of the Taiwan Institute of Chemical Engineers, 2017

6


03/12/19
PROFESSOR
Department of Mathematics
Quaid-i-Azam University
Islamabad